LONDON CENTRE FOR NANOTECHNOLOGY

UNIVERSITY COLLEGE LONDON

MOLECULAR MODELLING AND MATERIALS SCIENCE

PHYSICS AND ASTRONOMY

FROM THE MECHANICAL PROPERTIES OF SINGLE CELLS TO THOSE OF SIMPLE TISSUES

Engineering Doctorate Thesis

Andrew R. Harris

4/4/2013

DECLARATION OF WORK

I, Andrew R Harris confirm that the work presented in this thesis is my own. Where information has been derived from other sources, I confirm that this has been indicated in the thesis.

ACKNOWLEDGEMENTS

CONTENTS

LIST OF FIGURES

1. ABSTRACT

As interest in biophysics and biophysical modelling has grown in the cell and developmental biology communities, a variety of techniques have been developed to measure the mechanical properties of single cells. Atomic Force Microscopy (AFM) has become one of the preferred methods for these measurements primarily due to its ease of operation and commercial availability. However, measurements on soft cells with a variable surface topography require an additional level of care so that the predicted contact area with the cell surface is accurately estimated. Using combined AFM and confocal microscopy I have shown that with pyramidal tipped cantilevers the cell body can easily deform to the shape of the tip but can also touch the underside of the AFM cantilever beam causing an overestimation of elasticity. Such artefactual increases in contact area could be avoided by using spherical tipped cantilevers or tips with a high aspect ratio. I examined the role of the cytoskeleton and cell contractility in setting single cell stiffness with AFM.

With techniques such as AFM, the rheology of single cells is becoming increasingly well characterised. The next logical step in furthering our understanding of organ and embryo mechanics is to scale up investigations to simple tissues such as on cell thick monolayers. I have developed methods to measure the mechanical properties of MDCK epithelial cell monolayers under AFM indentation or planar extension.

Using deep indentation of monolayers cultured on soft gels I have measured the evolution of mechanical properties upon the establishment of cell-cell junctions. The relative mechanical stiffnesses of monolayer-gel composites evolve as cell contacts are established and required the formation of mature contractile adherens junctions.

To measure the planar mechanical properties of cell monolayers I designed a system to create monolayers freely suspended from their susbstrate between two test rods. Cell monolayers have a higher stiffness than their cellular constituents due to the organisation of the cell cytoskeleton upon the formation of matured intercellular junctions.

2. INTRODUCTION

i.   THE ROLE OF CELL MECHANICS IN PHYSIOLOGY

Human diseases are conditions or states that not only impair bodily functions but threaten general health and well-being. Current research has been largely focussed on the molecular, microbiological, and immunological basis for pathologies. However, the mechanical properties of cells and tissues can also become altered in disease, which is often apparent in the presented symptoms. Understanding how cells and tissues are able to sustain external mechanical stresses is crucial in developing treatments and determining the origin of such pathologies.

One typical example of single cells that require specific mechanical properties for their function is the red blood cell. Sickle cell anaemia is a genetic disease where haemoglobin is not correctly produced in red blood cells. Cells with the mutant haemoglobin have an altered shape that is sickle like rather than bi-concave and have a higher viscosity and stiffness (1). These alterations reduce the ability of cells to pass through small blood vessels and deliver oxygen to tissues. Sustaining external stress is a normal part of physiology for tissues and organs. Alveoli in the lung withstand large deformations during breathing, endothelial cells are exposed to fluid shear during blood flow and epithelia sustain peristaltic movements in the gut (2, 3).

Cells can also sense the mechanical properties of their environment and the forces that are generated within them. Cells detect external forces through proteins that interface the extra cellular matrix to the cell membrane and the cytoskeleton (4-8). The mechanical properties of the environment can therefore determine cell fate. One classical example of this behaviour is that the stiffness of the substrate stem cells are cultured on to directs their differentiation (5). In cancer, a rigid mass surrounded by soft tissue is a characteristic of tumour development and often diagnosed through palpation or elastography. Changes to the mechanical properties of the extra cellular matrix drive cellular contractions, a malignant phenotype, and the progression of cancer (9, 10). Furthermore, transformed cells expressing certain oncogenes have increased elasticities, a characteristic that is detected by the surrounding cells which respond by collectively extruding the oncogenic cell from the tissue (11, 12).

Thus biomechanics research has entered an exciting era of investigation; where the mechanical properties of cells and tissues can be both a direct consequence, and a regulating factor of biological function and architecture.

ii. HIERARCHY IN CELL AND TISSUE MECHANICS

Cells are small soft objects that are highly dynamic, yet they are able to interface together to create large, strong and stable structures at the tissue and organ level. The interior of a single cell is a fluid, crowded with organelles, macromolecules, and structures that fulfil a variety of functions (13). Networks of subcellular filaments called the cytoskeleton form higher order meshes and bundles that endow individual cells with their elastic and rheological properties. However, these filaments are also dynamic and can be rapidly re-organised by the cell in response to chemical cues, enabling cells to migrate and change shape (14, 15).

Since single cells are soft (having a Young's modulus on the order of hundreds of Pascals) they implement additional strategies to sustain the large physiological mechanical stresses encountered at the tissue and organ level. Firstly, they can interface to the Extra Cellular Matrix (ECM). The ECM is a complex network of proteins and polysaccharides secreted by cells which forms into a porous, fibrous network allowing the diffusion of external biochemical cues (7, 13). This provides a strong scaffold for the cells to attach to (with individual collagen fibrils having a Young's modulus on the order of MPa, and kPa for collagen gels). In bone and connective tissue where the ECM is abundant, it primarily bears external stresses (3). Cells are able to remodel and organise the ECM in response to a wound and maintain its mechanical integrity (16, 17). In developing embryos where there is little ECM or where tissues need to form an impermeable fluid barrier between compartments, a second strategy is adopted. Cells can interface together through specialised adhesion structures that tie the cytoskeletons of neighbouring cells into a mechanical syncytium. Many of the cavities and free surfaces of the human body are lined by a "one cell thick" layer of cells called epithelia that employ this strategy. Development offers perhaps the most vivid illustration of epithelia withstanding and exerting mechanical stresses through intercellular junctions. Embryonic epithelial tissues are under a constant tension generated by spatially restricted cellular contractions that coordinate tissue level deformations (18). When intercellular-junctions are disrupted,

embryos fail to properly develop, displaying a disaggregated ectoderm consistent with mechanical failure (19). Early in vertebrate development, the absence of an extracellular matrix (ECM) in the blastopore (20) together with the lack of effect of inhibition of ECM synthesis on blastopore initiation, suggest that the mechanics of monolayers and force generation within monolayers govern blastopore formation (21, 22).

The mechanical properties of the ECM have been well characterised (3), but comparatively few measurements of monolayer mechanical properties exist. In this thesis, I sought to characterise the supracellular mechanical properties of tissue monolayers, and how these arise with the formation of intercellular junctions.

iii. CYTOSKELETAL FILAMENTS

The cytoskeleton is a cohesive meshwork of filaments that extends throughout the cell fulfilling a variety of functions; from motility (23) to shape change (24), cargo transport (25) and cell division (26). There are three main families of cytoskeletal filaments that are suggested to be important in setting the mechanical properties of cells; microfilaments (actin), microtubules (tubulin) and intermediate filaments (specifically the keratin subgroup). Physically, the different families of cytoskeletal filaments have distinct mechanical properties in terms of persistence length and Young's modulus. Biochemically, cytoskeletal filaments have different binding and unbinding rates of their subunits, meaning that they are dynamically distinct. They are regulated by a myriad of ancillary proteins which allow them to form higher order structures, interact with other filament populations, with organelles, and the cell membrane. I describe the three major types of cytoskeletal filaments in further details in terms of their characteristics and functions and the current opinion on how they contribute to cellular mechanical properties.

MICROFILAMENTS - ACTIN

The three isoforms of actin (α, β, γ) form the most abundant protein in eukaryotic cells. Polymerisation of the globular monomeric form (G-actin) into filaments (F-actin) and coalescence of filaments into networks is the main molecular mechanism underlying cellular morphogenesis. Actin plays a crucial role in cellular processes such as cytokinesis (26) and sarcomeric contraction (27), but has also been

established as the most important component of the cytoskeleton in setting cellular elastic (28) and rheological properties (29). Filaments are composed of a two stranded double helix with a width of 5-9nm and a repeat length of 36nm. The helix is coiled at a rotation angle of 167 degrees and has polarity, pointed and barbed ends (*Figure 1* A)(13).

Polymerisation of actin filaments can be subdivided into three different steps. The first step which limits the rate of polymerisation is the formation of a small actin nucleus from three individual monomers. This step is thermodynamically unstable. After a stable nucleus has formed the addition of subunits in the elongation phase is comparatively quicker. Actin monomers exist in two hydrolysed states; ATP bound and ADP bound. At the pointed end of the filament the association rate for each monomer hydrolysis state is equal. At the barbed end of the filament there is a greater affinity for ATP bound monomers, with the rate for ADP bound monomers similar to that at the pointed end. There is therefore net polymerisation of actin monomers at the barbed end and generally net depolymerisation at the pointed end of filaments. Once ATP bound monomers have bound to the filament, the ATP becomes irreversibly hydrolysed to ADP. When the monomer concentration available is just above the critical polymerisation concentration for the barbed end, and just below the critical concentration for the pointed end, the filament enters a steady treadmilling state. The rates of polymerisation at the barbed end and depolymerisation at the pointed end are balanced, in the steady state, and the filament remains at a constant length. In order for the cell to maintain a dynamic actin cytoskeleton it is necessary for there to be a large pool of monomers available for polymerisation and a fast treadmilling rate (13).

The balance between polymerisation/filamentous and depolymerisation/monomeric actin is controlled through many regulatory proteins. To induce cell shape requires rapid remodelling of actin filaments. This can be accomplished through de novo nucleation of actin filaments and cells have evolved specialised proteins to accelerate filament nucleation. Actin nucleators take various forms but all reduce the rate limiting step of forming a new actin nucleus. To maintain the pool of free monomers and remove actin structures that are not required the cell uses capping, monomer binding and filament severing proteins. Two of the main nucleators of actin are

Formins and the Actin Related Protein 2/3 complex (Arp2/3). Arp2/3 binds to the side of pre-existing mother filaments and nucleates daughter filaments that grow as branches from the mother filament. This type of nucleation tends to create branched networks of short actin filaments (*Figure 1* D). Formins bind to the barbed end of unbranched filaments. They promote polymerisation and elongate the filament facilitated by profilin. This type of actin nucleation leads to long bundles of filaments (*Figure 1* E).

Actin organisation in epithelia

In epithelial cells actin is largely localised to intercellular junctions where it serves to coordinate stresses between cells through adherens junctions (*Figure 1* B). At the apical membrane actin can also create small protrusions called microvilli to increase the apical membrane surface area (*Figure 1* C). This enhancement to surface area enables the cells to absorb and secrete more efficiently, such as in the brush border of the intestine. Below the apical membrane, actin is organised into a contractile band that is interfaced between cells by structures called adherens junctions. The interface of the actin network to adherens junctions, its assembly and regulation is of significant interest in the community as it is these characteristics that allow cells to interface together mechanically (*see chapter 2, section IV, Adherens Junctions*).

Actin and mechanics

The mechanical flexibility of polymers is usually defined in the physical sciences by the persistence length, which is the length at which the direction of the polymer chain becomes uncorrelated (30). Actin filaments have a persistence length of ~20μm which is of the order of the size of the cell. It is not therefore likely that the flexural rigidity of actin filaments defines the mechanical properties of cells. Rather, it is the assembly of filaments into crosslinked and entangled networks that govern cellular mechanical properties. Indeed the presence of a single species of crosslinking protein actin gels can go from fluid to solid elastic meshes simply by altering the ratio of crosslinker and filament length (31). The binding rate of crosslinkers thus sets the timescale and frequency response of actin networks to stress. Different types of actin crosslinkers and nucleators create different actin structures that fill a variety of functions and have different mechanical characteristics (*Figure 2*).
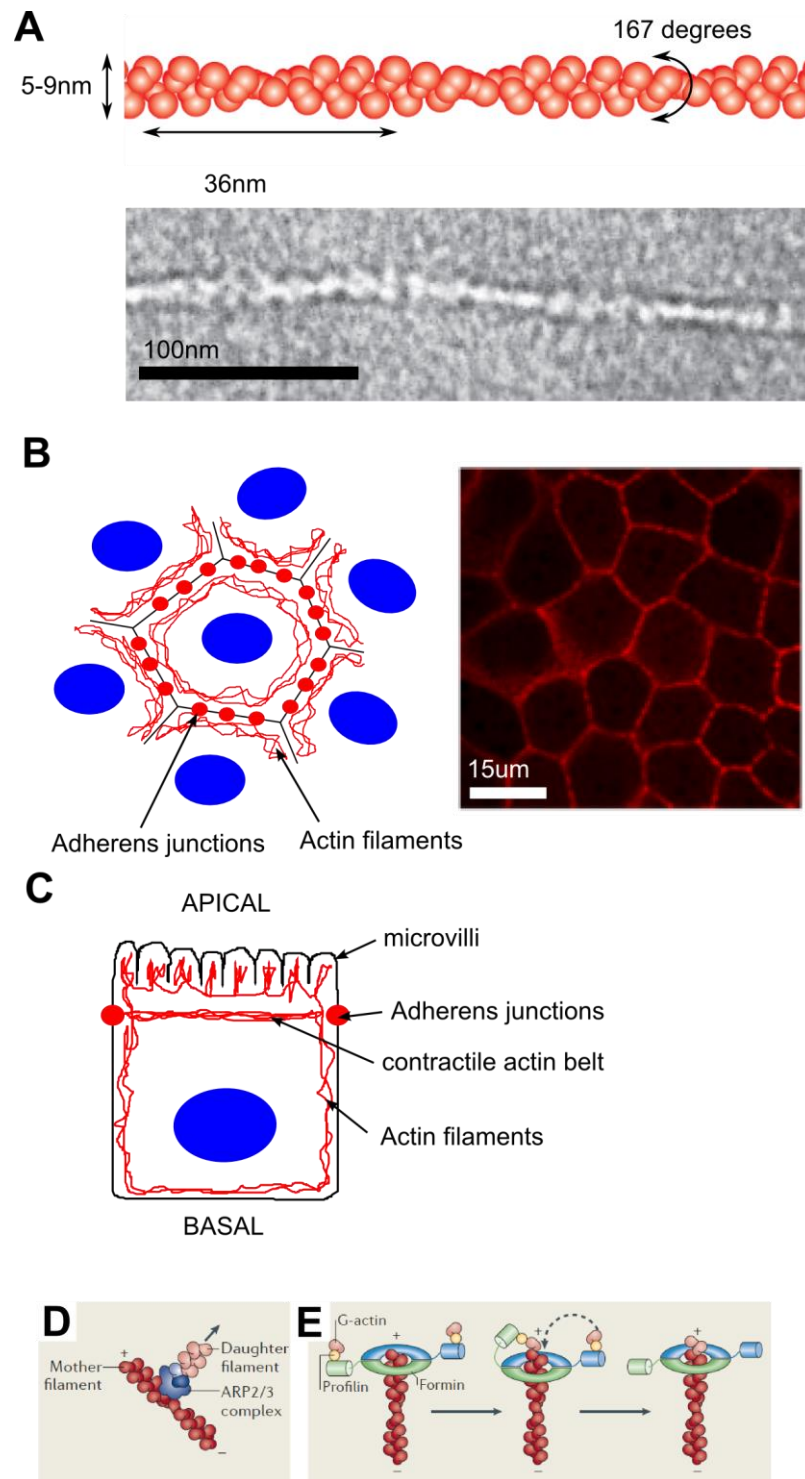
Figure 1 : The actin cytoskeleton

(A) Schematic of an actin filament and a Transmission Electron Microscope image (13). (B) Actin localisation in MDCK epithelial cells in a planar view. In epithelial cells actin localises to intercellular junctions. The actin cytoskeletons of neighbouring cells are interfaced to one another through adherens junctions. (C) Side view of an epithelial cell showing the actin cytoskeleton. Adherens junctions in typical epithelia localise towards the apical membrane. Microvilli are actin rich protrusions at the apical membrane that increase the cellular apical surface area. (D) Branching of actin filaments by the Arp2/3 complex. (E) Formin mediated elongation of actin filaments (32).
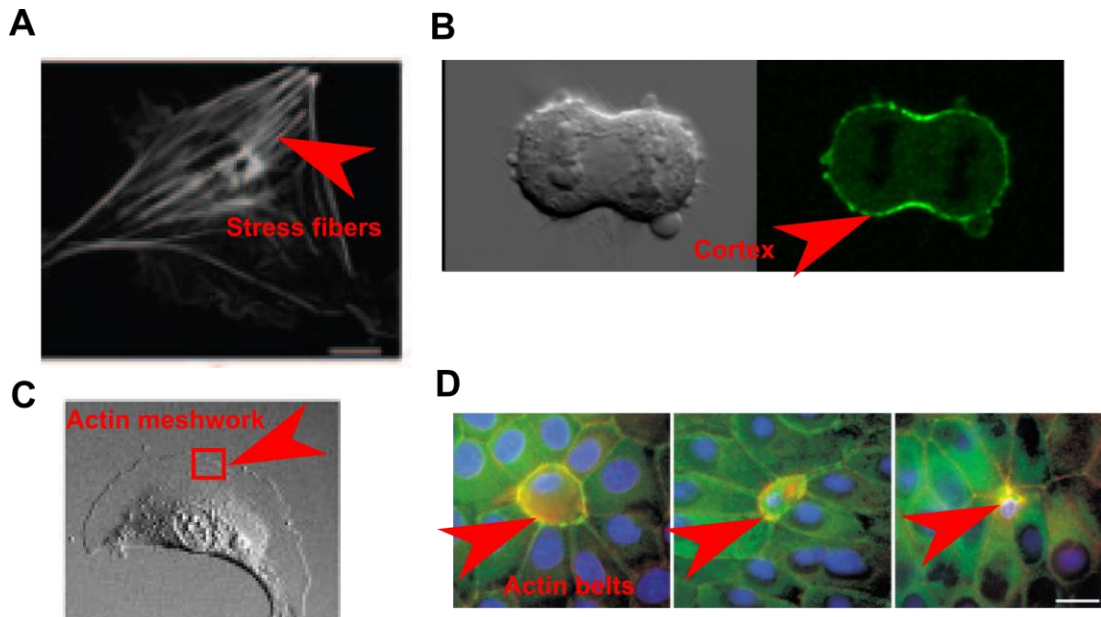
Figure 2 : The mechanical properties of actin networks

(A) Stress fibres within cells are located basally and are maintained under tension by myosin contractility (33). (B) The actin cortex in a dividing cell determines cell shape and mechanical properties (34). (C) In migrating cells, branched actin meshworks help it to polarise the direction of motility (13, 35). (D) Contractile actin belts within epithelia constrict the dying cell apical membrane to maintain barrier function during apoptosis(13).

Stress fibers are contractile actin bundles that form at the base of the cell. They consist of bundles of filaments of alternating polarity crosslinked by α-actinin and myosin motor proteins (*Figure 2* A). The actin cortex is a thin meshwork of crosslinked actin filaments below the plasma membrane and is maintained under tension by myosin activity. This structure controls cell shape, particularly during cell division (*Figure 2* B). In migrating cells, the actin network is often formed into a thin branched meshwork at the front of the cell called the lamellipodium (*Figure 2* C). In epithelia, cells often display a contractile belt of actin located close to the cell apical membrane. As cells undergo apoptosis, myosin is recruited to this actin belt causing the dying cell to contract and eventually be extruded. In this instance the contraction of the actin belt enables the epithelium to remain impermeable to fluids as the apoptotic cell is removed (13)(*Figure 2* D).

MICROTUBULES - TUBULIN

Microtubules are hollow tubes formed from α and β tubulin heterodimers. These heterodimers form longer protofilaments. The most common arrangement of a

microtubule is thirteen protofilaments bound together in a hollow cylinder, but a wide variety of structures exist within the cell (*Figure 3* A). Like actin, microtubules have structural polarity through the different nucleotide bound states, called the plus and minus ends (GTP and GDP bound). The main function of microtubules is in the separation of daughter cell chromatids during mitosis, though they also serve as a mechanism for intracellular delivery of cargo via dynein and kinesin motors.

Microtubule organisation in epithelia

One key characteristic of epithelial cells is their apico-basal polarisation. Apical and baso-lateral membranes have distinct protein compositions and are separated by tight junctions. This polarisation is further extended to the microtubule network that have their plus ends oriented towards the apical membrane and minus ends towards the basal membrane (*Figure 3* B-C). In contrast to other cell types such as fibroblasts, where the microtubules radiate out towards the cell cortex from the MTOC/centrosome, the microtubules in epithelial cells are non-centrosomal. The polarised network of microtubules in epithelial cells hence serves as an effective mechanism for the vectorial trafficking of cargo to the cell surfaces (36).

Microtubule mechanics

The tubular structure of microtubules gives them a high persistence length of ~5mm, which is the highest of the three cytoskeletal filament types. The high persistence length of microtubules would suggest that on the length scale of the cell, they act as load bearing structures. One theory, tensegrity, suggests that microtubules are mechanically significant in this respect (37, 38). This model describes the cytoskeleton as a combination of rigid scaffolds connected together by tensed ropes (a tensegrity structure such as a suspension bridge). The analogy with the cell is that microtubules act as the compressional elements and are interfaced to microfilaments that are under tension. Indeed, proteins interface the ends of microtubules to the actin cortex that aid in force generation in dividing cells (*Figure 4* A). Microtubules can also be observed to buckle on external loading (38). They are also shown to be important in determining cell length. In elongated cells microtubules are aligned with the cell long axis (39). Disruption of microtubules with Nocodazole or Colcemide causes a reduction in cell length (*Figure 4* B). This would indicate that the

microtubules that interface to the cell cytoskeleton bear mechanical loads (***Figure 4*** C). However the role of microtubules in cell mechanics remains unclear. Indeed, disruption of microtubules only causes small reductions in cellular elasticity as measured with AFM suggesting that their principal function is not in sustaining mechanical load (28).
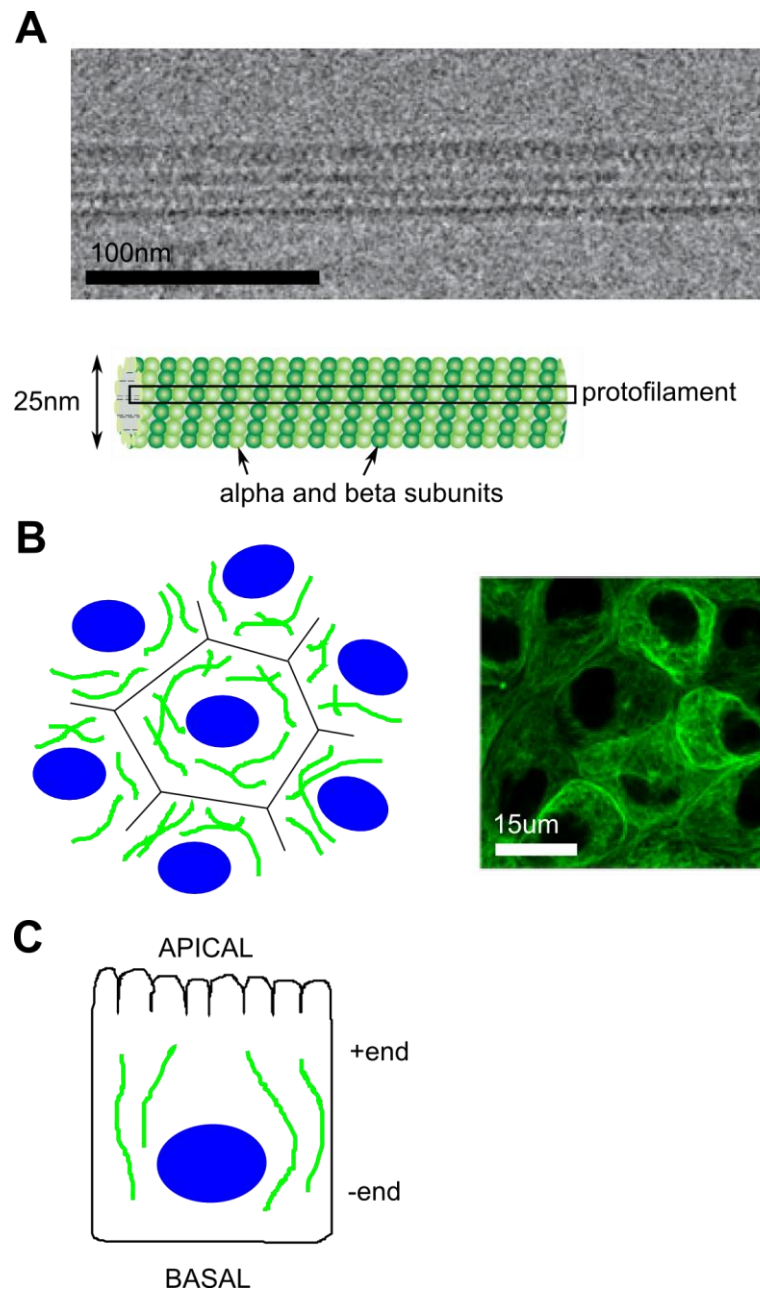
Figure 3 : Microtubules

(A) Microtubules are hollow cylindrical filaments of tubulin (13). (B) Planar view of microtubule organisation in epithelial cells. (C) Side view of microtubule organisation in epithelial cells.
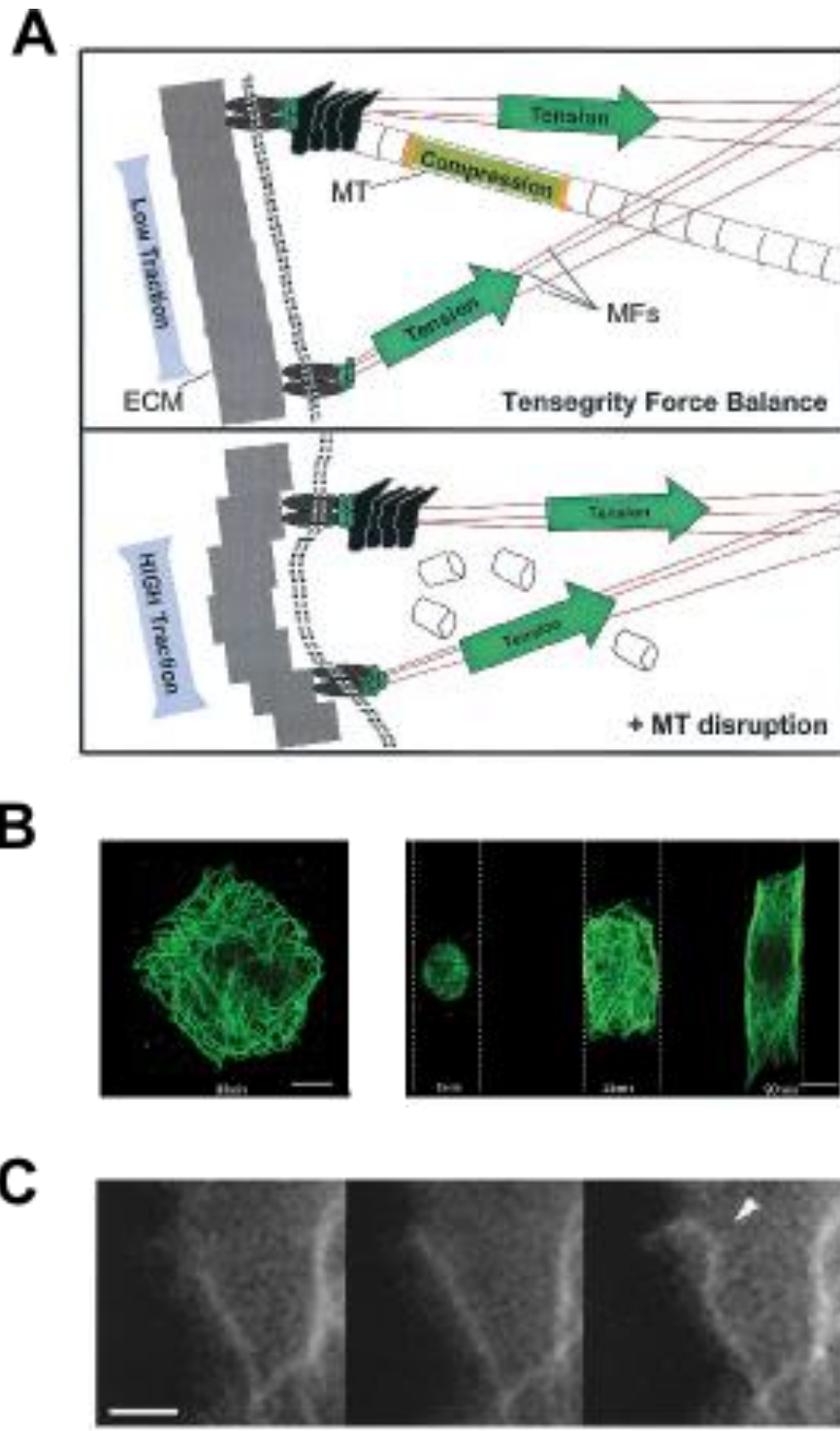
Figure 4 : The mechanical properties of microubules

(A) The tensegrity model for microtubules (38). In the tensegrity model of cells, microtubules are load bearing structures that are under compression, whereas actin microfilaments are under tension in the tensegrity structure. (B) Microtubules in a HeLa cell on micropatterned substrates (39). As cells spread along a line their microtubules align with the cell long axis suggesting that they can regulate the cell length. (C) Single microtubules in cells bend and buckle, suggesting a mechanical contribution to the cell morphology.

INTERMEDIATE FILAMENTS - KERATINS

The largest subgroup of intermediate filaments is called the Keratins. Each filament is made up from an equal mixture of type one (acidic) and type two (basic) Keratin proteins which form heterodimers. Two heterodimers join to make a tetramer filament subunit. Eight parallel proto-filaments made up of tetramers makes the filament. Unlike microfilaments and microtubules, intermediate filaments are non-polar (*Figure 5* A).
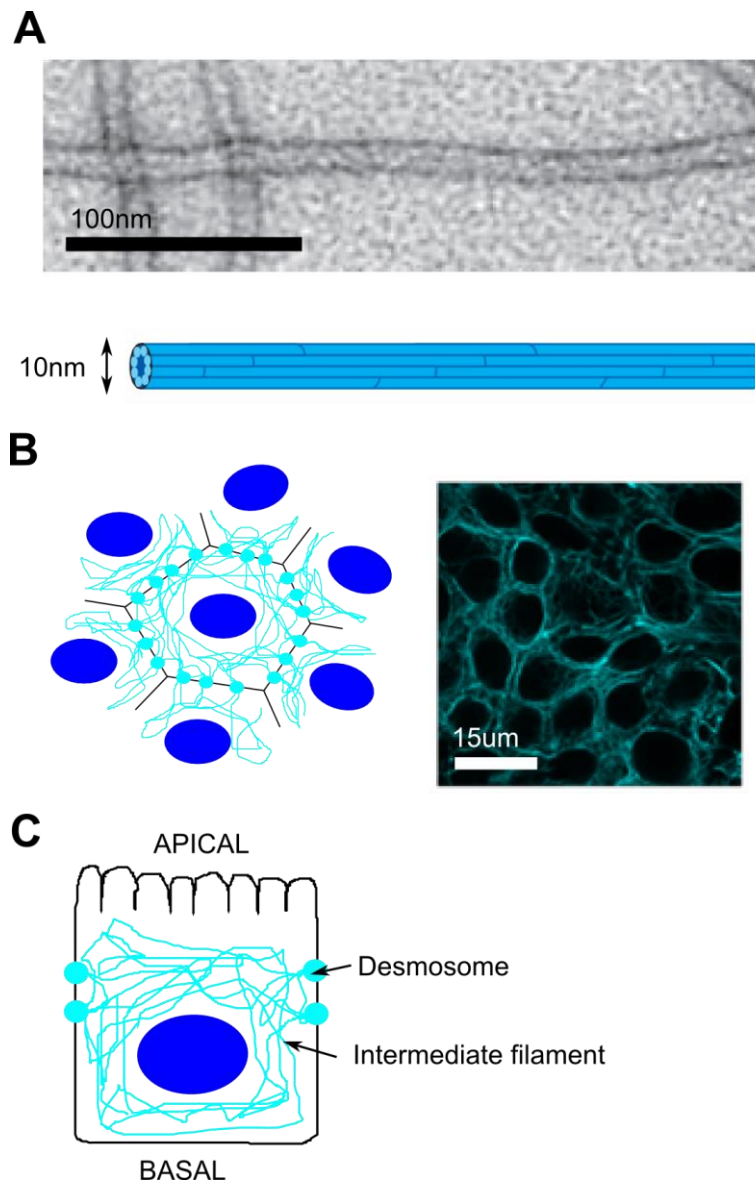
Figure 5 : Intermediate filaments

(A) Transmission electron microscope image and schematic view of intermediate filaments (13). (B) Planar view of the organisation of intermediate filaments within epithelial cells. Filaments span throughout the cell monolayer and are interfaced between cells through desmosomes. (C) Intermediate filaments do not have a specific apical or basal localisation.

Intermediate filaments organisation in epithelia

Intermediate filaments in epithelia are found spanning throughout the cytoplasm of constituent cells and are interfaced to one another by desmosomes (***Figure 5*** B, C). They are non-polar and hence do not have a specific orientation like that of microtubules and do not form specific mesh-works like microfilaments.

Intermediate filament mechanics

Intermediate filaments have a persistence length on the order of 1µm, much smaller than the typical cellular length scale. Indeed, intermediate filaments appear wavy within cells and do not display a high level of alignment or organisation. Due to their short persistence length and lack of higher order organisation the intermediate filament network would be unable to sustain compressive loading of cells. Therefore the role of intermediate filaments within cells is not well established though a number of hypotheses have been proposed. Speculation over their mechanical role comes from observations in some diseases with mutations in Keratin genes. Mutations in K5 or K14 filaments are associated with the disease Epidermolysis Bullosa, where increased expression of the mutant form of the protein results in shorter intermediate filaments. Patients with Epidermolysis Bullosa have increased skin fragility in the milder cases which results from blister formation and cytolysis, but in the more severe cases this can be fatal due to loss of tissue integrity (40). In Epidermolytic Hyperkeratosis, mutations in K10 result in increased tissue fragility, predominantly observed in the basal layers of the skin. When the Keratin 8 gene is ablated in mice embryonic stem cells, the embryo fails to develop past the formation of the liver, a stage where the mechanical stress in the embryo is increased (40). Moreover, the intermediate filament network is not found within the cells of animals such as Drosophila that have a protective exoskeleton, but is found in mammalian soft tissue (13).

Within the cell Intermediate filaments often coil into disorganised bundles where adjacent filaments are interfaced through non-covalent bonds. From a mechanical perspective this may suggest that intermediate filaments could contribute some plastic behaviour within cells and that they may exhibit a nonlinear mechanical response. When cells are subjected to high levels of strain, intermediate filaments appear taut between cell junctions suggesting that they are load bearing (41, 42). At

the single filament level AFM has been used to image single intermediate filament morphology under mechanical deformation (*Figure 6*) (43). Intermediate filaments are remarkably extensible, able to accommodate 250% extension at forces much larger than the maximum tensile force that microtubules or microfilaments can sustain (IF~1-2nN, MT~0.6nN) (44, 45). Thus all of the evidence suggests that intermediate filaments are crucial in preventing the lysis of single metazoan cells but also in interfacing cells into a mechanical continuum. Our lack of understanding of the precise mechanical role of intermediate filaments within cells is partly due to the diversity of filaments within this group and the lack of simple chemical treatments to disrupt the intermediate filament network. Indeed, Orthovanadate (46) and Okadaic acid (47) are largely non-specific and seem to only disrupt the intermediate filament network in a small percentage of cells. To further our understanding of their contribution to tissue mechanics, genetic manipulation of keratin in cells is required in combination with a mechanical testing approach.
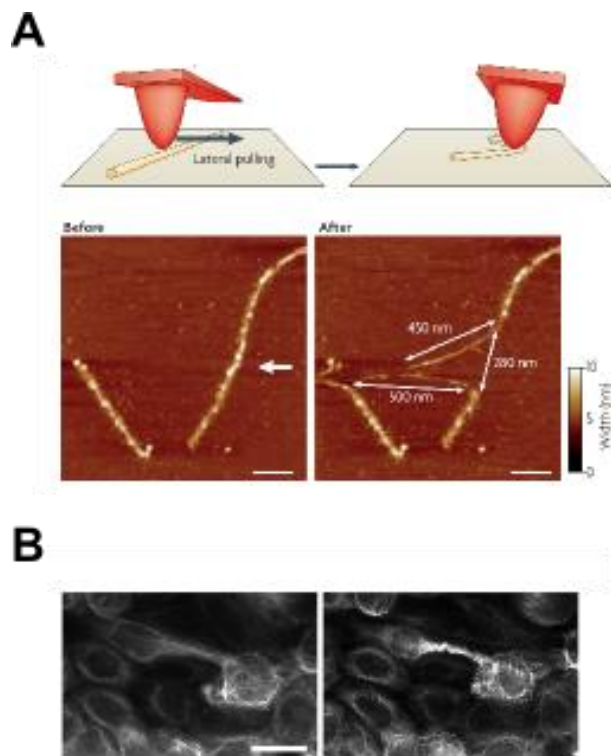
Figure 6 : The mechanical properties of Intermediate filaments

(A) Single intermediate filaments are flexible, as shown through atomic force microscopy shearing experiments (45). (B) In cells grown on elastic substrates, stretching the substrate stretches the cells and their intermediate filament networks. Upon release of the applied stretch the configuration of the intermediate filament network is altered suggesting a level of plasticity in response to extension (42).

iv. INTERCELLULAR JUNCTIONS

There are four key categories of intercellular junctions which fulfil a variety of functions. Occluding junctions seal cell contacts in polarized tissues creating a size selective diffusion barrier between the apical and basal membranes (48, 49). Gap junctions facilitate intercellular communication through the exchange of ions, second messengers and small metabolites between neighbouring cells (50). Adherens junctions and desmosomes interface the cytoskeletons of constituent cells into a mechanical syncytium and are discussed in more detail (51-53) (*Figure 7*).
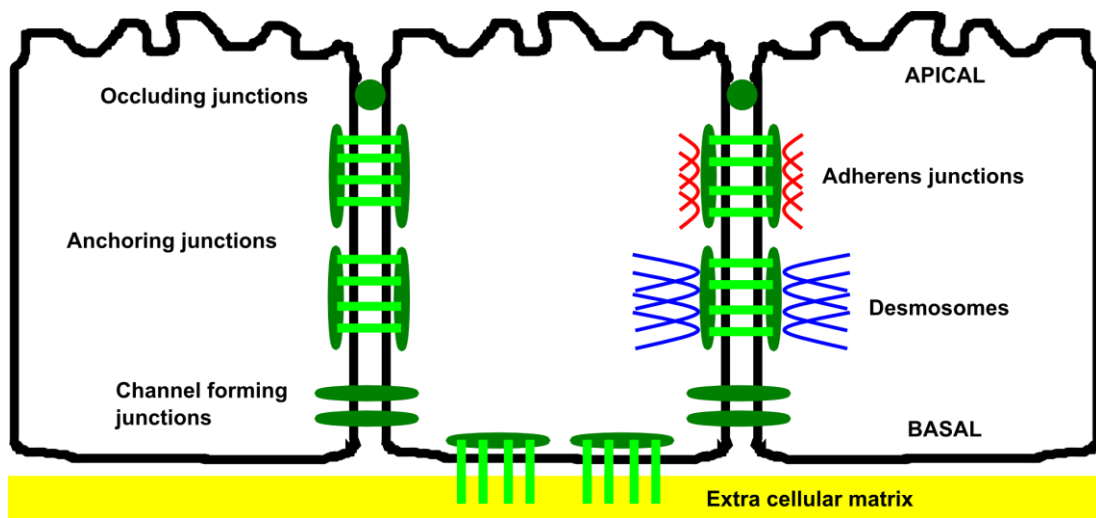
Figure 7 : Intercellular junctions

There are four main categories of intercellular junctions; Occluding junctions, Channel forming junctions, Adherens junctions and Desmosomes (13). Occluding junctions interface cells into a fluid impermeable barrier. Channel forming junctions enable passage of small molecules between adjacent cells. Anchoring junctions either mechanically interface the cytoskeletons of constituent cells together or link the cytoskeletons to the Extra Cellular Matrix (ECM). Adherens junctions interface the actin cytoskeletons of neighbouring cells whilst Desmosomes interface the intermediate filaments.

CALCIUM DEPENDENT ADHESION - CADHERIN

Connections to the ECM are mediated through the trans-membrane superfamily of proteins called Integrins. Connections between cells are mediated through the Cadherin superfamily. Cadherins are the main adhesion molecules that mechanically interface cells together. In developing embryos, treatment with an anti-cadherin blocking antibody results in disaggregation of the embryo (19, 54). In the later stages of embryonic development, the expression of epithelial-cadherin helps to give the embryo mechanical stability and cellular organisation.

The classical epithelial-cadherin consists of an intracellular, a trans-membrane and an extracellular domain. The intracellular domain is binds to the cytoskeleton allowing mechanical stress to be transmitted between cells through these adhesions. The extracellular domain consists of 5 copies of the cadherin domain motif. Extracellular domains of E-cadherin bind to counterparts on neighbouring cells through homophilic binding. Each motif in the domain acts as a flexible hinge that becomes rigid with the binding of Ca^{2+} (**Figure 8**). In the absence of extra-cellular calcium, the extra-cellular domains become floppy and are rapidly degraded by proteolytic enzymes. Upon the addition of extracellular calcium these form bonds with neighbouring cells that are relatively weak and are strengthened with clustering of the cadherin (54, 55). This type of adhesion means that junctions are strong but can be disassembled easily by the sequential breaking of individual bonds. Cadherin contacts occur in the two main types of intercellular junctions that sustain mechanical stresses: Adherens junctions and Desmosomes.
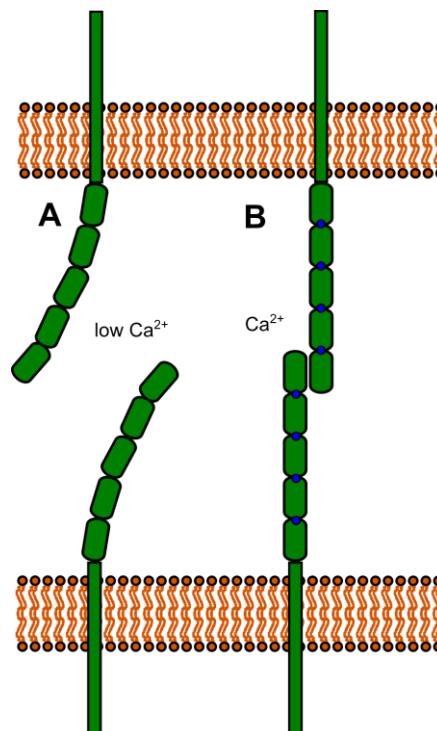
Figure 8 : Calcium dependent adhesion

(A) *In low calcium conditions the extracellular domains of cadherin are floppy and unaligned (13).*
(B) *Upon the addition of extra cellular calcium, or the formation of cell-cell contacts cadherins interface to one another through homophilic connections. Because of this single cadherin bonds are not mechanically strong, but allow the cell contacts to remain dynamic (32).*

ADHERENS JUNCTIONS

Adherens junctions serve to interface the actin cytoskeletons of neighbouring cells (*Figure 9* A). This is accomplished through the specific structure of cadherins and the proteins that bind the cadherin cytoplasmic tail and interface it to actin microfilaments. The extracellular domains of cadherin bind between neighbouring cells interfacing their membranes. The cytoplasmic tails of cadherin bind directly to a protein called B catenin. B catenin serves as a scaffold to interface alpha catenins that can bind to filamentous actin. p120 catenin can directly bind to the cytoplasmic tail of cadherin and regulates its stability at the plasma membrane (56).

However, the precise mechanism by which cadherins interface to the actin cytoskeleton is still being investigated. Proteins such as Eplin, Vinculin and Myosin are also suggested to bind cadherin to actin filaments (32). Furthermore, the cytoplasmic tail of cadherin can also bind other proteins and signalling molecules (*Figure 9* B).

The interfacing of cadherin to the actin cytoskeleton enables the propagation of cytoskeletal contractility from one cell to the next. At the tissue level forces can be coordinated into large deformations and shape changes, which are important in embryonic development (18, 57). Adherens junctions and the corresponding actin network are normally apically located in epithelial cells (*Figure 9* B). The actin network forms a contractile belt that runs parallel to the adherens junctions at the lateral cell membranes. This actin network is regulated by the formin Diaphonous 1 and the Actin Related Protein 2/3 complex that can nucleate actin filaments (13, 32).

A

B
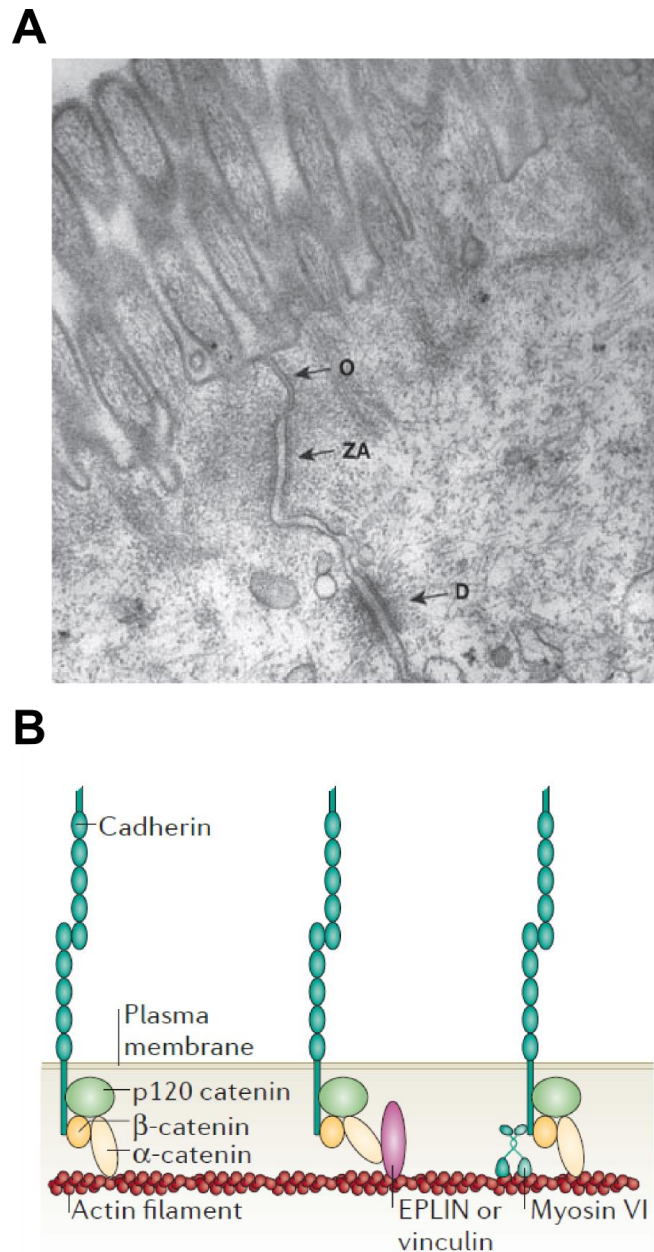
Figure 9 : The structure of adherens junctions

(A) Transmission electron microscope image of tight junctions (O), adherens junctions (ZA) and desmosomes (D) (13). (B) Diagram of the different ways that cadherins can interface to the actin cytoskeleton (32).

FORMATION OF ADHERENS JUNCTIONS

The biological sequence of events leading to the formation of mature intercellular junctions has been studied extensively and is progressively becoming better understood (***Figure 10***) (51-53, 58). Adherens junctions are assembled through the formation of cadherin-catenin clusters following contact between the lamellipodia of

two nearby cells. After initial contact, additional actin is recruited to these clusters and the junction expands through extended contact of the lamellipodia (56, 59). This polymerisation of actin is facilitated through the activation of the nucleating factor Arp2/3 by WAVE. Then, the dendritic lamellipodial actin network is remodelled into a peripheral actin belt through the combined action of de novo polymerisation by formins (60, 61) and network rearrangement by myosin contraction and α-catenin (53, 62). Later, the actin belt becomes increasingly contractile, a process regulated by the crosstalk between the small GTPases rac1 and rhoA (63, 64).
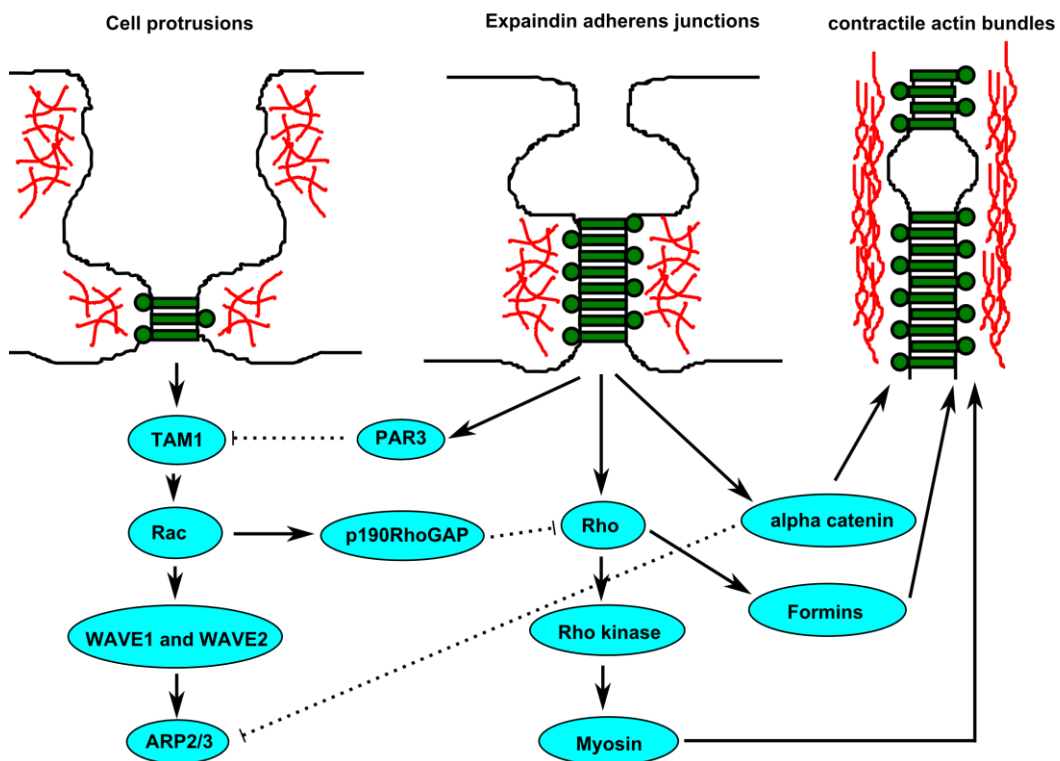
Figure 10 : Formation of adherens junctions

Initial contacts of lamellipodia between cells are stimulated by Arp2/3 mediated crawling of cells. The initial contact activates Rac, WAVE and then Arp2/3 mediated polymerisation of actin filaments at the junctions which drives expansion of the initial contact. Then junctional actin is remodelled by myosin II activity and formins. This de novo polymerisation and actin remodelling by myosin and alpha catenin creates a contractile actin belt that is interfaced to cadherin clusters (53).

DESMOSOMES

Desmosomes possess structural similarities with adherens junctions but are interfaced to the intermediate cytoskeleton rather than actin. Desmosomes form plaques that tightly interface cells together. In physiology, diseases such as

Pemphigus and *Epidermolysis Bullosa simplex* which have altered desmosome function or mutations to the intermediate filaments present with symptoms such as skin blistering and reduced tissue strength, suggesting that these structures have a mechanical role in tissues. In desmosomes the transmembrane members of the cadherin family Desmocollin and Desmoglein form the intercellular contacts (***Figure 11***). Their cytoplasmic domains interact with the proteins Plakophilin and Plakoglobin, which are linked to Desmoplakin that interfaces the whole complex to intermediate filaments (***Figure 11*** B). Lateral interaction of adjacent plaques increases the structural integrity of the desmosomes.
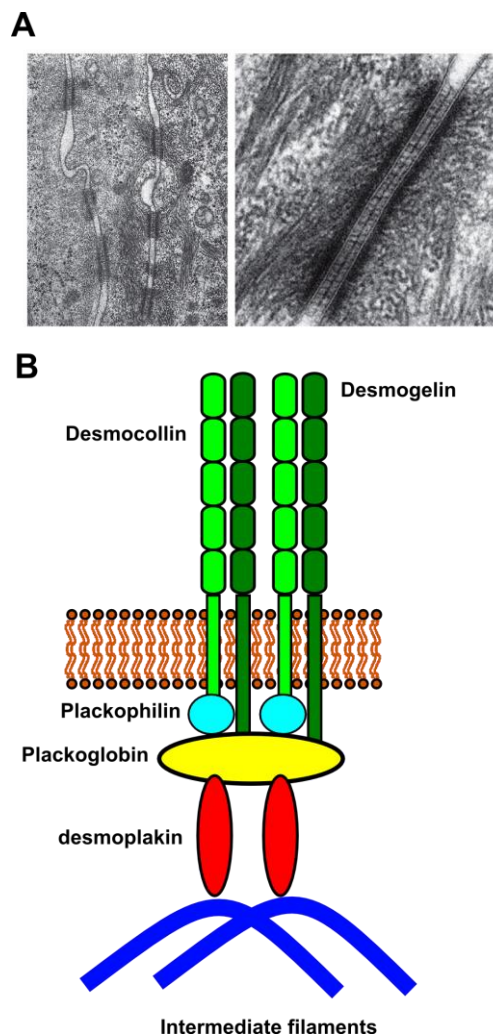
Figure 11 : The structure of desmosomes

(A) Transmission electron microscope images of desmosomal contacts between cells, and a zoomed in image of one desmosomal plaque (13). (B) Desmocolin and Desmogelin are members of the cadherin family of proteins that interface the membranes of adjacent cells. Their cytoplasmic tails bind to plackophilin and plackoglobin from the armadillo family. This complex is interfaced to the intermediate filament cytoskeleton through desmoplakin.

FORMATION OF DESMOSOMES

Desmosomes are formed in temporally distinct stages (***Figure 12***) (65). Desmocollin and Desmoglein are recruited to the cell membrane from the Golgi through vesicular transport along microtubules. Following the initial contact between cells, desmoplakin is recruited to the cell membrane, followed by a slow translocation of additional desmoplakin and plakophilin to the initial cluster sites that requires translocation along actin microfilaments (65). These adhesions then become stabilised at the plasma membrane upon interfacing to intermediate filaments (66, 67) and form mature desmosomes.
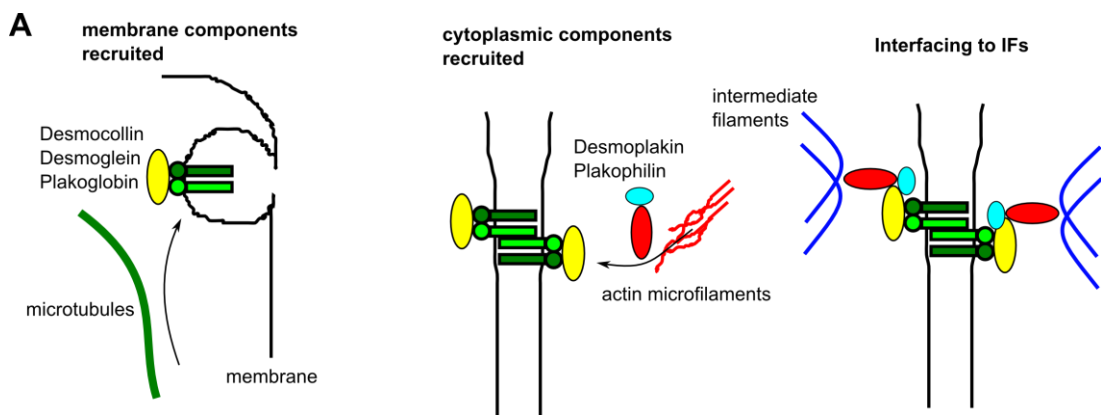
Figure 12 : The formation of Desmosomes

The initial recruitment of Desmocollin and Desmoglein to the cell membrane occurs through vesicular transport along microtubules. Then desmoplakin and plakophilin are recruited to the initial cluster sites in a process that requires actin microfilaments. These structures interface to intermediate filaments and form stable desmosomal junctions (65).

v. RHEOLOGICAL PROPERTIES OF BIOLOGICAL MATERIALS

LINEAR ELASTICITY

The mechanical properties of simple materials are characterised by the response of the material to an external load. The scaling of deformation with the applied load determines the linearity of this response. In simple crystals the stress (which is defined as the force per unit area loaded onto the material) scales linearly with the engineering strain (the change length of the material with reference to its original length), and is defined by a constant of proportionality the Young's modulus (68). In a crystal structure, the molecular determinant of this behaviour is the stretching of covalent bonds between atoms which are arranged into a regular lattice. After the

release of deformation the material returns to its original dimensions. Permanent deformation after an applied load is called a plastic deformation and is often observed at high levels of strain where the material begins to yield, whereas elastic responses are observed at low levels of strain. In general, a force acting on a given plane of a body is called a stress. In 3 dimensions, this is characterised by a second-order tensor. An analogous tensor characterises the relative deformation of the body called the strain tensor. In linear elasticity, these tensors are related by 21 elastic constants. However, assuming symmetry conditions and a perfectly isotropic material undergoing pure deformation in one direction is characterised by two scalars, the Young's modulus and the Poisson ratio. In the simplest case the Poisson ratio characterises the amount a material contracts in the transverse direction when being extended in the longitudinal direction.

$\sigma = \frac{F}{A}$ Stress is the force per unit area

$\varepsilon = \frac{L - L_0}{L_0}$ The engineering strain is the change in length relative to the original length

$E = \frac{\sigma}{\varepsilon}$ The Young's modulus is the stress divided by the strain

NON-LINEAR ELASTICITY

Nonlinear elasticity is where the Young's modulus does not scale affinely with the external stress or strain. This behaviour is often observed in materials at high levels of external stress or strain. Typical examples of non-linear behaviour are strain softening (a decreasing Young's modulus with strain) or strain stiffening (an increasing Young's modulus with strain). Non-linear elasticity can be characterised through the measurement of the differential elastic modulus. In these experiments, materials are loaded to an initial level of stress and their elastic modulus measured locally at this pre-stress (3, 31).

TIME DEPENDENT MECHANICAL PROPERTIES

In polymer melts and amorphous materials the response of the material to external load can also be time dependent arising from friction between molecules as they

flow past one another. Typical mechanical testing of the time dependent mechanical properties of materials incorporates measuring the temporal evolution of their strain under constant stress (creep) or the temporal evolution of their stress under constant strain (stress relaxation). Materials that display both elastic and time dependent characteristics are termed viscoelastic (69).

LINEAR MODELS OF RHEOLOGY

In homogeneous materials stress relaxation and creep measurements can be interpreted through simple continuum models. In the analysis of polymers, mechanical behaviour is often described by an empirical combination of linear springs and dashpots that can reproduce the observed mechanical behaviour. Simple models of this kind are the Maxwell model for viscous liquids and the Zener model for viscoelastic solids which take the following forms:

Maxwell model for viscoelastic liquids:

$$\sigma(t) = \sigma_0 \, e^{\left(\frac{-Et}{\eta}\right)}$$
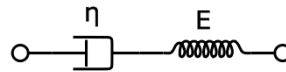
Zener model for viscoelastic solids:

$$\sigma(t) = \varepsilon E_1 + \varepsilon E_2 \, e^{\left(\frac{-E_2 t}{\eta}\right)}$$
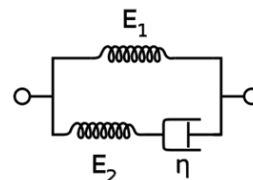
By introducing more components to the model, experimental data can be increasingly well fitted but the physical interpretation of models with many parameters start to lose their physical meaning.

CELLULAR RHEOLOGY

Simple continuum models can only adequately describe the rheological behaviour of cells in specific loading conditions over specific timescales. They fail to capture the universal rheological behaviour of cells that have become apparent with the development of new methods to probe cell mechanical properties. Instead of fitting

with many linear elements, experimental data can be fitted with a single decay exponent that spans a wide range of timescales (70). This equation is often celled a stretched exponential. Time is normalised in this equation to t_0 which can be set to 1sec for convenience as changing t_0 does not change the value of the power law exponent. This characteristic means that power law rheology is often referred to as being time-scale independent and takes the following form:

$$\sigma(t) = \left(\frac{t}{t_0}\right)^{-\beta}$$

Power law exponents in cells are often weak $\beta \sim 0.1$-0.5. These intermediate values that range between 0 and 1 signify that cell rheology incorporates both elastic and viscous elements, where $\beta=0$ is a solid material and $\beta=1$ is a fluid (70). The problem with power law rheology is that since it is a relaxation process with no dominant timescale it is difficult to make a connection with underlying molecular mechanisms. However, theories have been proposed to make these links such as soft glassy rheology.

Cells are complex heterogeneous media that exhibit complicated rheological properties (15, 29, 71-73). For example, cell elasticity and rheological behaviour is heavily dependent on the actin cytoskeleton. This is not solely an entangled network of polymers but also contains crosslinks, motor proteins actin as stress dipoles, and interfaces to other cytoskeletal networks as well as the cell membrane. Therefore the rheological properties of this network are highly dependent on the concentration of filaments and their relative crosslinking densities (74). Reconstituted actin meshworks can exhibit both stress softening at low filament density and stress stiffening at high filament density (75). Thus the mechanical properties of actin networks are non-linear at high strain. The added complication in interpreting the rheology of this network is that it is an active gel. Cells can do mechanical work through the hydrolysis of ATP. This can take the form of filament polymerisation or the movement of myosin motors along microfilaments (15). Indeed, the action of myosin exert high stresses on actin networks which further impacts their rheological behaviour. Thus the search for the appropriate mechanical model or a unifying theory for single cell rheology remains an active area of research.

vi. TISSUE MECHANICS

INTERCELLULAR ADHESION IN TISSUE MECHANICS

The cytoskeleton is the major determinant of single cell mechanical properties. It then stands to reason that to create strong and stable tissues cells need to interface their cytoskeletons into a mechanical syncytium. They accomplish this through cadherin mediated adhesion between cells and the formation of intercellular junctions as described in the previous chapter (*see chapter 2, section IV*). Thus forces that are generated at the cellular level can be coordinated into tissue level deformations. Cadherin cell contacts are under constitutive acto-myosin generated tension (76). This tension is increased with the application of an external load, and regulates the size of intercellular junctions (59). However, intercellular junctions are not just passive links between cells, but rather they are continuously remodelled in response to changes in signalling and changes in the mechanical environment.

In developing embryos differences in the level of intercellular adhesion is suggested to have a role in the spontaneous sorting of cells (differential adhesion hypothesis) (77). Differences in cell surface tensions drive the minimisation of the interfacial surface area between populations, much like the separation of immiscible liquids. The cellular surface tension was originally proposed to be set by the level of expression adhesion molecules, but recently the cortical tension in constituent cells has been suggested to be the driving force of this process (78).

TISSUE MECHANICS IN EMBRYONIC DEVELOPMENT

Embryonic morphogenesis requires the co-ordinated reshaping of tissues. Such large scale deformations are beyond what can be accommodated by cell shape change alone and requires the active re-arrangement of cells within tissues. This type of active re-arrangement endows tissues with fluid like or viscoelastic behaviour on long timescales (77, 79). There are three main mechanisms by which cells can re-organise within a tissue. Firstly, active neighbour exchange, called intercalation, is when two cells that are initially second neighbours come directly in contact through the exchange of junctions with their direct neighbours (80). Secondly, in cell death, cells that are not originally neighbours come in contact through the removal of a dying cell from the layer. Finally, a cell that divides into two new daughter cells adds

mass to the epithelium. Such processes are important in convergence extension of embryo anteroposterior axes where the cells within the embryo narrow along one direction and extend in the other. There are now sophisticated methods to determine the relative contributions of cell elongation to tissue morphogenesis during development (81).

In two dimensions, this type of mechanical behaviour can be simulated with models derived from the mechanics of soft matter such as foams. The network of cells within a tissue can we modelled with a vertex model. Here, cell vertices are modelled as a network of nodes joined together by elastic springs. Each cell has a specific target area which is modelled by an area elasticity, and a contractility. Intercellular junctions are also modelled as having an adhesion energy. These terms are incorporated into an energy function that describes the total energy of the network and can be minimised with either Monte Carlo or conjugant gradient approaches (80, 82). Increasing levels of complexity can be incorporated into the model by adding cell division and delamination. Vertex models have been used to investigate the delamination of cells at the midline of Drosophila embryos resulting from increased compression of cells (82). Vertex models are but one example of the types of computational models that can be used to simulate the mechanical behaviour of tissues. Potts models and 3D FEM models have also been employed to study convergence extension and invagination in embryos (83).

In developing embryos, there is a large amount of cell division and re-arrangements with the generation of organs and sub-compartments. Once tissues reach maturity they enter a homeostatic state where the number of cells within the tissue is tightly controlled. Loss of tissue homeostasis is a hallmark of disease and is often reflected in the mechanical properties of tissues.

FORCE HOMEOSTASIS IN TISSUES

It is well known that cells can adapt to the mechanical characteristics of their environment. They tune their mechanical properties to match that of their substrate (4, 5), migrate towards particular mechanical conditions, and sense the mechanical stiffness of the ECM through focal adhesions (6). The interaction of cells with their mechanical environment is particularly important in pathologies such as poly-cystic

kidney disease and cancer. If we take a purely mechanistic perspective, a growing tumour is confined by the surrounding tissue. As the tumour grows the mechanical pressure exerted by the surrounding tissue on the tumour increases. The amount of pressure is a direct result of the mechanical properties of the tissue and the degree of deformation. If the rate of cell death is mechanically sensitive, and increases with mechanical pressure, then a critical homeostatic size exists where the rate of cell division is balanced by the rate of apoptosis (84). This theory can explain why metastasis is a relatively inefficient process, as it is only successful when a cell invades into a tissue of comparable mechanical properties. This phenomenon is incorporated into a more general theory called "the soil and seed hypothesis" where specific environmental conditions are required for tumour growth (84).

There is some experimental evidence for the regulation of tissue growth by the mechanical properties of the environment. Cell spheroids that are exposed to increased osmotic pressure in their environment take longer to reach a specific size, and the equilibrium size is smaller with higher osmotic pressure (85). These results have also been confirmed in spheroids growing in gels of different mechanical characteristics, where increased stiffness of the surrounding matrix suppresses spheroid growth (86). When cells are cultured onto tensed elastic membranes, release of the membrane tension compresses the monolayer and increases the amount of live cell extrusion within the tissue as the cells try to restore a homeostatic density (87). This is a similar result to that observed in development where live cell delamination reduces tissue overcrowding in the midline of developing Drosophila embryos (82). To date, the majority of research has indicated that the level of either live cell extrusion or apoptosis within the tissue is mechanically controlled. However, it is also plausible that cells could divide in the direction of stress to transfer mass into that axis and dissipate the applied stress. This idea is particularly apparent in developing embryos of the fly where large numbers of dividing cells have a preferential orientation (88). Division and cell extrusion cause long timescale flow in tissues and determine their rheological properties (79).

COLLECTIVE MECHANICAL BEHAVIOUR OF CELLULAR AGGREGATES

Although rheological measurements of single cells are now widespread, and some of the mechanical behaviour of embryos can be represented through computational

models of development, there is a significant gap in our understanding of the mechanical behaviour of simple tissues. Many of the techniques that have been developed to study the mechanical properties of single cells cannot be easily applied to study the mechanical properties of cell layers. This is primarily due to the difficult preparation of the sample that is required. Simple tissues are often fragile and manually interfacing them to mechanical testing equipment with glue or adhesives can easily damage the sample (89, 90). Furthermore, even the simplest in vivo tissues often incorporate multiple layers of different mechanical properties, making the interpretation of mechanical testing data difficult. This leaves cultured tissues as the most suitable model for determining the mechanical behaviour of aggregates. Tissues of specific sizes and shapes can be easily prepared with micro-patterning and techniques from soft lithography (91-94). Much of our understanding of the behaviour of simple tissue mechanical properties has come from examining well defined patches of epithelia in vitro (91, 92), in vivo (95), or in response to typical wound healing assays (17, 96, 97), but purely mechanistic quantifications are lacking.

vii.   PHYSICAL TECHNIQUES IN THE LIFE SCIENCES

ORGAN MECHANICAL PROPERTIES

The mechanical properties of large tissue explants and organs have been the focus of bioengineering research for decades. A wide variety of samples from full organs (such as liver (98), lung (99), skin (100) and tendon (3)), to extra-cellular matrices (ECM, (101)) have been investigated through an array of mechanical testing techniques. Understanding organ and tissue mechanical properties is important in developing treatments for disease and for applications in regenerative medicine, such as prosthetic implants. One typical example is the relaxation of organ surfaces in response to a wound, which could be a surgical incision or resulting from an injury. The recoil of the tissue after incision gives an indication of the mechanical pre-stress within the material. The results obtained inform clinicians on the best way to orient an incision and to repair the wound (3).

Although examination of the mechanistic properties of organs has provided advances to medical practise, greater attention is now being focussed on understanding the

mechanical properties of single cells. Modern molecular biology can be used to selectively disrupt biochemical signalling and subcellular structures. When combined with mechanical testing, the contribution of a specific protein or organelle in setting a cells mechanical response can be measured. This approach can provide new perspectives on the origins of diseases that present with symptoms related to mechanical failure (such as increased skin fragility). Such advances are primarily due to availability of new experimental techniques that have been adapted from the physical sciences to measure the mechanical properties of single cells. Methods to characterise the mechanical properties and topography of surfaces have the resolution to probe the relevant length scales for single cells, spatially, tens of microns, and nano to pico newton levels of force.

Here, I review some of the techniques that can be used to measure the material properties of cells. Typically this type of mechanical testing incorporates applying a force to a material and monitoring the resulting deformation. However, it is important that cells are actively able to exert mechanical work, and generate forces through the hydrolysis of ATP. This phenomenon has been investigated by monitoring the extent to which cells are able to deform their surrounding environment. The most common of these methods is traction force microscopy which has been used to measure forces exerted by single cells (92, 102), cell doublets (59) and in monolayers (91, 96, 103, 104). However, these techniques do not enable measurements of classical material properties of cells such as the Young's modulus and ultimate strength of cells and tissues, and hence I do not review them in detail.

SINGLE CELL MECHANICAL TESTING

Techniques to measure the mechanical properties of single cells typically incorporate a small probe such as a bead or needle to induce deformations whilst simultaneously measuring the applied force.

Micropipette aspiration

Cells can be aspirated into a micropipette of known geometry with a controlled pressure. The internal diameter of the micropipette is smaller than the nominal diameter of the cell (*Figure 13 A*) and the internal pressure of the pipette can be

finely controlled from 0.1-1000Pa. The deformation of the cell as it enters the pipette is monitored with optical microscopy. Changes in cellular deformation with gradual step increases in pressure can be used to determine the cells rheological properties. Either the whole cell or just part of the cell can be aspirated into the pipette depending on the information required (**Figure 13 B**). Partial aspiration allows for measurement of the mechanical properties and tension of the cell actin cortex (34). For simple interpretation of the data, the Young Laplace equation for the internal pressure difference in spherical bodies can be applied (**Figure 13 A**). The precision and complexity of the interpretation of the data can be increased by using finite element models of the aspiration, for example by modelling the cell membrane and cortex as independent layers.

A   Cortex aspiration

$$T = \frac{P_e - P_i}{2\left(\dfrac{1}{R_p} - \dfrac{1}{R_c}\right)}$$

B   Whole cell aspiration

Neutrophil

Chondrocyte
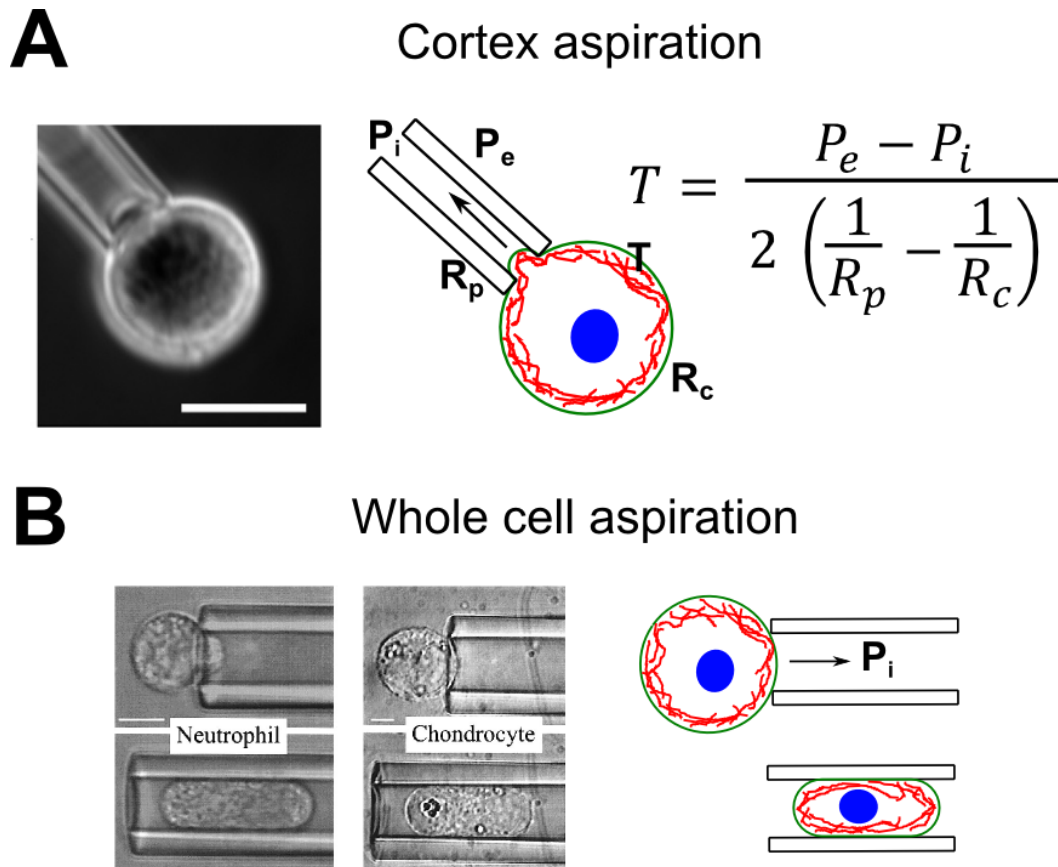
Figure 13 : Micropipette aspiration of cells

(A) Phase contrast image of a cell being aspirated into a micropipette. The difference between the inside pressure P_i and outside P_e pressure in the pipette can be related to the radius of curvature of the cell R_c and the hemispherical cap aspirated into the pipette R_p by the cortical tension T (34). (B) Micropipette aspiration experiments either aspirate the whole cell or only a hemispherical cap depending on the mechanical property of interest (105).

Magnetic bead twisting cytometry

In magnetic twisting cytometry, a magnetic field is used to apply a force to ferromagnetic particles, in this case specifically a torque (***Figure 14*** A). By functionalising the surface of the magnetic particles with ligands that bind to integrins on the cell membrane, deformations induced by rotation of the beads contain mechanical information about the underlying cell membrane and cytoskeleton (***Figure 14*** B-C). Typically 250nm-5µm beads are used and these are often partially phagocytosed by the cells. By applying an external magnetic field the remnant magnetic fields of the beads can be aligned in the external field direction. The remnant field can be measured with a magnometer and used to detect the deformation that is applied to the cells relative to the external field. Although this technique allows for the application of well-defined small forces, the interaction of the bead with the membrane is hard to quantify and characterise biochemically. Since magnetic twisting cytometry allows for acute deformation of the cell membrane it can be combined with other mechanical testing techniques such as deformable substrates (71).
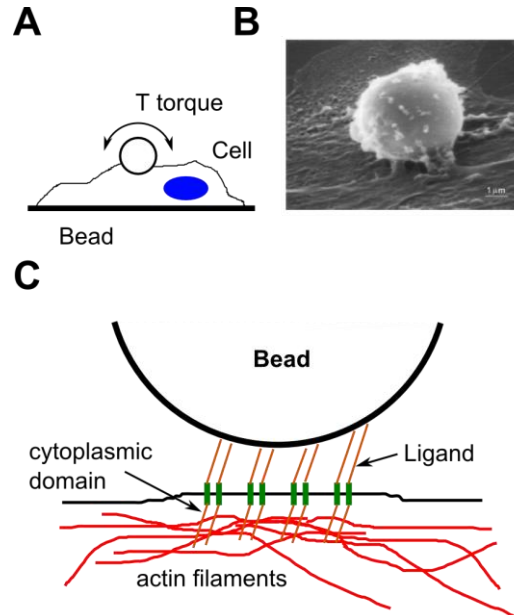
Figure 14 : Magnetic twisting cytometry

(A) Small magnetic beads are functionalised and attached to the cell membrane (71). By applying an external magnetic field a torque can be applied to the cell. (B) SEM image of a bead tethered to the cell membrane. (C) Typical molecules such as integrins bind to the bead and interface it to the actin cytoskeleton. This means that this experimental method can be used to probe cytoskeletal dynamics (1).

Optical methods: stretcher, tweezers and bead pulling

Optical methods in general rely on the conservation of photon momentum as a driving factor for the restoring force. As a focussed laser beam of photons enters a dielectric object of high refractive index, it becomes refracted upon entering and leaving the object. This causes a restoring force in the direction of the focal point of the laser beam. This system can be calibrated such that changes in the position of trapped objects relative to the focal point of the light can be translated into a force. Whole cells can be compressed with optical traps (*Figure 15* A), or cells stretched by moving beads that they are attached to with optical tweezers (*Figure 15* B). The main advantage of optical methods trap method is the high resolution of forces that they are able to measure. However, the maximum force that can be exerted onto the cells is limited by the trap stiffness (~100pN max) and whole cell methods are mainly useful for measuring the mechanical properties of non-adherent cell types.
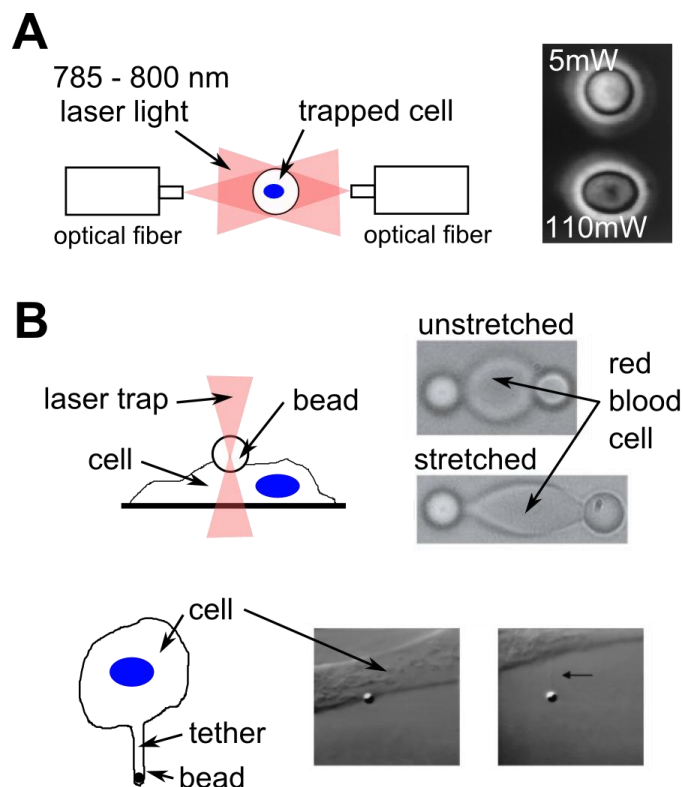
Figure 15 : Optical methods for measuring cell mechanical properties

(A) The optical trap method for deforming cells (106). High powered lasers can be focussed onto the cell and increasing laser power results in a larger cellular deformation (right). (B) The optical tweezers approach can be used to manipulate beads that are tethered to the cell membrane and can be used to stretch red blood cells (107) (right). In addition if the beads are completely engulfed by the cell then tethers of cell membrane can be pulled and used to measure membrane mechanical properties.

MULTICELLULAR AGGREGATE MECHANICAL TESTING

To better understand the contribution of cell-cell adhesion and cell interactions in multicellular mechanics, there have been several attempts to apply single cell mechanical measurements techniques to cell doublets and simple aggregates. This is a challenging task which requires a solution to several technical obstacles. For instance, aggregates of cells can be quite fragile and manipulating them prior to measurement is challenging.

Cell-cell interactions with two micropipettes

Dual micropipette assays have been used to measure intercellular adhesion. A cell is captured onto the end of each micropipette loaded onto a micromanipulator with suction. The cells are then brought together and allowed to establish adhesive structures on the order of minutes. The suction pressure in the pipettes required to separate the cells as they are pulled apart gives an indication of the magnitude of the adhesive force (***Figure 16*** A). This approach has been successfully employed to measure the adhesion between cells with mutant cadherin proteins (94) and also in cells from different tissues of a developing embryo (78). Although this technique can give indications of adhesion strength and surface tension it can only be applied to cells in suspension. In addition, only step increases in pressure can be tested rather than providing continuous measurements. Finally, since the cells are brought into contact for only a few minutes, fully mature intercellular junctions do not have time to form (78, 94). Even on timescales as long as 30mins full junction maturation cannot take place, whilst the main components of adherens junctions are formed, desmosomes and their interface to intermediate filament are not established (***Figure 16*** B). Therefore this technique is best suited for measuring the formation of junctions that only take a short time to establish such as cadherin junctions or non-specific adhesion, rather than desmosomes or fully matured contractile adherens junctions.
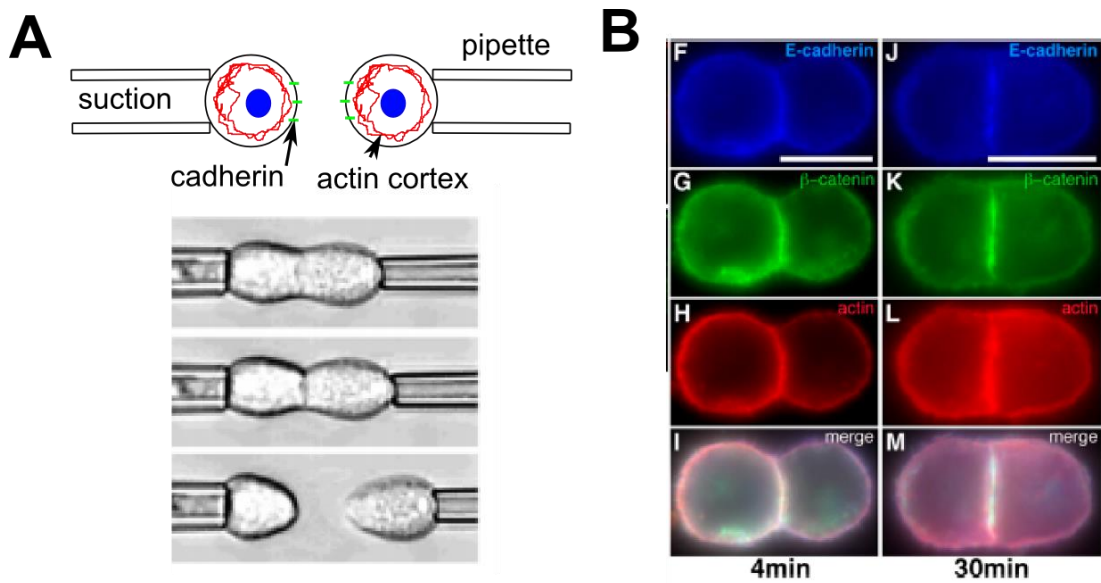
Figure 16 : Measuring adhesion between doublets

(A) Suction in the pipettes can be used to capture cells and touch them together so that they form adhesions. The separation pressure in the pipettes then indicates the force required to separate the doublet (94). (B) Doublets can be prepared on either short or longer timescales to establish the effect of junction maturation.

Micro tissue mechanical methods

There are a few microtissue mechanical testing methods that have been developed. A variation of traction force microscopy is to grow a tissue between two pillars (***Figure 17*** A) (108). Here, the forces exerted by contracting and beating cardiomyocyte tissues can be measured. Multi-cellular spheroids can be aspirated into pipettes in a similar way to single cell measurements to test their mechanical properties (***Figure 17 B***). Mechanical measurements are the most easy to interpret if a flat regular shaped material is extended in the plane. One tool to measure the mechanical properties of embryo explants allows for the measurement of elasticity and failure stress. In this approach embryo explants have to be glued to the mechanical testing system, where the fragile samples can be easily damaged (***Figure 17 C***) (89, 90). To date very few of these measurements have been made.
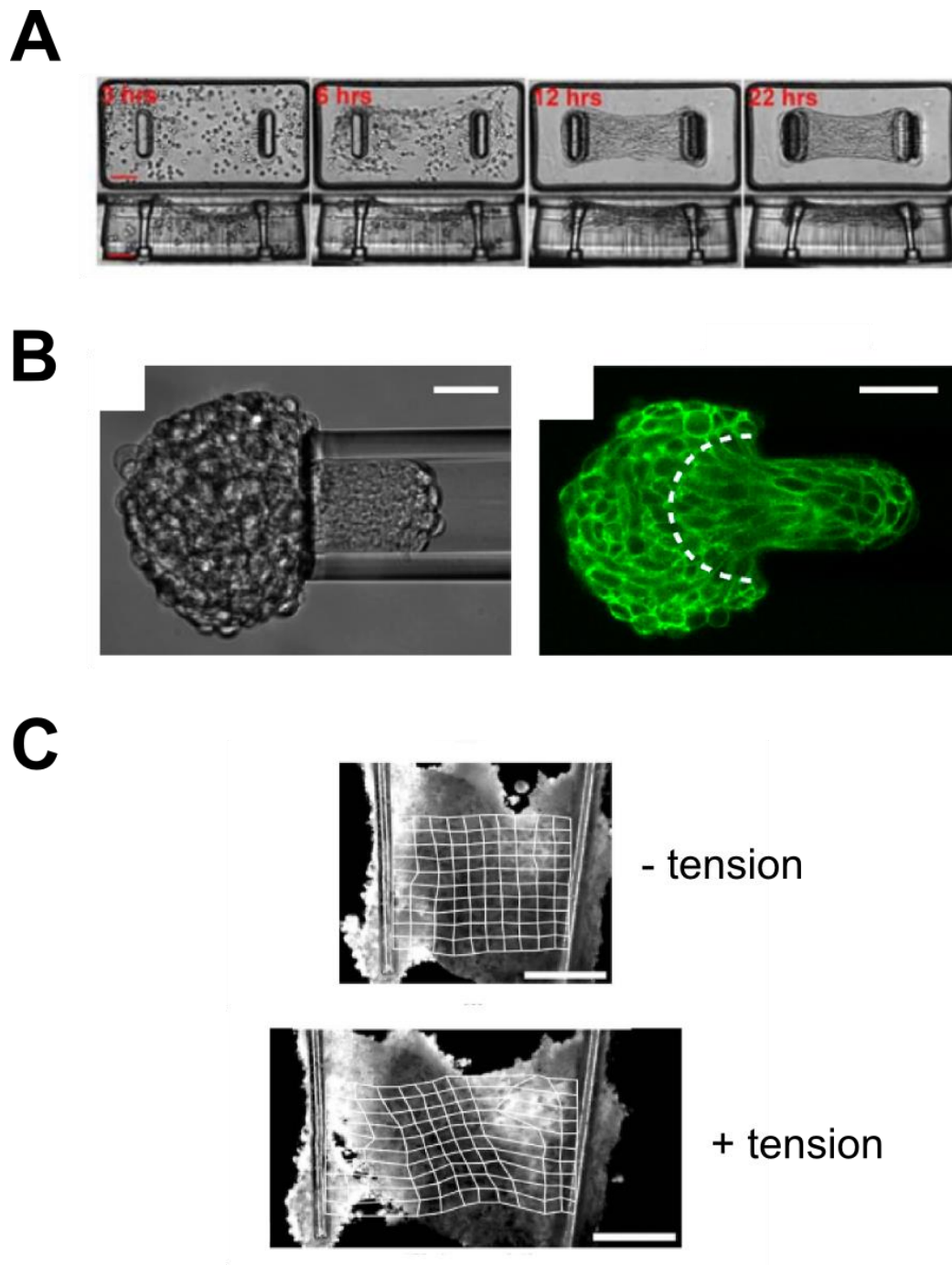
Figure 17 : Microtissue testing

(A) Micro muscle tissue grown between two PDMS pillars. As the cells grow they exert a contractile force on the gel which collapses onto the pillars (108). The beating force for cardiomyocytes can be measured with this approach. (B) Micropipette aspiration of a multicellular acinus (109). This can be used in a similar way to the cortical aspiration of single cells to infer mechanical properties. (C) Tensile testing of xenopus embryo explants (89).

Deformation of cells through elastic substrates

Adherent cell populations can be mechanically stimulated by the deformation of their substrate. PDMS elastomers offer a convenient way of making thin flexible substrates that are bio-compatible, can easily deform, and are elastic. Deformations can be either uniaxial or biaxial. One example of uniaxial extension of cells is the diaphragm inflation test, or cell drum (110, 111). Here, the membrane is inflated in order to stretch the cells by air pressure. The deformation of the membrane can be measured with a laser beam. However imaging the cells is difficult as the focal plane is not flat and changes during the experiment. Membranes can also be extended uniaxially, to stretch cells and observe the re-organisation of subcellular filaments (*Figure 18*) (42). This technique can also be combined with other methods to measure the change in the mechanical response of the cells under extension or compression (71). However, deriving quantitative mechanical data from these experiments is difficult as separating the mechanical properties of the cells from those of the substrate is non-trivial. Additionally, when subjected to large deformations cells can detach from the substrate.
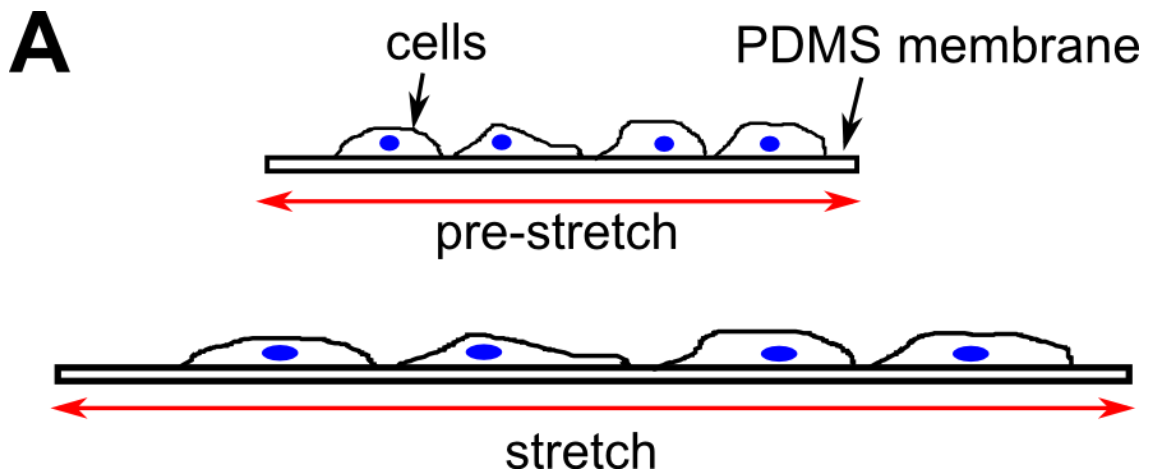
Figure 18 : Substrate deformation methods

(A) Cells can be stretched through extension of the elastomeric membrane substrates. However separating the mechanical response of the cells from that of the substrate is non-trivial.

viii.   ATOMIC FORCE MICROSCOPY

One technique that is becoming very common to measure cell mechanical properties is Atomic force microscopy (AFM). In AFM a small probe is scanned over a material's surface and used to measure properties (including topography, surface charge, and mechanics) that can be resolved at a spatial resolution on the order of the probe size. Atomic force microscopy (AFM) developed in 1986 by Binnig et al (112) has become a used due to its relative ease of operation and the production of commercially available probes with sizes as small as a 2-3 nm at the probe apex. This makes AFM a powerful method for imaging hard surface topography such as mica and graphite, or in imaging biomolecules attached to these surfaces (113, 114). In practise, AFM probes consist of a sharp tip usually pyramidal (~2-10μm tall), attached to a cantilevered beam (~200μm long, 50μm wide, and a few μm thick) which is an extension of a larger silicon chip (***Figure 19, bottom left***).
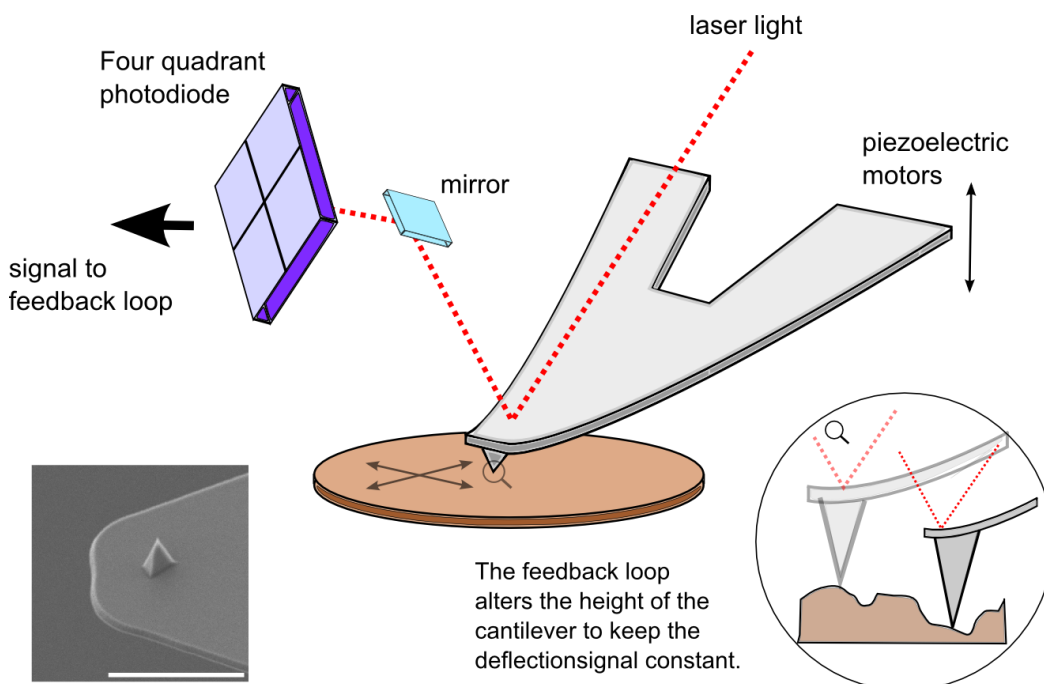
 Figure 19 : Atomic Force Microscopy

The AFM cantilever is scanned in a raster fashion over the surface. Laser light is deflected from the back of the cantilever at a different angle as the cantilever bends. This change is monitored with a four quadrant photodiode and used to measure the deflection and hence the resultant force on the cantilever. The zoomed region shows the feedback loop maintaining a constant force or cantilever deflection by changing the height of the piezo.The chip is mounted onto a piezoelectric support so that the height of the tip above the sample can be accurately controlled.

In addition, for coarse control, the piezo is often mounted onto a stepper motor setup. For basic imaging, the tip is brought into contact with the sample so that the cantilever bends, and is scanned over the surface in a raster fashion whilst maintaining constant piezo height (*Figure 19*). The relative deflection of the cantilever beam over the surface gives the sample topography (*Figure 19 bottom right*). The deflections of the cantilever are small (less than 1μm) relative to the cantilever length, and hence can be treated as linear, and are monitored optically. To do this a laser is reflected onto the back of the cantilever beam towards a four quadrant photodiode. As the cantilever bends the angle of reflection of the laser light changes and changes the signal in the diode.

Simply scanning the tip over the surface with the piezo at constant height can be problematic when the sample is soft. Indeed, excessive bending of the cantilever results in large applied forces and can damage the sample. Instead of using a constant piezo height, a feedback loop is used to maintain the deflection of the cantilever constant by changing the piezo height. In addition to feedback loops, other techniques for reduced sample interaction exist such as dynamically oscillating the cantilever for intermittent contact with the sample. Whilst for hard samples the indentation created by the AFM tip is small for soft samples even the smallest forces that can be applied by AFM cantilevers (typically a few hundred pN) create indentations that are much larger (hundreds of nm) than the apex tip geometry (a few nm) and hence the spatial resolution is decreased. In practice, images of soft biological materials such as cells often do not offer greater spatial resolution than that of optical microscopy.

FORCE MEASUREMENTS WITH AFM

Although imaging cells with AFM is not particularly advantageous, the use of AFM as a micromanipulator and for measuring mechanical properties of cells has become widespread. Instead of raster scanning the tip over the surface the deflection of the cantilever is monitored as a function of tip-sample separation as the tip is pressed into the sample. This approach is also known as a force-distance measurement (*Figure 20*). Initially the cantilever deflection stays constant until the tip reaches the sample (*Figure 20, grey line*). When the tip touches the sample the deflection begins to increase. The rate of deflection increase as a function of indentation depth can be

fitted with a contact mechanics model to extract information such as the sample elasticity. Several different analytical models exist, but the most commonly used is the Hertz model for the contact of two elastic spheres (115). In order to perform AFM measurements of elasticity correctly there are several guidelines that should be followed, which are discussed in more detail in *Chapter 5*.
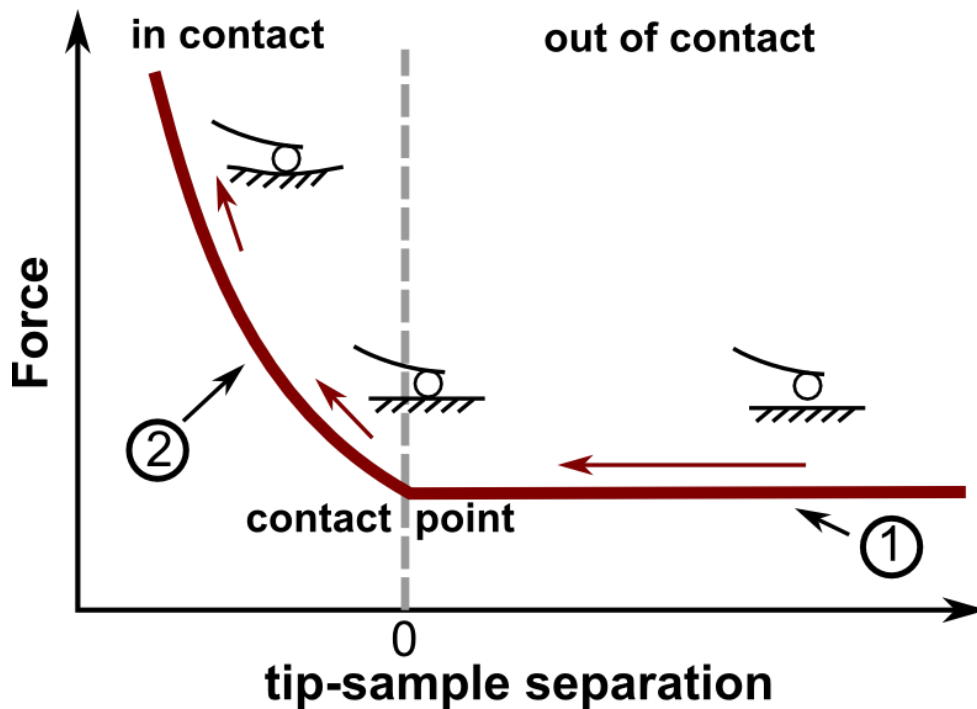
Figure 20 : force distance measurements

Initially the tip of the cantilever is out of contact with the sample. The deflection remains constant as the tip is gradually lowered towards the sample surface (portion 1 of the curve). As the cantilever tip touches the sample the deflection increases and the sample is indented (portion 2 of the curve). The second portion of the curve contains information about the stiffness of the cantilever (which is calibrated) and the sample mechanical properties. These can be extracted by fitting a two bodied contact mechanics model to the data.

HERTZIAN ELASTIC CONTACT MODELS

The Hertz theory of elastic contact is based upon three assumptions. In order to satisfy these conditions the contact of the two bodies must fulfil the following conditions (115, 116):

1. Continuous surfaces and small strains; the contact area is much less than the radius of curvature of the indenter.
2. Elastic half space; the contact area is much smaller than the depth of the indented body.

3. The surfaces are assumed to be frictionless; only a normal force is applied to the surface.

For a sample to be an infinite elastic half plane, the sample thickness must be large in comparison to the indentation depth. Contributions to the elasticity of the sample are therefore from the sample alone and not the surface that it is mounted upon. In measurements on cells this is of particular relevance. Cells are soft in comparison to common culture substrates such as glass and are often thin, such as in the lamellipodia. There have been some attempts to correct for the finite thickness of cells in indentation experiments (117), but in practise an appropriate force can be chosen by trial and error (checking the level of indentation at different forces) to satisfy *point 2*. At small levels of strain, rigid materials such as metals are in a linear elastic regime (68). For more compliant materials, such as rubber, very small strains can easily exceed the linear regime of elasticity. For cells, the depth of indentation needs to be small and accurately controlled to assume a linear elastic response. For this reason, opinions differ in the literature about the validity of the Hertz model for measuring cell elasticity. At large indentations cells exhibit non-linear behaviour which can be better fitted by a parallel recruitment of springs model or hyper elastic models (118-120). Measurement of cell elasticity at small indentation depths can be analysed with the hertz model and yields values that can be compared between treatments.

The Hertz theory of indentation can be modified to accommodate a range of different indenter geometries (116). The contact of the two bodies is assumed to be linearly elastic within the range of indentation and hence approximated by a simple Hookean relation. For the contact of a spherical tip indenting a flat sample, the radius of one sphere is chosen to be infinite, to represent a flat surface and the elastic modulus of the other chosen to be infinitely rigid to represent a rigid indenter. For a detailed description of the fitting procedure for AFM measurements and a critical discussion on the different approaches see *chapter 5* and articles by David C. Lin et al (121, 122).

HERTZIAN CONTACT EQUATIONS FOR DIFFERENT INDENTER GEOMETRIES

The general derivation for Hertzian contact between two elastic bodies is well established and described in a number of text books. For clarity I outline the key equations that are used in this thesis.

$\frac{1}{E^*} = \frac{(1-v^2)}{E} + \frac{(1-v'^2)}{E'}$ *Combined elastic modulus E* of the sphere E and specimen E' with poisson ratios of v and v' respectively. For a rigid indenter E' is infinite and the second term in this equation becomes zero. The combined elastic modulus is therefore a measurement of just the sample elastic modulus and poisson ratio.*

$\frac{1}{R} = \frac{1}{R'} + \frac{1}{R_s}$ *Relative curvature of the indenter R' to the specimen R_s. For a flat specimen R_s tends to infinity and the second term in this equation becomes zero. For MDCK cells, the curvature of the apical membrane R_s is roughly the same of that of the bead R', making the combined curvature R = R'/2.*

$\delta = \frac{a^2}{R}$ *Indentation depth δ for spherical indentation with contact radius a and indenter radius R as given by the hertz model for the elastic contact of two spheres.*

$a^3 = \frac{3}{4}\frac{FR}{E^*}$ *Radius of contact a between a rigid sphere of radius R and a flat surface with a combined modulus of E*.*

If we make the assumption that the spherical indenter is infinitely rigid and for the case of indenting a flat specimen we can derive a relationship between load and indentation depth. The load F needed to produce an indentation δ on the surface of a cell with elastic modulus E, radius of indenter R, and Poisson's ratio *v*.

$$F = \frac{4E\sqrt{R}}{3(1-v^2)}\delta^{\frac{3}{2}}$$

This solution can also be determined for indenters of different geometries. For the simplest case of a cylindrical punch, the contact area does not change with the indentation depth. Here "a" is the effective contact area.

$$F = \frac{2Ea}{(1 - \upsilon^2)} \delta$$

The general solution for a pyramidal shaped tip is given by the Bilodeau model. Here Φ is the opening angle of the pyramid.

$$F = \frac{1.4906\ E \tan(\Phi)}{2\ (1 - v^2)}\ \delta^2$$

For the case of AFM measurements our load is given by the spring constant of the cantilever and its deflection. Assuming a Hookean linear elastic behaviour with cantilever spring constant k and d the deflection we obtain the following for the indentation depth:

$$\delta = (\frac{3k(1 - v^2)d}{4E\sqrt{R}})^{\frac{2}{3}}$$

These equations are used in **chapters 5 and 6** to calculate the elasticity of biological samples using AFM based indentation experiments.

3. SCOPE

The mechanical properties of single cells are beginning to be better understood in relation to the biological structures that form their cytoskeleton and in the framework of physical models. At the organ scale, we have learnt much about biomechanics such as the relevant types of materials and Young's modulus to develop prosthetic implants. However, techniques to measure the mechanical properties of embryos and simple tissues are lacking. Simple tissues, such as cell monolayers, are a model system in which the tissue scale mechanical properties that arise upon formation of intercellular junctions can be investigated.

I sought to develop experimental techniques to measure the mechanical properties of cell monolayers. I first characterised the mechanical properties of single cells by AFM to provide a point of comparison for the mechanical properties of tissues. One of my initial observations was that values obtained for the mechanical properties of single cells were dependent on the measurement technique. In particular, AFM elasticity measurements appear dependent on tip geometry with pyramidal tips yielding elasticities 2-3 fold larger than spherical tips. In *chapter 5* I investigate the validity of AFM elasticity measurements and some of the assumptions that are made when interpreting force-distance curve data.

In the following chapters I describe two different experimental approaches that I have developed to measure the supracellular mechanical properties of cell monolayers. I investigated the emergence of monolayer supracellular mechanical properties which coincides with the establishment of intercellular junctions in *chapter 6.* I again used atomic force microscopy, but this time made large indentations into monolayer-gel composites. Although this technique allows for time dependent measurements of monolayer mechanical properties and is comparative between treatments, interpreting the results is a theoretical challenge. Hence I sought to develop another method to measure the planar mechanical properties of cell monolayers as discussed in *chapter 7*. I prepared freely suspended monolayers between two test rods and prised the test rods apart to measure their mechanical properties in the plane of the layer.

The general materials and methods for these experiments can be found in *chapter 4* but additional methods sections are incorporated to supplement each of the experimental chapters also. Final concluding remarks are discussed in *chapter 8* and future work for the project in *chapter 9*.

4. GENERAL MATERIALS AND METHODS

i. CELL CULTURE

Madin-Darby Canine Kidney II (MDCK-II) cells were cultured at 37°C in an atmosphere of 5% CO_2 in air in DMEM (Invitrogen, Paisley, UK) supplemented with 10% FCS (Invitrogen) and 1% Penicillin Streptomycin. Prior to experiment, the medium was replaced with Leibovitz L-15 without phenol red (Invitrogen) supplemented with 10% FCS. Cells were passaged every 3-4 days using standard cell culture protocols, and disposed of after 30 passages. When cells became confluent they were washed with phosphate-buffered saline (PBS) and incubated for 30 minutes with 1% Trypsin/EDTA (Invitrogen). Cells usually detach during this period but the remaining cells could be detached by gently tapping the culture flask. Trypsin activity was stopped by re-suspending the cells in 5ml of culture medium for a T25 culture flask (Falcon). Cells were resuspended to a new culture flask in a 1:10 ratio with fresh culture media.

ii. GENERATION OF CELL LINES

Stable cell lines were created to observe different cell structures with fluorescent microscopy. Cell lines were mainly created with viral infection and selection rather than using more traditional transfection protocols due to their low transfection ratio in MDCK cells. Stable cell lines were produced by Guillaume Charras.

To visualise the cell membrane, we created a stable cell line expressing the PH domain of Phospholipase Cδ tagged with GFP (PH-PLCδ-GFP), a phosphatidyl-inositol-4,5-bisphophate binding protein that localises to the cell membrane in epithelial cells. Briefly, PH-PLCδ-GFP (a kind gift from Dr Tamas Balla, NIH) was excised from EGFP-N1 (Takara-Clontech, CA, U.S.A), inserted into the retroviral vector pLNCX2 (Takara-Clontech), and transfected into 293-GPG cells for packaging (a kind gift from Prof Daniel Ory, Washington University (123)). Retroviral supernatants were then used to infect wild type MDCK cells. The cells were selected in the presence of 1 mg.ml^{-1} G418 (Merck Biosciences, Nottingham, UK) for 2 weeks and subcloned to obtain a monoclonal cell line with an epithelial phenotype.

For estimation of the cell volume, we created a cell line stably expressing cytoplasmic GFP. Briefly, wild-type MDCK were infected with retroviruses generated by transfecting packaging cells with pRetroQ-Ac-GFP-C1 (Clontech), selected with 500 ng.ml^{-1} puromycin (Merck Biosciences), and subcloned to obtain a monoclonal cell line with epithelial phenotype.

To visualise different components of intercellular junctions and the cytoskeleton, we generated cell lines stably expressing E - cadherin - GFP, keratin 18 - GFP, Life - act - GFP, cytoplasmic GFP, CAAX - Cherry, and MRLC - GFP. E - Cadherin was excised from E - Cadherin pBAT (a kind gift of Prof Yasuyuki Fujita, Hokkaido University, Japan), cloned into EGFP-N1 (Takara-Clontech, CA, U.S.A), and inserted into the retroviral vector pRetroQAcGFPN1 (Takara-Clontech). Keratin 18 - GFP pLNCX was a kind gift from Prof Rudolf Leube (University of Aachen, Germany). Life - act - GFP, a kind gift of Dr Roland Wedlich-Soldner (MPI, Martinsried, Germany) was inserted into the retroviral vector pLPCX (Clontech). The ras CAAX box, a kind gift from Prof John Carroll (University College London, UK), was inserted into pcDNA3 in frame with Cherry, and mCherry-CAAX was then inserted into the retroviral vector pLPCX. MRLC - GFP was inserted into pRetroQAcGFPC1. Retroviruses and clonal cell lines were then generated as described earlier. Retroviral supernatants were then used to infect wild type MDCK cells. The cells were selected in the presence of 1 mg ml^{-1} G418 (Merck Biosciences, Nottingham, UK) (for pLNCX plasmids) or 500 ng ml^{-1} puromycin (for pLPCX and pRetroQ plasmids) for 2 weeks and subcloned to obtain a monoclonal cell line with an epithelial phenotype.

For simultaneous visualisation of the keratin cytoskeleton and the cell membrane, cells stably expressing keratin 18-GFP were infected with CAAX-Cherry retrovirus before selection and subcloning.

iii. CRYO PRESERVATION OF CELL LINES

Cell lines that were created were stored under liquid nitrogen until use. To cryo-store cells, they were firstly grown to confluence in a large T75 (Falcon) flask, washed with PBS and detached with trypsinisation. The full cell suspension was then pelleted by centrifugation (Beckman-Coulter) in a 15ml falcon tube (Falcon) for 10

minutes at 1500 rpm. The pellet was then re-suspended in freezing medium (10% Dimethyl Sulfoxide (DMSO), 20% FBS, 70% culture medium), placed into a cryo-vial (Nalgene) which was then transferred to an isopropanol freezing chamber and placed at -80°C overnight. Cells were then stored in liquid nitrogen. When required, cells could be taken out of the liquid nitrogen to resume culture. The vial was gently warmed until the ice pellet could be poured into a 15ml flacon tube containing 10ml of fresh culture media. To remove the DMSO, the suspension was centrifuged for 10 minutes at 1500 rpm and the pellet re-suspended in 15ml of fresh culture media. The new suspension was transferred to a T75 flask and the cells given a week to recover before experiments.

iv. CHEMICAL TREATMENTS TARGETING THE CELL CYTOSKELETON

The controlled polymerisation and depolymerisation of cytoskeletal filaments is essential for basic eukaryotic survival and hence is the target for many natural plant toxins. Chemical inhibitors of cytoskeletal polymerisation and ancillary protein activity have become commercially available.
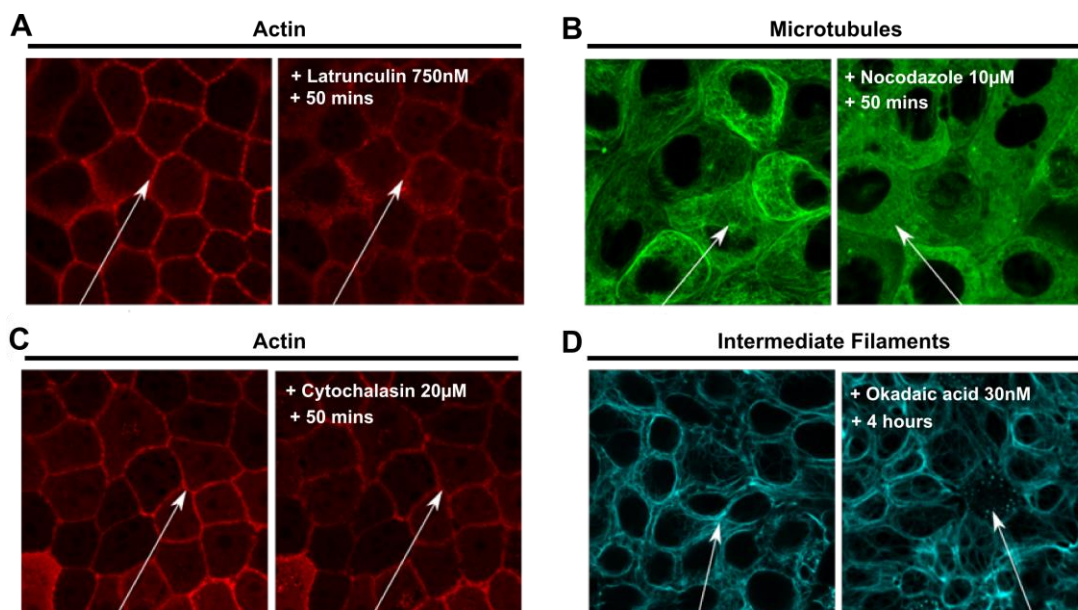
Figure 21 : Chemical perturbations of the cytoskeleton

Different chemicals and inhibitors can be used to perturb the cell cytoskeleton and were calibrated experimentally. Latrunculin and cytochalasin target the actin cytoskeleton through sequestering actin monomers and capping the barbed end of filaments respectively. Nocodazole depolymerises microtubules and intermediate filaments are disrupted by okadaic acid treatment, which is less specific. All drug treatments were incubated for 50-60mins with the exception of Okadaic acid which was incubated for 4hours. For measurements on freely suspended monolayers, drug treatments were implemented with the digestion phase, with the exception of EDTA treatment.

Many of these are permeable to the cell membrane making experiments easy to perform and informative when combined with confocal imaging. I calibrated the concentrations used in this thesis by imaging the targeted subcellular structures with fluorescent probes after drug treatment. A guideline for the concentrations used was the work by Rotsch et al (124).

Latrunculin B is extracted from the sea sponge Latrunculia magnifica (13). It sequesters actin monomers inhibiting them from binding to the barbed end of pre-existing filaments. This results in net depolymerisation of filaments as the pointed end (where depolymerisation is favourable) is unaffected. Treatment of MDCK cells with 750nM of Latrunculin B shows a reduction in the amount of highly localised fluorescent actin at the cell edge, due to the depolymerisation of filamentous structures (124) (*Figure 21* A) (*Table 1*).

Cytochalasin D is a metabolite secreted by a variety of moulds (13). Cytochalasin D is a capping protein which binds to the barbed and of filaments. This prevents the addition of actin monomers. Treatment of 20uM cytochalasin D has a similar effect to latrunculin treatment on the localisation of fluorescent actin in the cell (*Figure 21* C) (*Table 1*).

Nocodazole targets tubulin dimers in the same way as latrunculin does for actin monomers (13). By sequestering the free tubulin dimers it causes an increase in the number of microtubule catastrophes and at high concentrations causes depolymerisation of microtubules. Addition of 10uM nocodazole to MDCK cells shows depolymerisation of filamentous structures. The localisation of fluorescently labelled tubulin in filaments moves to being diffuse in the cytosol (*Figure 21* B) (*Table 1*).

Disrupting the keratin filament network is more difficult as there are no specific inhibitors of its polymerisation into filaments. A low concentration of Okadaic acid (0.2ug/ml) is non-specific but has been shown to disrupt intermediate filament structures (47). Localisation of the fluorescence from filamentous form to small globules can be observed but only in some cells (*Figure 21* D). In order to

completely disrupt the intermediate filament network a mutant strategies are required.

In mature monolayers, calcium-mediated adhesion through E-Cadherin was disrupted by chelation of calcium from the medium by addition of 5mM of EDTA (Sigma), a divalent cation chelator. To prevent the formation of E-Cadherin mediated adhesion in replating or low calcium experiments, cells were incubated with 10µg/ml of an anti-E-Cadherin blocking antibody that targets the extracellular domain of E-cadherin blocking intercellular adhesion (Uvomorulin, Monoclonal Anti-E-Cadherin antibody, Sigma). The actin filament network was disrupted by incubation with 750nM Latrunculin B (Sigma), a small molecule that sequesters actin monomers. To block actin filament nucleation through the arp2/3 complex and formin mediated nucleation, cells were incubated with 100µM CK666 (125) (Merck Biosciences) and 40µM SMIFH2 (126) (Merck Biosciences), respectively. To inhibit myosin activity, cells were treated with 50µM Y27632 (127) (Merck Biosciences) an inhibitor of rho kinase or 100µM Blebbistatin (128) (Merck Biosciences) which inhibits myosin II ATPase.

Cells were incubated in culture medium with the relevant drug concentration for 50 min prior to measurement. The medium was then replaced with imaging medium containing the same drug concentration such that the inhibitor was present at all times during measurements. Cells were treated with latrunculin B and cytochalasin D (to depolymerise F-actin), nocodazole (to depolymerise microtubules), Y-27632 (to inhibit Rho-kinase mediated contractility), and blebbistatin (to inhibit myosin II ATPase). All drugs were purchased from Merck-Biosciences UK (Nottingham, UK). To disrupt cadherin intercellular adhesion, monolayers were treated with EDTA (Sigma Aldrich) to chelate extracellular calcium.

| Inhibitor	Mode of action	Concentration	Effect
Latrunculin B	Sequesters actin monomers	750nM	Depolymerises actin filaments
Cytochalasin D	Caps the barbed end of actin filaments	20μM	Depolymerises actin filaments
Nocodazole	Sequesters tubulin dimers	10μM	Depolymerises microtubules
Y27632	Inhibits Rho kinase	10-50μM	Reduces myosin contractility
Blebbistatin	Myosin II	50-100μM	Reduces myosin contractility
EDTA	Divalent cation chelator	5mM	Reduces calcium mediated adhesion
CK666	Inhibits Arp2/3 nucleation of filaments	100μM	Reduces the extent of branched filaments
SMIFH2	Broad spectrum Formin inhibitor	40μM	Reduces actin polymerisation by formins

Table 1 Chemical perturbations to the cytokskeleton

Different chemical inhibitors used to perturb the cell cytoskeleton, their concentrations, target and mode of action.

v. STATISTICS

Data are reported as mean ± standard deviation except where otherwise noted. In box and whisker plots, boxes represent the 25th, 50th and 75th percentile and whiskers represent the maximum and minimum values in the data. Differences in values for the elastic modulus obtained using different tips and drug treatments were analysed by a two sample independent Student's t-test. Statistical significance was assumed at

p<0.05. The coefficient of determination r^2 was calculated as an estimation of the accuracy of model fit to experimental data

5. EXPERIMENTAL VALIDATION OF ATOMIC FORCE MICROSCOPY-BASED CELL ELASTICITY MEASUREMENTS

i. ACKNOWLEDGEMENTS

ii. INTRODUCTION

Atomic Force Microscopy (AFM) has been used to measure the elasticity of a wide variety of cell-types (129) (from fish keratocytes (130), to cancer cells (131), and stem cells (132)), at different stages of the cell-cycle (133, 134), and in different parts of a developing embryo (135), as well as to evaluate changes in response to genetic mutations (11) or drugs (124). Such widespread use is due primarily to AFM's relative-ease of operation, its high precision of force measurement, high-spatial accuracy, and the availability of mass-produced cantilevers.

Though AFM has very successfully been used for comparative measurements of cellular elasticity, the broad range of absolute elastic moduli reported for mammalian cells in the literature (100 Pa to 100 kPa) is intriguing (136). In contrast, other measurement methods such as bead tracking micro-rheology or micropipette aspiration give values of 100 Pa to 500 Pa for elasticity (137, 138). Such differences are usually ascribed to cell substructure heterogeneity and the far greater spatial accuracy of AFM measurements. The vast majority of AFM elasticity measurements utilise pyramidal-tipped cantilevers because of their wider availability. Surprisingly, measurements using spherical-tipped cantilevers are generally 2-3 times lower than measurements with pyramidal tips (139). This is often assumed to be the result of spatial averaging due to the larger contact area of spherical tips with the cell surface (140).

The organisation of cytoskeletal structures such as actin filaments and bundles can be examined with both optical and Scanning Electron Microscopy (SEM). By fixing and permeablising the cell membrane the sub-membranous actin cortex can be observed at high resolution with SEM. At the apical membrane of epithelia the actin cortex is arranged into a woven meshwork of thin filaments on the order of 7-10 nm in diameter (*Figure 22*). Since the cell membrane is soft and readily deforms upon contact with the AFM tip. The resulting contact area (hundreds of nm) is much larger than the tip apex (a few nm) or the mesh size of the actin network (<100nm). It is therefore unlikely that spatial heterogeneities in the actin network are responsible for variation in measured elasticity. I sought to understand the source of differences in elasticity between AFM and other measurement methods, as well as the dependence of AFM measurements on tip geometry.
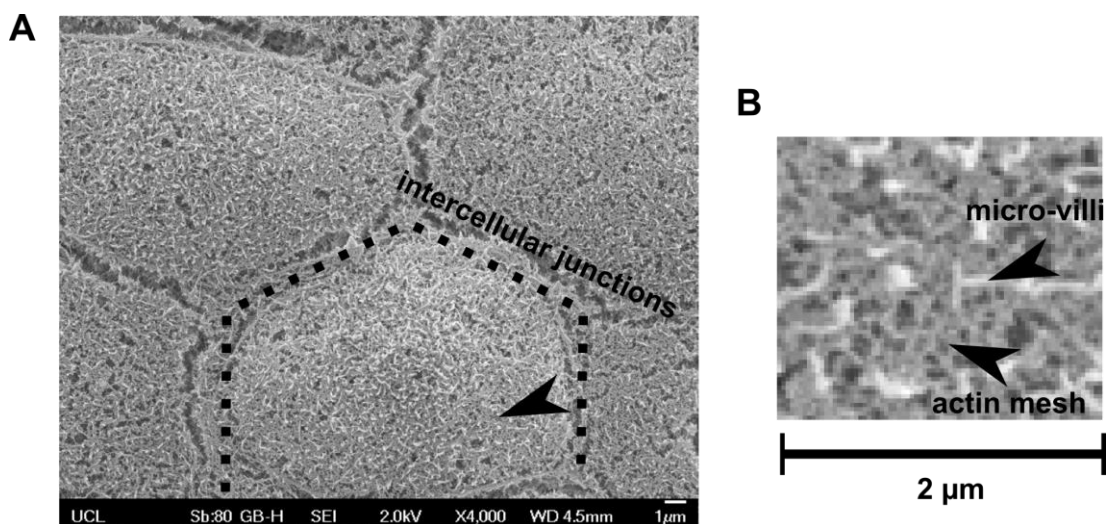
Figure 22 : SEM picture of the apical actin structures in MDCK cells.

(A) Actin filaments at the apex of MDCK cells form a tight network with a small mesh size. (B) As seen at high magnification. Even sharp pyramidal tips at low indentation depths have a large contact area with the soft cell surface. It is therefore, unlikely that spatial heterogeneity in the apical actin network can cause the broad range of elasticity values that are observed in the literature. These images were acquired with the assistance of G.Charras.

Several other potential sources of error exist that could affect elastic modulus measurements on living cells using AFM. First, errors may arise in processing of force-distance curves resulting from erroneous detection of the point of contact between the cell and the cantilever tip. Indeed, cantilever deflections at the point of contact are often of a similar magnitude to the measurement noise. Errors in

determining the point of contact inevitably affect the conversion of force-distance curves into force-indentation curves and therefore the estimated value of the elastic modulus. This point has been the focus of much attention and algorithms have recently been developed to better detect the contact point but their reliability has not been assessed experimentally on living cells (121). Second, during AFM measurements, the area of contact between the tip and the cell is not measured: it is estimated from the geometry of the tip, the indentation depth and contact mechanics models. To our knowledge, there exists no experimental verification of the shape of contact between cell and cantilever. Third, for estimation of elasticity from contact mechanics models, a measure of the cellular Poisson ratio is required. Because the cell is largely composed of fluid, it is often assumed to be incompressible with a Poisson ratio of 0.5, however few experimental measurements exist and these range between 0.3 and 0.5 (105, 141, 142).

In this study, I used an AFM-confocal microscope setup to systematically examine the presence and contribution of each potential source of error to elasticity measurements on living cells for both pyramidal and spherical-tipped cantilevers. For these experiments, I used epithelial cells that stably express a Green Fluorescent Protein (GFP)-tagged membrane marker and image AFM-induced cell deformation using a confocal microscope. I show experimentally that indentation depth is correctly estimated from force-distance curves but also reveal that large errors occur in the estimation of cell-cantilever contact area when using pyramidal-tipped cantilevers even at moderate forces (>0.4 nN). Using cells expressing cytoplasmic GFP, I estimated the cellular Poisson ratio from volume measurements before and during AFM indentation. Finally, I discuss the implications of our findings for AFM-based measurements of cellular elasticity and give guidelines to allow for error-free measurements.

iii. MATERIALS AND METHODS

GENERAL

AFM measurements and confocal measurements were performed using Leibovitz-L15 CO_2 independent medium supplemented with 10% FBS. All measurements in this chapter were conducted at room temperature.

AFM FORCE DISTANCE CURVE ACQUISITION

For AFM measurements, I utilised a JPK Nanowizard 1 (JPK, Berlin, Germany) interfaced with an inverted microscope (IX-81, Olympus, Berlin, Germany). For elasticity measurements, I used both standard pyramidal-tipped cantilevers (MSNL, nominal spring constant k=0.05 N/m, Veeco, Manheim, Germany) and the same cantilevers modified with a spherical tip. Cantilevers were calibrated by the thermal noise method before each experiment (143). Spherical tipped cantilevers were made by gluing (UV curing glue, Loctite, Hertfordshire, UK) a 15µm diameter fluorescent bead (Fluorospheres, Invitrogen) to the very end of the cantilever beam (***Figure 23***). During experiments, the cantilever tip was aligned over the centre of a cell and force-distance curves acquired with an approach speed of $3\mu m.s^{-1}$ and target forces ranging from 0.2-3.0 nN. This slow approach speed was chosen to minimize the contribution of time dependent properties of the cell to the apparent cellular elastic modulus (144). Forces were chosen to keep the indentation depth to less than 20% of the cell height such that errors resulting from the limited cell thickness were reduced (117, 145). Measurements were made above the cell nucleus. In epithelial cells, the nucleus is located close to the base of the cell and hence its contribution to the elastic modulus can be neglected. After the target force was reached the piezo-electric ceramic controlling the height of the cantilever was kept at a constant height for 10 seconds before retraction to allow for acquisition of a confocal image of the indented zone.

AFM ELASTICITY MEASUREMENTS

Cell elasticity was evaluated from the approach phase of the force-distance curves. The non-contact portion of the curve was fitted with a line and the contact portion with the Bilodeau model for pyramidal contact or the Hertz model for spherical contact (115). For a given force F the indentation depth δ depends on the Poisson ratio υ, the elastic modulus of the sample E, and terms that relate to the contact area derived from the tip geometry:

$$F_{\text{spherical}} = \frac{4 \, E \, R_r^{\frac{1}{2}}}{3 \, (1 - v^2)} \, \delta^{\frac{3}{2}}$$

$$\frac{1}{R_r} = \frac{1}{R_c} + \frac{1}{R_s}$$

$$F_{pyramidal} = \frac{1.4906\ E\ \tan(\Phi)}{2\ (1 - \nu^2)}\ \delta^2$$

with R_r the reduced indenter radius, (where R_c is the radius of curvature of the cell surface, and R_s is the radius of the spherical indenter) and Φ the opening angle of the pyramid. For accurate estimation of the point of contact I used a previously developed algorithm (146) and implemented it in MATLAB (MathWorks, Natick, MA, U.S.A). Briefly, each experimental data point in the curve is in turn taken as the point of contact and a least squares minimisation is used to fit the non-contact portion up to the current point of contact and the contact model thereafter. The summed error of the two fits is calculated for each point and the point in the curve which has the smallest corresponding summed fit error is taken to be the correct contact point. The value of the elastic modulus was then calculated by fitting the contact portion with a lone fitting parameter.

AFM MEASUREMENTS OF INDENTATION DEPTH

For comparison with confocal microscopy measurements, I computed the indentation depth for given forces from force-curves. Indentation depths δ were taken as the piezo displacement z from the contact point minus the cantilever deflection d.

$$\delta = z - d$$

The extracted indentation depth was corrected for any drift in piezo height using data extracted from the piezo strain gauge during the confocal measurement.

CONFOCAL MICROSCOPY

For combined AFM and confocal measurements, I used an FV1000 confocal head attached to our inverted microscope (Olympus). All imaging was carried out with a 60x oil immersion objective (UPLSapo, NA=1.35, Olympus). The underside of pyramidal cantilevers could be visualised by collecting reflected laser light (647nm laser) and in these images, the tip could be identified as a dark region on the

cantilever surface. For spherical tips, the beads could be imaged by exciting them with a 647nm laser and collecting light at 680nm. GFP in the cells was excited with a 488nm laser and light was collected at 525nm.

CONFOCAL MEASUREMENTS OF INDENTATION DEPTH

To confirm the correct detection of the point of contact from force-distance curves, I compared the indentation depth derived from AFM measurements with depths measured optically by confocal microscopy for a range of forces (0.2-3.0nN). An x-z confocal image of the cell was acquired with 0.1μm steps in z along a line parallel to the cantilever long axis passing through the centre of the tip to give a side view of the cell before indentation (***Figure 24***). The cantilever was approached towards the cell surface until it reached the target force and another x-z confocal image was acquired while the cantilever height was kept constant (***Figure 24***). The cell membrane profile was extracted at each x position by fitting the fluorescence intensity profile with a Gaussian function. The peak of the Gaussian was taken to be the membrane position at x. Cell profiles were extracted prior to and during indentation.

For spherical tips, the indentation depth was found by subtracting the cell profile during indentation from the cell profile prior to indentation. This height difference was fitted with a parabola and the peak of the parabola was taken to be the indentation depth. The x-z geometrical profile of the pyramidal tip was extracted from SEM images. The indentation depth was found by fitting the x-z tip geometry to the indented x-z membrane profile. To find the correct position in x of the tip apex, the fitting procedure was repeated for each point in the profile and the summed squared error was calculated. The position in x with the lowest fit error was taken to be the correct location of the apex of the pyramidal tip (***Figure 26***). The indentation depth was found by subtracting the height of the indented membrane profile from the height of a parabola fit of the pre-indented membrane profile, at the tip apex. The full analysis for indentation depth measurement was implemented in MATLAB.

QUALITATIVE CONTACT AREA ANALYSIS

For qualitative analysis of the area of contact, confocal stacks of cells expressing PH-PLCδ-GFP were acquired prior to and during AFM indentation. The cell surface was then rendered with iso-surfaces using Imaris (Bitplane AG, Zurich, Switzerland) and examined to find areas with geometries that matched the geometry of the cantilever tip. Membrane-cantilever contact area could also be visualised in colour combined x-z confocal slices (MetaMorph, Molecular Devices, CA, U.S.A) showing the cell profile before and during indentation.

COMPRESSIBILITY MEASUREMENTS

To measure cell compressibility, cells expressing cytoplasmic GFP were cultured in a 1:100 ratio with wild-type cells such that they retained their epithelial phenotype. Confocal image stacks of cells expressing a cytoplasmic GFP were acquired prior to and during AFM indentation. During the experiments, cantilevers with spherical tips were brought into contact with the cell surface reaching a target force of 10 nN, large enough to cause an indentation excluding ~10% of the cell volume. After the target force was reached the cantilever was maintained at a constant height for 300 seconds while a confocal image stack was acquired. The background noise of the image stacks was removed by plotting a histogram of the pixel intensities and fitting a Gaussian function to the low intensity pixels. The threshold intensity of the image was chosen to be the mean of the fit plus two standard deviations. The image stacks were then low pass filtered, thresholded, binarised, and subjected to a round of erosion-dilation to create a contiguous cell volume image devoid of isolated pixels. The pixels were summed for each optical slice and multiplied by the x-y pixel area and the z (0.42μm) step size to calculate the cell volume before and during AFM indentation.

SCANNING ELECTRON MICROSCOPY

All imaging was performed on a JEOL 7401 high resolution field emission scanning electron microscope (JEOL, Herts, UK). Prior to imaging, cantilevers were coated with platinum-palladium using an ion beam coater. Images were acquired with a 35˚ tilt to allow visualisation of cantilever tip profiles.

iv. RESULTS

To verify the validity of AFM-based cellular elasticity measurements, I decided to utilise MDCK epithelial cells that form confluent cellular monolayers with a large thickness (~8-10 μm). These cells allow for easy determination of the indentation depth by confocal microscopy and their large height reduces errors of elasticity measurement due to the limited thickness of the cells (117). First, I verified the elastic modulus of cells stably expressing PH-PLCδ-GFP and wild-type cells when measured with a spherical tip (322±97 Pa and 380±107 Pa respectively, N=110 cells in each case). Next, I showed that measurements obtained on the same cells on the same day with pyramidal tips gave ~2-fold higher elasticities than with spherical tips for both the WT and PH-PLCδ-GFP cells (*Figure 23*, target force 0.4nN, p<0.01 for both cell types). To exclude any error arising from unknown tip geometry, I imaged cantilever tips after the experiment using scanning electron microscopy (SEM, Figure 1 b, c). Both had the expected geometry (pyramidal tip height of ~2 μm and spherical tip radius of 7.5μm). It is a good assumption that only small errors occurred in the measurement of tip-sample separation (a closed loop control parameter measured by a strain gauge) and cantilever deflection (AFM parameter). Hence, any discrepancy in the measured elastic modulus must arise from the estimation of the contact point, the contact area, or the cellular Poisson ratio, and therefore I examined each of these possibilities.
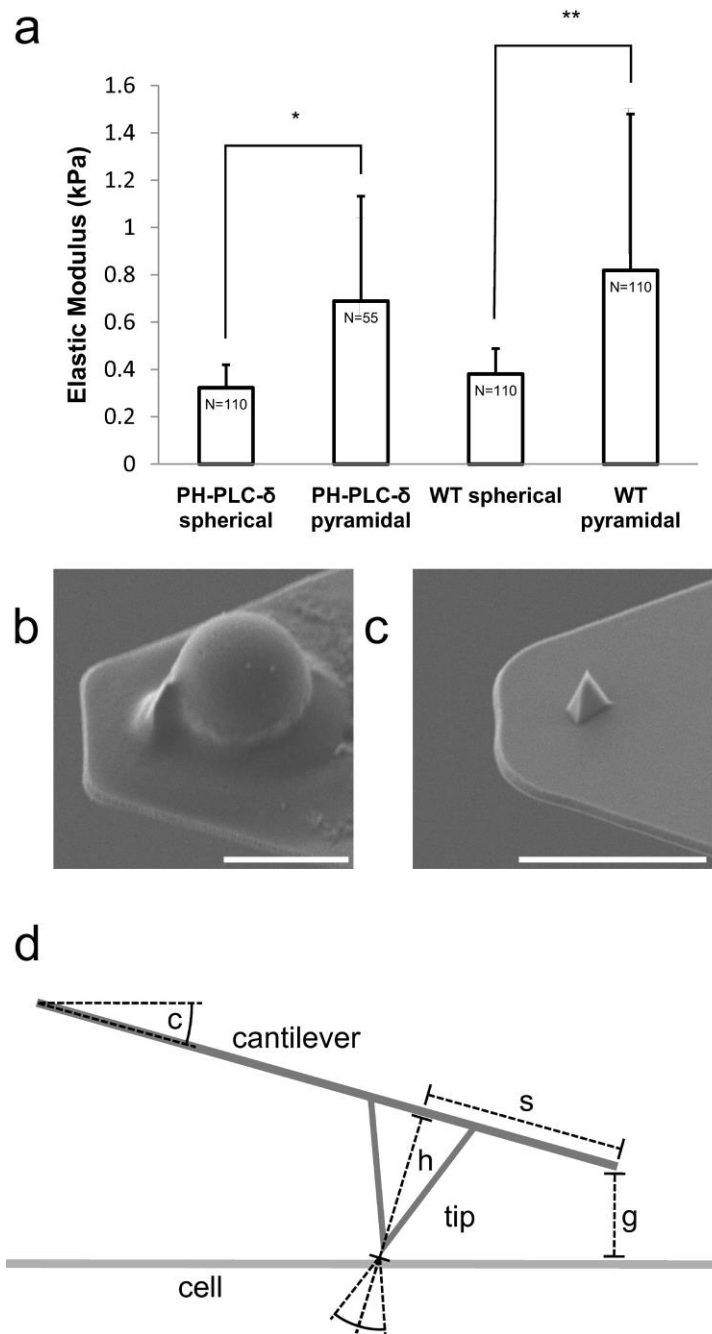
Figure 23 : Pyramidal tips and spherical tips give significantly different values of elasticity for the same cells.

(a) The elastic modulus of MDCK cells measured with cantilevers with pyramidal tips is greater than values obtained from cantilevers with spherical tips (for PH-PLCδ cells $E_{spherical}$ = 322±97 Pa, $E_{pyramidal}$ = 689±444, p*<0.01, and for WT cells $E_{spherical}$ = 380±138 Pa, $E_{pyramidal}$ = 819±660 Pa, p**<0.01). (b) Scanning electron Microscope image of a spherical tipped cantilever used in the confocal and AFM measurements (scale bar = 10μm). (c) SEM image of a pyramidal tipped cantilever (scale bar = 5μm). (d) Simple geometric considerations allow calculation of the clearance g between the cell and the end of the cantilever. This clearance is the maximum indentation depth that can be used in force measurements. g: clearance between the cell and the end of the cantilever, s: distance between the tip centre and the cantilever edge, c: angle between the horizontal and the cantilever, h: height of the pyramidal tip.

SPHERICAL-TIPPED CANTILEVERS ALLOW FOR CORRECT ESTIMATION OF CELLULAR ELASTICITY

Firstly, I extracted the indentation depth made with the spherical indenter from confocal images of the cell profile before and during indentation (**Figure 24** A-C). For each point along the x-axis I extracted the position of the cell membrane before and during indentation (**Figure 24** B), with the maximal displacement of the membrane being the indentation depth (**Figure 24, Materials and Methods**). I compared the indentation depths evaluated with this method and those obtained from AFM force-curve fitting. Both gave similar values for a range of applied forces (0.2-3.0nN) and depths measured by confocal microscopy plotted against depths measured by AFM force-curve fitting were well fitted by a straight line of slope 1 (r^2=0.87, **Figure 24** D). This confirms that the force-curve fitting algorithm I was using accurately determines the point of contact between the cell and the cantilever, and hence the indentation depth.

I then fitted the indentation depth data from force distance curves with a hertz model for spherical indentation (**Figure 24** E). This fit yielded a Young's modulus of 301Pa, close to the value obtained when fitting AFM force-indentation curves directly. However, it is possible to see that at low indentation depths the quality of the fit is poor. The Hertz model assumes contact between perfectly smooth objects. In reality the surface of cells is not flat and is covered in membrane ruffles and other structures. The surfaces of epithelial cells are covered in small actin rich protrusions called micro-villi that increase the apical surface area. These heterogeneities make the elasticity and indentation depths poorly defined at small forces as these structures bend and deform, leading to a systematic deviation of the data from the model. For the majority of the data points and for force indentation data at a well-defined range of indentation depth the Hertz model provides an accurate description.
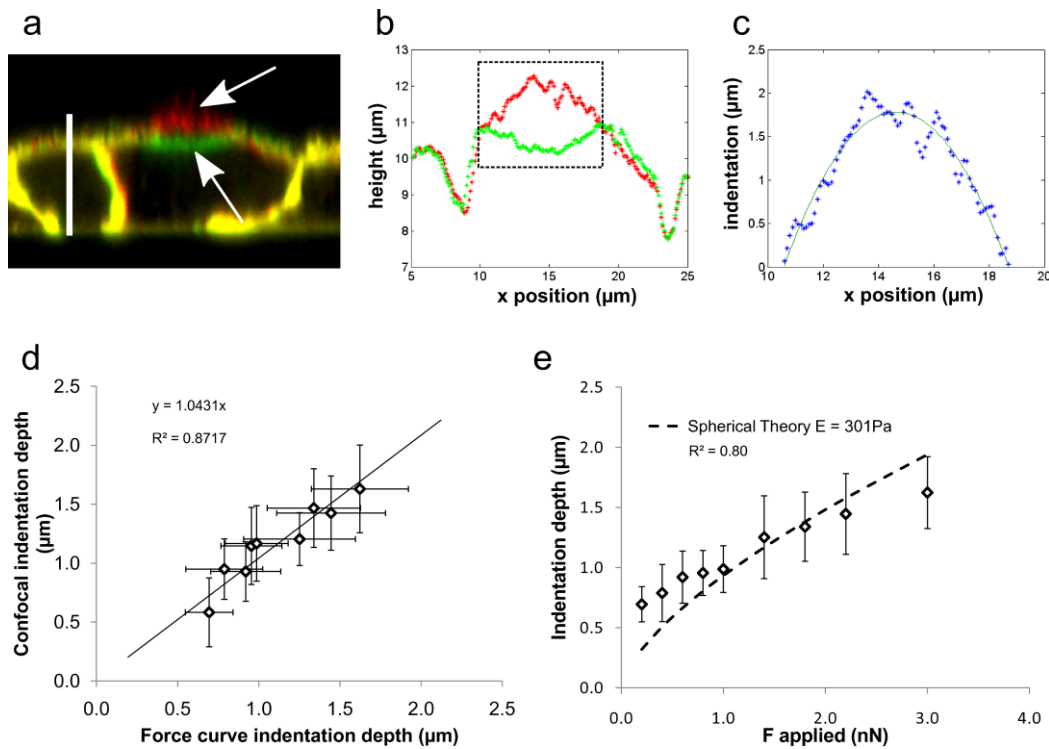
Figure 24 : Spherical tipped indenters correctly measure cell elasticity

(a) Colour combined image of the membrane profile of a cell prior to (red) and during (green) indentation with a spherical tip (scale bar=10μm). Areas where the cell has not been deformed are visualised in yellow and areas where the cell membrane has been displaced by indentation can clearly be identified by the difference in localisation of the red (before indentation) and green (during indentation) channels (arrows). (b) The absolute position of the membrane can be tracked by fitting a Gaussian function to the intensity profile in the z direction for each x position. The peak of the fit is taken to be the position of the membrane before (red) and during (green) indentation. (c) The difference in cell profiles (blue) can be fitted with a parabola (green) to find the maximum indentation depth. (d) Indentation depths measured using confocal microscopy or estimated from the AFM force-distance curves were well correlated indicating that the contact point is correctly determined from force-curve analysis. N=20 measurements for each data point. (e) The optical microscopy determined indentation depth as a function of applied force can be fitted with the Hertz model for a reduced tip radius of curvature R=4μm and a Poisson ratio of 0.5 yielding an elastic modulus of E=301 Pa, r²=0.80. N=20 measurements for each data point.

Next, I asked whether the geometry of contact between the cell and the indenter was spherical. Isosurface rendering of confocal stacks revealed that the contact area was a spherical cap for all of the forces examined (***Figure 25***). These data suggest that for spherical indenters one can correctly infer the geometry of contact between cell and tip solely from knowledge of the sphere radius and the depth of indentation. To test this further, I fitted the confocal microscopy measurements of the indentation depth as a function of applied force using the Hertz contact model. Using a reduced indenter radius R_r=4μm to account for cell curvature and a Poisson ratio v=0.5, my

experimental data was best fit to the theoretical model for an elasticity E=301 Pa (*Figure 24* , r^2=0.80, N=20 measurements for each data point), comparable to the original measurements using AFM only.

PYRAMIDAL TIPS OVERESTIMATE CELLULAR ELASTICITY FOR FORCES OVER 0.4NN

Using the same approach, I qualitatively examined the contact geometry between pyramidal-tipped cantilevers and cells for the same range of forces. For low forces, the contact between the indenter and the cell membrane displayed a clear pyramidal shape (0.2 nN, *Figure 25*) though the cantilever underside appeared in close proximity to the cell membrane.
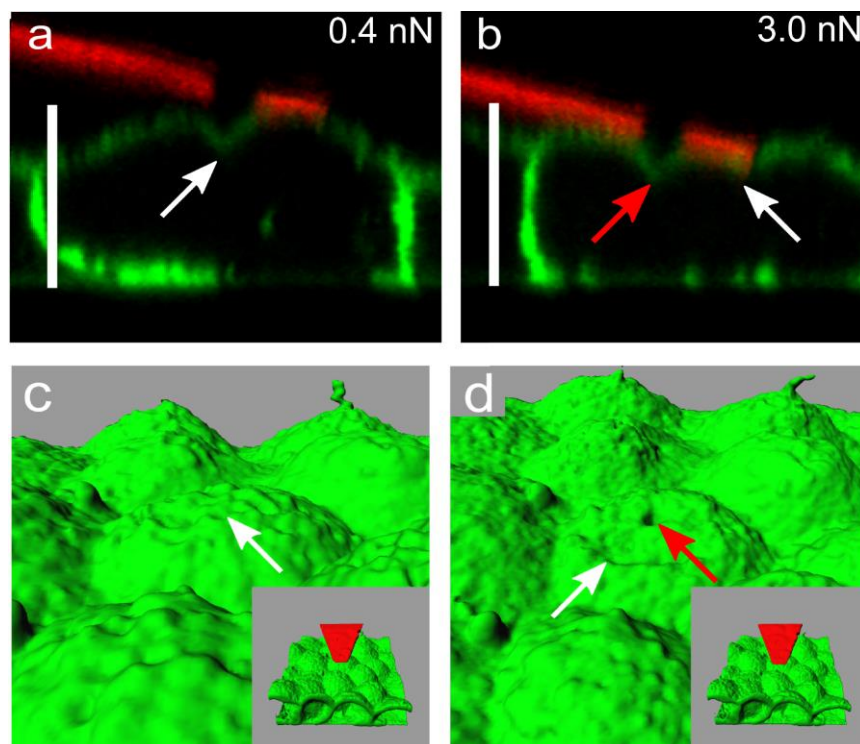
Figure 25 : Qualitative analysis of the contact geometry.

(a) At low applied force (0.2nN), the indentation in the cell membrane is solely due to the pyramidal tip (arrow). (b) At higher forces (3.0nN), the contact area is increased by additional contact between the underside of the cantilever and the cell surface (arrows). (c, d) 3D iso-surface reconstructions of the cell surface show that at low forces (0.2nN) contact geometry is pyramidal (c, red arrow) but that at higher force the underside of the cantilever beam comes into contact with the cell in addition to the tip (d, tip: red arrow, cantilever underside: white arrow). Scale bars = 10μm.

At larger forces, the cantilever underside clearly came into contact with the cell apex in addition to the tip and this was very apparent in isosurface reconstructions (3 nN, *Figure 25*). This suggested that even for forces routinely utilised for elasticity measurements (1-10nN), the contact area between the cell and the cantilever can have contributions both from the pyramidal tip and from the cantilever underside.

I assessed what influence this extra contact area had on elasticity measurements. Firstly, I verified that the curve fitting algorithm correctly determined the depth of indentation for cantilevers with pyramidal tips. Indentation depths extracted from confocal images correlated well with depths extracted from AFM force-curves (*Figure 26*, r^2=0.54) suggesting that the contact point is correctly identified. Second, I plotted the indentation depth measured by confocal microscopy as a function of force applied. Fitting this curve with the theoretical relationship for pyramidal indenters gave an elasticity E=785Pa (*Figure 26*, r^2=0.90), ~two-fold larger than for spherical indentations but similar to that obtained directly from AFM measurements. As I had confirmed that spherical-tips correctly measure elasticity, I plotted the theoretical indentation depth for a pyramidal tip on a material of elasticity E=301 Pa (*Figure 26*). At low forces, the indentation depth measured by optical microscopy was close to that predicted for the elasticity measured using spherical indenters, whereas at high forces the indentation depths measured by microscopy were significantly smaller than predicted for a pyramidal indentation of the cell (*Figure 26*). Inspection of the contact area geometry pointed to an explanation for these results: at low forces, the contact area was pyramidal indicating that only the tip contacted the cell surface, whereas at high forces it was not. Careful examination of my images of cell indentation with pyramidal cantilevers revealed close apposition between the cantilever underside and the cell surface for the full force range, suggesting that the cantilever contacts the cell in addition to the tip. This was particularly apparent at high forces (*Figure 26*) and lead to an underestimation of the contact area resulting in an overestimation of elasticity. Next, in view of the large area of contact between the cantilever underside and the cell at high forces, I asked if the experimental depth versus force curve might be better approximated by using a theoretical relationship for indentation by a flat ended cylindrical punch with radius

a=5μm, comparable to the area of contact between the cantilever underside and the cell (estimated from *Figure 23*). For flat ended punches, the force F scales as (116):

$$F = \frac{2Ea}{(1 - \upsilon^2)}\delta$$

with *E* the elasticity, *a* the contact radius, *δ* the indentation depth, and *ν* the Poisson ratio.
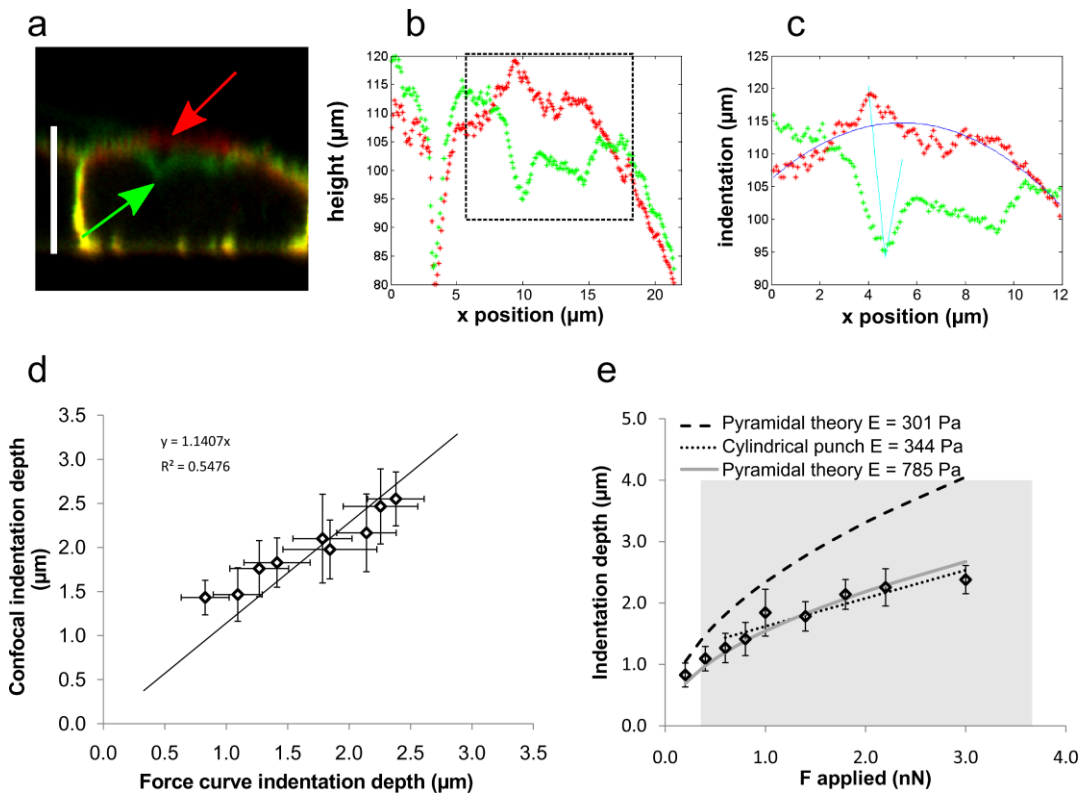
Figure 26 : At high forces the area of contact for pyramidal tips can be underestimated

(a) Membrane profile of an MDCK cells expressing PH-PLCδ before (red) and during (green) indentation with a pyramidal cantilever with a force of 3.0 nN (b) Membrane profile of the cell before (red) and during (green) indentation by a pyramidal tipped cantilever for the cell shown in a. (c) The indentation depth is found by fitting the indented profile with the x-z profile of the pyramidal tip. (d) The indentation depth measured by confocal microscopy correlates well with the indentation depth estimated from AFM force-distance curves, R^2=0.54. Each data point represents the average of N=20 measurements. (e) Indentation depth as a function of force applied. The indentation depth plotted as a function of applied force (diamonds) did not follow the theoretical model for a pyramidal indenter for a material of E=301 Pa at high forces (indicated by the grey region). Instead the behaviour tended towards that of a flat ended cylindrical punch plus an offset from the pyramidal tip indentation. Each data point represents the average of N=20 measurements.

Fitting this theoretical relationship to my experimental data (*Figure 26*) yielded a good fit at higher forces for an elasticity of E=344 Pa (r^2=0.92), comparable to the elasticity measured with spherical indentation. At higher forces, the indentation depth increased linearly with force as expected from the above scaling (*Figure 26*).

POISSON RATIO MEASUREMENTS

Finally, to determine the cellular Poisson ratio, cells expressing GFP in their cytoplasm were seeded into a mixed monolayer and cell volume was measured with confocal microscopy before and during AFM indentation. I chose an indentation force large enough to yield an indentation of ~ 10% of the cell volume. Cell volume was identical before and during AFM indentation (*Figure 27*, p=0.79). Isosurface reconstruction of the cell volume before and after indentation showed that the cell bulges outwards when compressed by the microsphere (*Figure 27*). These data suggest that a Poisson ratio of 0.5 is a good estimate calculating the elasticity of MDCK cells. Although the volume measurements obtained with confocal microscopy are only accurate to ~10%, small uncertainties in the value of the Poisson ratio do not have a large impact on the final value of the young's modulus that is obtained. This source of uncertainty is not larger than the heterogeneities between cells that provide a much larger contribution to deviations in elasticity data.
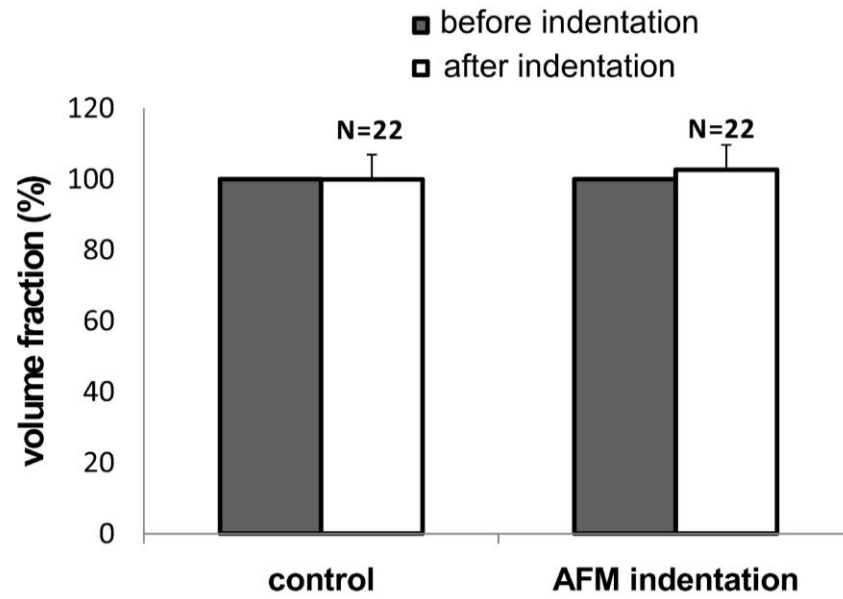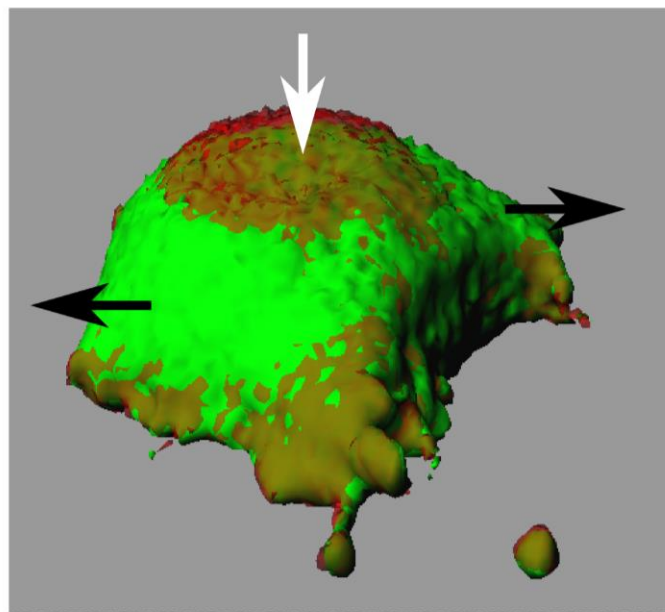
Figure 27 : Measurement of cell compressibility

(a) Cell volume is conserved before and during indentation indicating that the cell is incompressible (p=0.79) and that a Poisson ratio of 0.5 is a good assumption when measuring elasticity. Typically there is a 10% error on measurements of cell volume using this method. N=22 measurements for each case. (b) Colour combined images of cell before (red translucent) and during AFM indentation (green). Reconstructions of the cell volume show that under large indentation the cell bulges outwards to conserve its volume (before = red, white arrow, during = green, black arrow). MDCK cells used in these experiments were typically 8μm tall and a diameter of 15μm. Assuming a typical columnar shape the expected volume is ~1500μm³.

CYTOSKELETAL CONTRIBUTIONS TO CELLULAR ELASTICITY

Having shown that elasticity measurements with pyramidal tips overestimate cellular elasticity even at low forces, I re-verified the effect of drugs perturbing the cytoskeleton and contractility on cellular elasticity using spherical indenters (*Figure 28*). Depolymerisation of the F-actin cytoskeleton with Cytochalasin D (20 µM) and Latrunculin B (750nM) led to an approximately two-fold decrease in elasticity ($E_{Cytochalasin}$ = 147±73 Pa, p*<0.01, $E_{Latrunculin}$ = 227±106 Pa, p**<0.01). Depolymerisation of microtubules with Nocodazole (10µM) did not have such a dramatic effect but nonetheless reduced cellular elasticity significantly ($E_{Nocodazole}$ = 285±106 Pa, p***<0.01). Drugs disrupting cellular contractility either by inhibiting myosin II ATPase (Blebbistatin, 50µM) or Rho-kinase activity (Y27632 ,10µM) did not affect cellular elasticity ($E_{Blebbistatin}$ = 377±129 Pa, P=0.65, E_{Y27632} = 380±165 Pa, p=0.85).

ACCURATE MEASUREMENTS WITH PYRAMIDAL TIPS

Pyramidal-tipped cantilevers offer high spatial accuracy and hence achieving reliable measurements of cellular elasticity with these remains a highly desirable outcome. When using standard pyramidal tips (1-2 µm height), a threshold indentation depth δ_{max} can be chosen based on the clearance g between the tip apex and the cantilever beam edge as well as the angle of the cantilever to the horizontal (*Figure 23* D). Using indentation depths below δ_{max} ensures that all contact area is entirely due to the pyramidal tip. Simple geometrical considerations show that this threshold can be calculated as:

$$g = h \sin(\pi - c) - s \sin(c)$$

With g the clearance, s the distance between the tip and the cantilever edge, h the height of the tip, and c the angle between the cantilever and the horizontal (*Figure 23* D). As a proof of principle, I fitted force distance curves up to an indentation depth of ~0.6µm (resulting from indentation forces up to ~0.06 nN) and obtained an elastic modulus of 499±407 Pa for wild-type MDCK cells, not significantly different from those obtained by spherical shaped indenters (p=0.15, *Figure 28*).
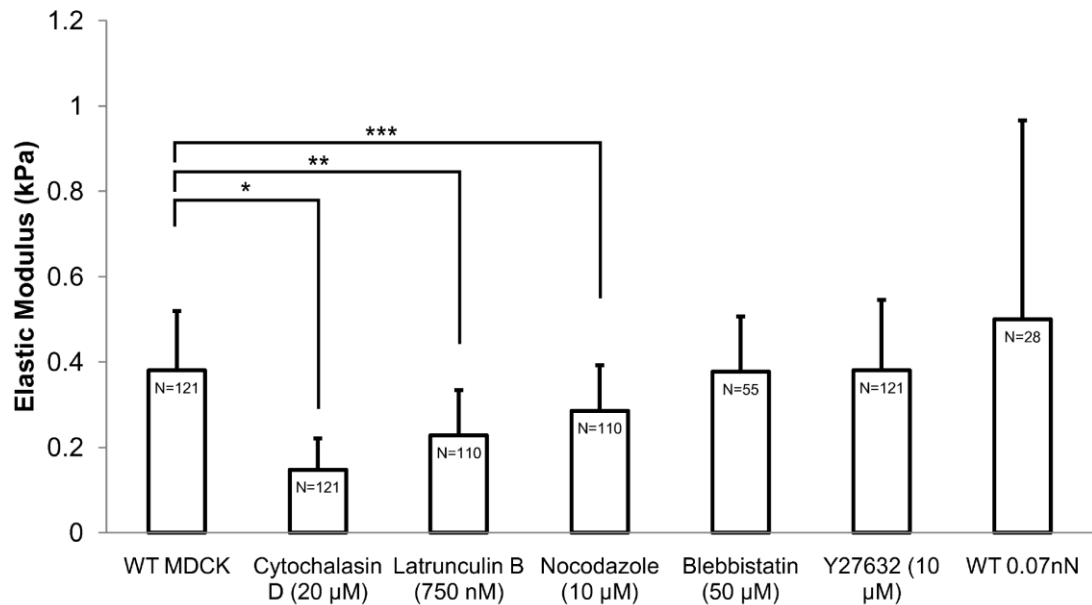
Figure 28 : Effect of drug treatments on cellular elasticity

(a) Depolymerising actin filaments with cytochalasin D and latrunculin B caused the most noticeable effects on the cell elastic modulus decreasing it approximately two-fold. Depolymerising microtubules with Nocodazole only caused a small but significant decrease in elasticity (-25%, p<0.01). Inhibiting contractility with Blebbistatin and Y27632 did not have a significant effect on the cell elastic modulus. Fitting force curves obtained from control cells using pyramidal tipped cantilevers up to ~0.6μm indentation depth gave an elastic modulus close to that obtained with spherical tips (p=0.15). The number of measurements performed for each experiment is displayed on the respective bar. Each measurement is performed on an individual cell and was repeated on three different days with fresh samples.

v. DISCUSSION

AFM has become the method of choice for measuring cellular elasticity, however values of cellular elasticity reported in AFM measurements are large compared to those reported by other methods and measurements performed using spherical tips give significantly lower elasticities than pyramidal tips. I have provided the first in-depth experimental validation of AFM-based cellular elasticity measurements and show that measurements with spherical-tipped cantilevers provide a more accurate measure of elasticity, whereas measurements with pyramidal-tipped cantilevers can lead to extraneous contact between the cantilever and the cell surface if the target force is set too high. This leads to an overestimation of the measured elasticity. I identified three possible sources of error for AFM based elasticity measurements: i)

errors in measurement of indentation depth, ii) errors in estimation of tip-cell contact area, iii) errors in the cellular Poisson ratio. Firstly, I experimentally validated the fitting algorithm used to detect contact between the cell and the cantilever by measuring AFM indentation depths using confocal microscopy and comparing these to indentation depths obtained from AFM force-distance curves for a range of applied forces (0.2-3.0nN). Both methods gave similar values showing that the fitting algorithm used (146) correctly identified the point of contact and hence indentation depth for both spherical and pyramidal tips. The main benefit of being able to use an automated fitting algorithm is that it increases data throughput in comparison to having to manually identify the contact point in each curve. Typical automated methods include using the first and second derivatives of smoothed data in order to identify the contact point. The major issue with the method is that the force curves can often be noisy making identification of the correct derivatives difficult. The method that I used (described by David C Lin (121)) involves sequentially moving through the dataset and finding the best fit as if each data point was the contact point. The fit with the lowest mean square error will have the contact point in the correct position. The method however requires analysis of fitting for all of the points in the dataset in turn and can become time consuming for large amounts of data. However, my experimental measurements have shown this to be a reliable way of automatically determining the contact point in AFM force-curve data.

Having verified the quality of the curve fitting algorithm (by showing a good agreement between the indentation depths obtained using AFM and confocal microscopy, *Figure 24* d), I used confocal microscopy to examine tip-cell contact geometry during indentation. For spherical tips, the tip-cell contact area was a spherical cap as expected and fitting the indentation depths determined by confocal microscopy versus force applied gave an elastic modulus similar to that derived by fitting force distance curves. In contrast, for pyramidal tips, the tip-cell contact area was pyramidal at the lowest force examined (0.2nN) but for larger forces it was not. Indeed, in addition to the pyramidal contact expected from the cantilever tip, the underside of the cantilever came into contact with the cell, even dominating at high forces (*Figure 26*). This led to an underestimation of the contact area and indentation depth for a given force, errors that translated into an overestimation of the cellular

elasticity. Unlike previous measurements, my validated measurements with spherical tips were comparable in magnitude to elasticities obtained using other measurement methods such as micropipette aspiration or micro rheology (100-500 Pa (137), (138)). Having shown that elasticity measurements performed using pyramidal tips can lead to errors in measurement, I re-examined the effect of drugs that disrupt the cytoskeleton or inhibit contractility on cell elasticity using spherical-tipped indenters. In line with measurements performed by others, I confirmed that drugs that depolymerised the F-actin network reduced the cell elastic modulus approximately two-fold. I found that disrupting microtubules using nocodazole led to a small (-25%) but significant decrease in cellular elasticity. Such a subtle decrease would certainly be overlooked in conditions where the tip-cell contact area is poorly controlled and point to a small contribution of microtubules to cell mechanics.

The high spatial accuracy afforded by pyramidal-tipped cantilevers makes it a desirable tool for mapping spatial variations in cellular elasticity. Mapping the spatial variation in elasticity arising from small mesh structures such as the apical actin network is not possible due to the small mesh size (~30 nm) and the large contact area between the AFM tip and the soft cell. However, it is possible to map the local stiffness of the cell which coincides with much larger actin rich bundled structures such as stress fibres. In the case of epithelial cells it is possible to see enriched actin adherens junctions which are stiffer than the main body of the cell (13, 144).

However, great care needs to be used in making local elasticity measurements and interpreting them. The highly varying cell surface topography at cell junctions or at large local structures such as stress fibres means that it is difficult to avoid contact errors (*Figure 29*). There are two approaches to avoid errors due to extraneous contact between the cantilever underside and the cell surface. First, the clearance between the tip apex and the underside of the cantilever could be increased by using very long tips (several microns). This would ensure that contact with the cell is solely due to the cantilever tip. When using the more common shorter tips (1-2 μm), I have shown that setting a threshold indentation depth based on the clearance between the cantilever and the cell surface allows for correct measurements,

assuming that the surface is flat. Further precautions should be taken when making local AFM measurements.
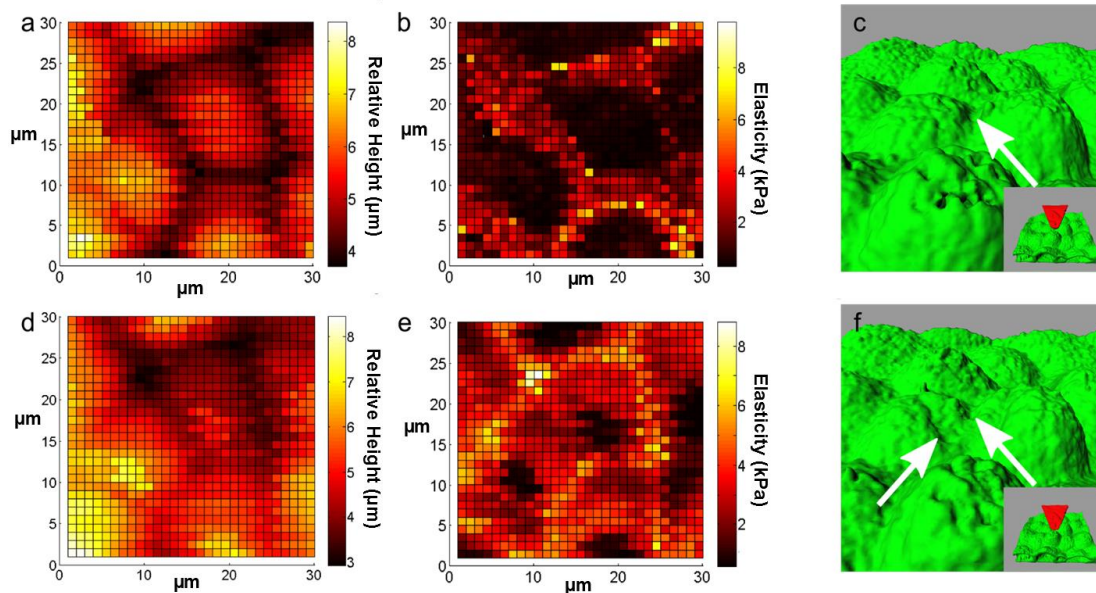
Figure 29 : Mapping of MDCK mechanical properties at different applied forces

Height maps at an applied force of 0.4nN (a) and 3.0nN (d) respectively, and their corresponding elasticity maps (b and e). At low applied force, a larger elastic modulus between cells coincides with the localisation of actin rich adherens junctions (13, 144). At higher applied forces the junctions appear broader (e). This is an artefact that arises from extraneous contact between the cantilever and cell the surface. (c, f) Confocal images of the cell membrane at low and high applied forces. (c) At low applied force the indentation made by the tip into the cell membrane has a well-controlled shape. (f) At higher applied forces the cantilever beam touches the sample causing an increase in the force exerted onto the cantilever and hence a higher apparent elasticity.

vi. SUMMARY

I have outlined some of the potential sources of error in measuring the elasticity of cells using atomic force microscope based indentation measurements. With the increasing number of researchers interested in cell mechanics and interdisciplinary research, it is vital to standardise measurement protocols to avoid erroneous measurements. In addition to using spherical tipped cantilevers, considerations must be made about the level of force and indentation that are used to avoid contact between the cantilever underside and the cell as well as to minimise any influence from the stiffness of the substrate that cells are plated on. Particular care needs to be taken with samples that have a highly varying topography or that are very soft. Outlining the protocols used to measure cell elasticity and exposing them to constant

review will help increase measurement accuracy and consistency on different cell types, and allow comparative between research groups. This will be of particular benefit to researchers working at the interface between biology and physics.

6. THE EMERGENCE OF MONOLAYER TISSUE LEVEL MECHANICAL PROPERTIES COINCIDES WITH THE FORMATION OF ADHERENS JUNCTIONS

i. ACKNOWLEDGEMENTS

I would like to thank Alicia Daeden, a masters student whom I worked with on this project and who contributed equally to the work in this chapter. Guillaume Charras created the cell lines used in this research.

ii. INTRODUCTION

In spite of our understanding of the biological mechanisms for intercellular junction formation, little is known about how tissue-scale mechanical properties evolve or to what extent each type of junction contributes. This is primarily due to the lack of non-destructive approaches enabling measurement of supracellular mechanical properties and their temporal evolution during the transition from isolated cells to strongly linked monolayers. Indeed, the presence and relative scale of intercellular tension within epithelia is usually probed using laser ablation, an approach that cannot be used to repeatedly interrogate the same region of interest because of its destructiveness (147). Intercellular junctions are dynamic structures allowing neighbour exchange and re-arrangement in collective cell migration and development. Therefore understanding the establishment of new intercellular junctions, the recruitment of proteins to intercellular junctions and their maintenance is important in our fundamental understanding of collective cell behaviours.

To measure the evolution of monolayer mechanical properties with the formation of intercellular junctions, I monitored the apparent rigidity of epithelial cell monolayers cultured on soft collagen gels using deep Atomic Force Microscopy (AFM) micro-indentation. Time-resolved measurements of the apparent rigidity of monolayer-gel composites combined with localisation studies and perturbation by chemical inhibitors showed that supracellular tissue-scale monolayer mechanical properties

emerged over the course of two hours and correlated with the formation of adherens junctions but not desmosomes.

iii. MATERIALS AND METHODS

GENERAL

AFM measurements and confocal measurements were performed using Leibovitz-L15 CO2 independent medium supplemented with 10% FBS. All measurements in this chapter were conducted at room temperature, but samples were returned to the incubator between measurements in time-course experiments.

CELL CULTURE: REPLATING ASSAY

To observe junction reformation measurements were made 30-40 minutes after plating 7 million cells onto a collagen gel coating the bottom of 50mm petri dish, a number of cells sufficient to yield a confluent monolayer. During this initial period, cells attached strongly to the substrate but did not reform intercellular junctions. Subsequently, the formation of intercellular junctions was followed with confocal microscopy and changes in monolayer apparent rigidity could be followed by AFM. Inducing cellular junction reformation with a calcium switch showed qualitatively similar results to the replating assay.

MEASUREMENT OF MONOLAYER APPARENT RIGIDITY

To measure monolayer supracellular properties, I utilised a specialised Atomic Force Microscope with a piezoelectric ceramic with a 100μm z-range (JPK CellHesion 200, JPK, Berlin, Germany) interfaced to an inverted microscope (IX-71, Olympus, Berlin, Germany). The long z-piezo range of this system facilitates indentation with large depths and ensures complete separation of the cantilever tip from the sample when the piezoelectric ceramic is retracted. Monolayers were deformed with AFM cantilevers with a nominal spring constant of 0.1N/m and a tip formed of a 20μm tall flat cylinder of radius 5μm (Nanosensors, Neuchatel, Switzerland). This allowed for contact with a whole single cell. Force-distance curves were acquired with an approach velocity of 5μm/s up to a target force of 25nN resulting in an indentation depth of ~15μm for cells seeded on top of a collagen gel. This indentation depth is

~2-fold larger than cell height and leads to measurable deformation field in the monolayer plane.
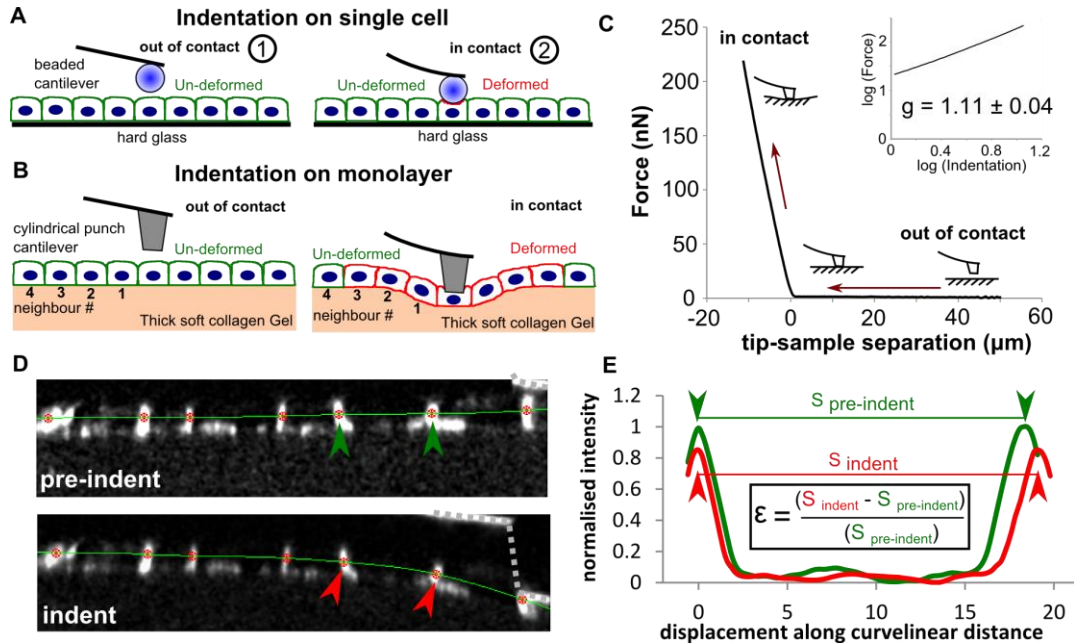
Figure 30 : Experimental setup and analysis of cellular deformation

(A) Samples are indented with a spherical tipped cantilever to a depth of ~1 μm. This signifies that deformation is localised to one single cell. The cantilever deflection as a function of indentation can be fitted with contact mechanics models to measure the stiffness of the indented cell. The small depth of indentation prevents artefacts arising from the large stiffness of the glass substrate. (B) To measure the mechanical properties of monolayers grown on gels, indentations were performed using a cylindrical punch tip up to an indentation depth of ~15μm (larger than the cell height). This induces a deformation not only in the cell contacted by the cantilever tip but also in neighbouring cells. Therefore, the measured applied force results from a combination of the cell stiffness, the monolayer supracellular mechanical properties, and the elasticity of the collagen gel. (C) Experimental force-distance curve data. At the start of approach, the cantilever is far from the sample and it is slowly lowered towards the sample. While it stays out of contact, the force applied stays constant and zero. Upon contact between the AFM cantilever tip and the sample, additional travel of the piezoelectric ceramic results in increasingly deep indentations and the force applied increases sharply with indentation depth. Force curves obtained in these experiments displayed a linear relationship between force and indentation (inset, slope = 1.11±0.04, N=26 curves), as would be expected for indentation of homogenous elastic materials in this geometry. (D) The cellular strain field away from the location of indentation was measured by analysing the displacement of intercellular junctions at mid-height in zx profiles of the monolayer using a custom written matlab routine. Confocal zx profiles of monolayers were acquired before and during indentation. Intercellular junctions could be identified morphologically as bright vertical bars in E-cadherin GFP cell monolayers. Indentation occurred on the right hand side of the images and the shape of the AFM cantilever is indicated by dashed grey lines. The location of intercellular junctions along the line profile (green line) is indicated by red dots. Green arrows indicate two intercellular junctions belonging to one cell close to the centre of indentation before indentation. Red arrows indicate the same junctions during indentation. (E) The GFP fluorescence intensity along the line profile (green line in D) could be compared before (green arrowheads in D, E) and during (red arrowheads in D, E) AFM indentation. Peaks in fluorescence intensity correspond to the location of intercellular junctions and these were used to calculate the cellular length (S), the change in cellular length (S_{indent}-$S_{pre-indent}$) and the engineering strain ($\varepsilon=(S_{indent}-S_{pre-indent})/ S_{pre-indent}$) along the curvilinear profile.

The slow approach speed used was chosen to minimise the contribution of viscoelastic properties of the system to the measured apparent rigidity. Force-distance curves were analysed using a Hertzian contact model to yield an apparent rigidity with the JPK data analysis software.

MEASUREMENT OF TEMPORAL CHANGES IN MONOLAYER APPARENT RIGIDITY

I monitored temporal changes in monolayer apparent rigidity by measuring changes in monolayer apparent elasticity using two different approaches.

First, I positioned the AFM cantilever above a chosen area and acquired force-distance curves at 2min intervals for 3h using the JPK control software. A phase contrast image of the cantilever and the monolayer was captured immediately after each rigidity measurement.

Second, I acquired measurements in multiple positions in a petri at defined time points after replating (defined time-point measurements) and returned monolayers to the incubator in between measurements. I measured monolayer apparent rigidity at 1h, 2h30, and 5h after replating. At each time point, AFM force-distance curves were collected at 5 different positions per time point in several petri dishes giving a total of over 30 measurements for each experimental condition. Each petri dish remained out of the incubator for less than 10min at each measurement time point.

PREPARATION OF COLLAGEN GELS

Collagen gels were made according to manufacturer protocols in a 7:2:1 ratio of collagen (Nitta Gelatin, Japan): 5x DMEM (PAA, Germany): reconstitution buffer (4.77 g HEPES and 2.2 g NaHCO3 in 100 ml of 0.05N NaOH). The solution was mixed on ice before transfer to 50mm glass bottom petri dishes (Intracell, UK) and gelation at 37°C for 30 minutes before use. Gels of different thicknesses were made according to the type of experiment.

For confocal imaging thin gels were generated to accommodate the short working distance (~300µm) of high magnification objectives (UPLSAPO, 60x water immersion, N.A. = 1.2, Olympus). To do this, 350µl of Cell matrix type I-A solution

was mixed with 100 µl of sterile 5x Dulbecco's Modified Eagle Medium and 50µl of sterile reconstitution buffer on ice. Then, 550µl of the reconstituted collagen solution was placed into a 50 mm glass bottomed petri dish (Intracell, Herts, UK) covering the entire glass surface of the dish. The majority of the solution was removed to obtain a thin collagen gel (>100µm thick) and incubated at 37°C for 30 minutes to allow for gelation. The collagen gel was washed with culture medium and cells were seeded onto it.

For AFM measurements thicker gels are required to allow approximation as elastic half planes under large indentation. Collagen gel solution was made as previously described but a volume of 775µl was deposited in the petri dish and left to gel, giving a thickness >200µm.

To conserve reagents when transfecting cells by electroporation, miniaturised gels were created covering a smaller area of the glass bottom dish surface. Silicon elastomer rings (Quicksil, World precision instruments, Florida USA) ~0.5cm in diameter were attached to the base of the culture dish. 20µl of reconstituted collagen solution was deposited within the ring, left to gel, and washed with 40µl of culture media.

To image the reformation of intercellular junctions following a calcium switch, low calcium gels were made. Calcium was removed from FBS and from 5xDMEM by adding 0.06g/ml of Chelex beads to these solutions (Chelex 100 Sodium Form, Sigma). Solutions containing Chelex beads were left in the fridge overnight with constant agitation, and sterilised by filtration through a 0.2µm filter (Appleton woods, Birmingham, UK).

MEASUREMENT OF INDENTATION DEPTH AND STRAIN FIELD IN THE MONOLAYER WITH COMBINED AFM AND CONFOCAL MICROSCOPY

For combined AFM-confocal measurements, a specialised microscope platen was fitted onto the confocal microscope stage to interface with the AFM head (JPK). All imaging was carried out with a 60x water immersion objective (UPLsapo, N.A. = 1.2, Olympus). To image the cantilever shape, a 10,000 MW fluorescent dextran (alexa 647, Invitrogen) was added to the medium and imaged by exciting the dye

with a 647nm laser and collecting light at 680nm. The cantilever tip appeared as a dark shadow against the bright medium. GFP in the cells was excited with a 488nm laser and light was collected at 525nm. The AFM tip was brought into contact with the cell layer. The AFM tip was then lowered into the cell layer to create a ~15 μm deep indentation using the AFM manual stepper motors. The resulting indentation and deformation of the cell layer was visualised by taking an X-Z profile image (with a pixel size of 0.2μm by 0.2μm).

ANALYSIS OF CELLULAR DEFORMATION PROFILES RESULTING FROM DEEP AFM INDENTATION

Confocal images were acquired before and during AFM indentation. Images were analysed using custom software written in Matlab (Mathworks, Natick, MA, USA). Briefly, images were imported into Matlab and a line profile drawn following the base of the cells. This line of interest was smoothed and its points interpolated using a cubic spline. The displacement along the line was measured by measuring the Euclidean distance at each pixel. Intercellular junctions along the lines were identified as local maxima in fluorescence intensity along the line profile. The strain in cells within the monolayer could then be measured as the relative change in length between junctions before and during indentation.

STATISTICS

Values within the text are given as mean±standard deviation and statistical significance determined using a student's T-test, where statistical significance was assumed when $p<0.01$. Data in charts are displayed as box and whisker plots showing the median, 1st quartile, 3rd quartile represented by the box and maximum, minimum represented by the whiskers.

iv. RESULTS

AFM MICRO-INDENTATION CAN PROBE TISSUE-SCALE MECHANICAL PROPERTIES

I reasoned that by applying deep indentations onto cell monolayers growing on soft substrates, I should be able to probe the supracellular tissue-scale mechanical properties of monolayers (*Figure 30*). In my experiments, I used MDCK II cells as a

junction-forming epithelial cell model and cultured them on top of thick collagen gels (thickness~200µm) with an elasticity seven-fold lower than that of the cells ($E_{collagen}$=66±8Pa) (11, 12). I measured the mechanical properties of monolayer-gel composites using cantilevers with a cylindrical tip giving a constant contact area of a size similar to the cellular apical surface area. Indentations larger than the monolayer thickness (~10-15µm) induced a deformation field that propagated through intercellular junctions over several cell diameters (***Figure 31***).

MONOLAYER-GEL COMPOSITE RIGIDITY

The restoring force opposing deformation results from a combination of the indented cell stiffness, the monolayer supracellular mechanical properties, and the collagen gel elasticity. As a mechanical indentation problem, this is reminiscent of a tensed membrane (148) or a thin stiff film (149) on a soft elastic half space. However, determining the relative contributions of monolayer tissue-scale planar elasticity (41), pre-stress (150) and tension poses a difficult theoretical challenge. The force applied by the AFM cantilever at any given indentation depth is resisted by the restoring forces due to elasticity of the cell contacted by the tip, by tension in the monolayer (76), by elastic deformation of the monolayer, and by elastic deformation of the collagen substrate. To my knowledge there is no widely accepted analytical formula for determining all the film properties from the indentation data. Asides from analysing the stress distributions, this problem is further complicated by the multiple factors that contribute to apparent monolayer rigidity including: anisotropies in elasticity within the monolayer (28, 41), the monolayer Poisson ratio, cellular tension/pre-stress resulting from myosin contractility (34, 151), as well as force-coupling between cells (18, 76) and between cells and the substrate (102). Although some finite element models of this indentation problem do exist (149, 150) I did not pursue this, choosing to focus on the biological aspects of the research. A finite element model and further data analysis would be a valuable avenue of future research to understand the different mechanical contributions to the monolayer-gel composite rigidity.
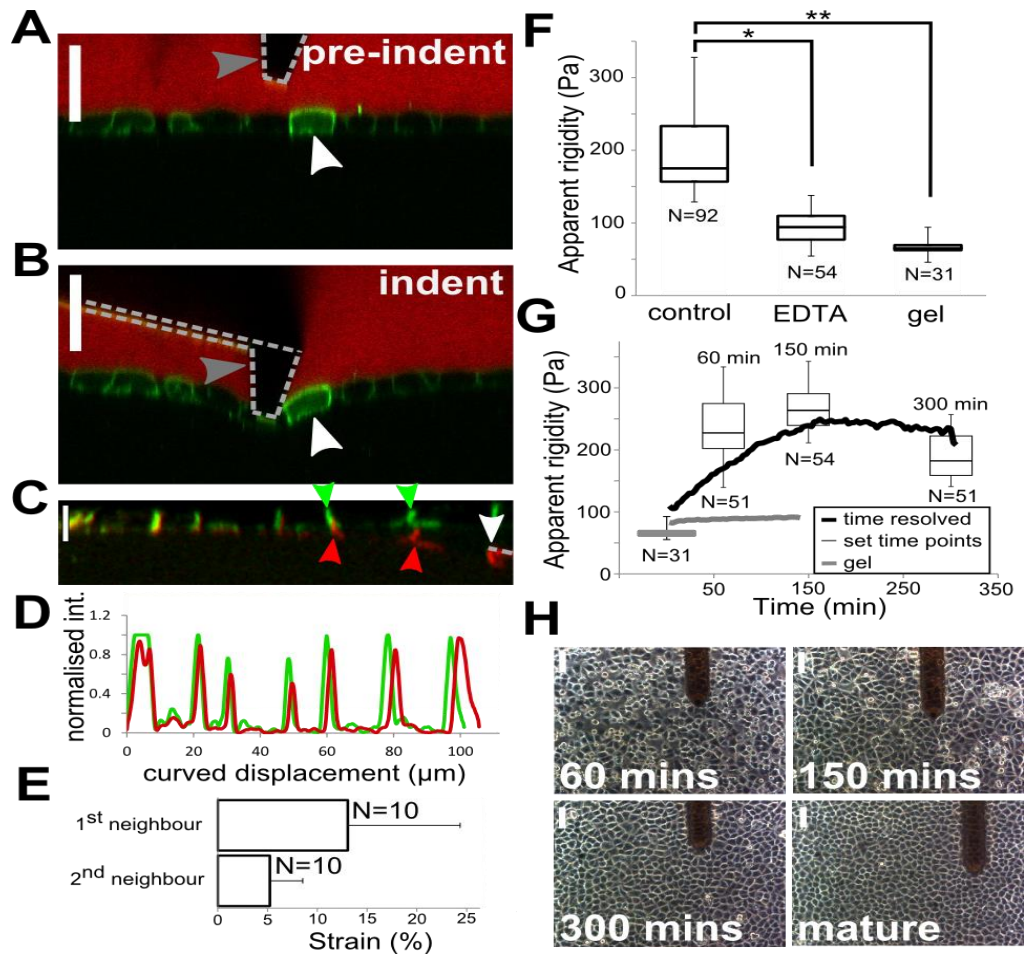
Figure 31 : the emergence of monolayer supracellular mechanical properties coincides with the formation of intercellular junctions.

(A-B) Confocal profiles of a cell monolayer grown on a soft collagen gel, before (A, s.b=20μm) and during (B, s.b=20μm) AFM indentation. Indenting the monolayer to a depth at least equal to the cell height induced a strain field in the plane of the monolayer, evident from the deformation of intercellular junctions in profile images (arrowhead, A-B). The monolayer (green) is visualised through expression of a GFP-tagged membrane marker and the profile of the AFM cantilever is visualised through exclusion of a fluorescent dye added to the extracellular medium (red). (C) Monolayer profile before (green) and during indentation (red). Arrows indicate the position of intercellular junctions in cells expressing GFP-tagged E-cadherin (before indentation: green arrows, during indentation: red arrows). The indentation was maximal close to the site of contact (white arrow, s.b.=10μm). (D) Fluorescence intensity along a line bisecting the monolayer shown before and during indentation. Peaks in fluorescence show the position of intercellular junctions. The cellular strain can be calculated from the change in distance between neighbouring junctions along the curvilinear deformation profile. Strain was maximal close to the indented cell and decayed with increasing distance from the site of indentation. (E) Average cellular strain in the first and second nearest cells to the centre indentation. Error bars represent standard deviations. (F) Average monolayer apparent rigidity for control monolayers, monolayers treated with EDTA, and collagen gels without cells. Dissociation of intercellular junctions by calcium chelation by EDTA led to a large reduction in monolayer apparent rigidity (p*<0.01, p**<0.01). (G) Temporal evolution of monolayer apparent rigidity obtained from time-resolved measurements (black line) or from measurements at set time-points (box plots). (H) Monolayers with mature intercellular junctions were established over the course of the first 120min of measurement. Phase contrast images of cell monolayers at different time-points after replating. The AFM cantilever is visible above the monolayer as a dark shadow (s.b.=50μm).

I chose to quantify the monolayer mechanical properties probed in my experiments as an apparent rigidity of the monolayer-collagen gel composite. This rigidity is expressed in Pascals (Pa), as in AFM measurements of single cell elasticity, to enable simple comparison between experimental conditions. Examination of experimental force-distance data revealed that applied force scaled linearly with indentation depth, as would be expected in indentation experiments of a homogenous elastic half-space with cylindrical punches. However, it is important to note here that my measurements do not represent a true Young's modulus: i) the sample has heterogeneous mechanical properties since the cells and the collagen substrate have very different elasticities (Ecollagen~60Pa and Ecells, z~400Pa) and the monolayer mechanical properties are anisotropic (Ecells, z~400Pa and Ecells, xy~5kPa at 10% strain), ii) it does not operate within the traditional small strain regime assumed by many contacts mechanics models when interpreting measurements, iii) I measured the combined mechanical contributions from tension and elasticity within the cells and the collagen substrate as well as tension between the cells and the substrate.

Despite these limitations, my experimental results indicate that deep AFM indentation of monolayer-gel layers is sensitive to monolayer supracellular mechanical properties. Indeed, deep AFM indentation induces a strain field in the plane of monolayers that extends over several cell diameters (*Figure 31*). Given that the planar stiffness of MDCK monolayers is 10 times larger than the transversal stiffness of MDCK cells (28, 41) and ~2 orders of magnitude larger than the elasticity of collagen gels, we expect restoring forces resulting from the planar deformations of monolayers to dominate. Furthermore, I have shown that my apparent rigidity measurements are sensitive to the presence of intercellular junctions (*Figure 31*). Thus, whilst I have demonstrated experimentally that deep AFM indentation of monolayers growing on soft collagen gels can probe the temporal evolution of monolayer mechanics, I leave the delineation of the relative mechanical contributions of each factor to future theoretical and experimental studies.

To evaluate the sensitivity of my experimental approach to the presence of intercellular junctions interfacing cells into a monolayer, I compared the apparent rigidity of control monolayers with that of the collagen gel alone, and with

monolayers in which intercellular adhesion had been disrupted through calcium chelation. Control monolayers grown on gels had a larger apparent rigidity than the collagen substrate alone ($E_{control}=181\pm33Pa$, $E_{gel}=66\pm8Pa$, $p^{**}<0.01$) while monolayers disaggregated by EDTA had a rigidity closer to, but larger than that of the gel ($E_{EDTA}=94\pm21Pa$, $p^*<0.01$ when compared to control monolayers (*Figure 31*) indicating that my measurements were indeed sensitive to the presence of intercellular junctions and suggesting that these give rise to supracellular mechanical properties. To further test this hypothesis, I examined the temporal evolution of apparent rigidity during the formation of intercellular junctions. Thirty minutes after replating cells onto a collagen gel, I sampled apparent rigidity at 2 min intervals. All curves examined shared the same characteristics (N=3 curves, black line, *Figure 31*): i) apparent rigidity increased steadily and quasi-linearly for ~120min before reaching a maximum 150min after replating, ii) apparent rigidity then decreased slowly over the next 150min. Qualitatively and quantitatively similar results were also obtained when measuring monolayer apparent rigidity at chosen time-points after replating: 60 minutes after replating, monolayer apparent rigidity was approximately 2-fold larger than the rigidity of collagen gels alone ($E_{60mins}=237\pm65Pa$, $E_{gel}=66\pm8Pa$, $p<0.01$), a maximum in rigidity was reached at 150 mins ($E_{150mins}=269\pm50Pa$), and rigidity then decreased significantly after 300 mins ($E_{150mins}=269\pm50Pa$, $E_{300mins}=196\pm49Pa$, $p<0.01$). The steep increase in apparent rigidity observed over the first 150min correlated with complete reformation of intercellular junctions while the slow decrease observed afterwards accompanied compaction of the cells (*Figure 31*). In contrast, collagen gels alone examined in identical conditions did not display any changes in mechanical properties (*Figure 31*, grey line). Together, these results show that apparent rigidity is sensitive to changes in monolayer supracellular mechanical properties and that intercellular junctions play a fundamental role in integrating individual cells into a tissue-scale mechanical syncitium.

THE EMERGENCE OF MONOLAYER SUPRACELLULAR RIGIDITY REQUIRES THE FORMATION OF ADHERENS JUNCTIONS BUT NOT DESMOSOMES

I sought to link the observed temporal change in apparent rigidity with the formation of adherens junctions and desmosomes. Live cell imaging revealed that the two main

components of adherens junctions, E-cadherin and F-actin, localised to cell-cell contacts forming well-defined intercellular adhesions within 150 minutes (***Figure 32*** A,B) concomitant with increase in monolayer apparent rigidity (***Figure 31*** G). Disrupting E-cadherin mediated adhesion with a blocking antibody or depolymerising actin filaments with latrunculin B prevented the formation of intercellular junctions (***Figure 32*** A,B) and the accompanying increases in apparent rigidity (***Figure 32*** C). In contrast, a well-defined intercellular intermediate filament network did not reform within this 150min time frame (***Figure 32*** D), consistent with the reported slow maturation of desmosomes at cell junctions (152). This suggested that intermediate filaments did not significantly contribute to the apparent rigidity measured by deep AFM indentation, perhaps because this technique induces strains (<15%, ***Figure 31*** E) that are small compared to the ~60% strain needed to tense keratin intermediate filament networks in suspended monolayers (41). Hence, in deep indentation measurements, intermediate filaments are unlikely to be taut between cell junctions and bearing mechanical stress. These data suggested that the increase in apparent rigidity observed in my measurements was due to the formation of adherens junctions but not desmosomes.

PERTURBATIONS TO ALL STAGES OF ADHERENS JUNCTION FORMATION ABOLISH INCREASES IN APPARENT RIGIDITY ACCOMPANYING INTERCELLULAR JUNCTION FORMATION

I then investigated how perturbation of the biological mechanisms leading to adherens junction formation affected the emergence of tissue-scale mechanical properties. Actin plays two major roles in adherens junction formation: first, polymerisation into a dendritic network via the arp2/3 complex enables lamellipodial crawling (153) and, second, this network is reorganised into a contractile actin belt via myosin contractility (53), α-catenin mediated inhibition of arp2/3 (62), and formin-mediated polymerisation (60, 61). (***Figure 33*** D) suggesting that the junctional F-actin network generated by the arp2/3 complex (154, 155) does not play a strong mechanical role.
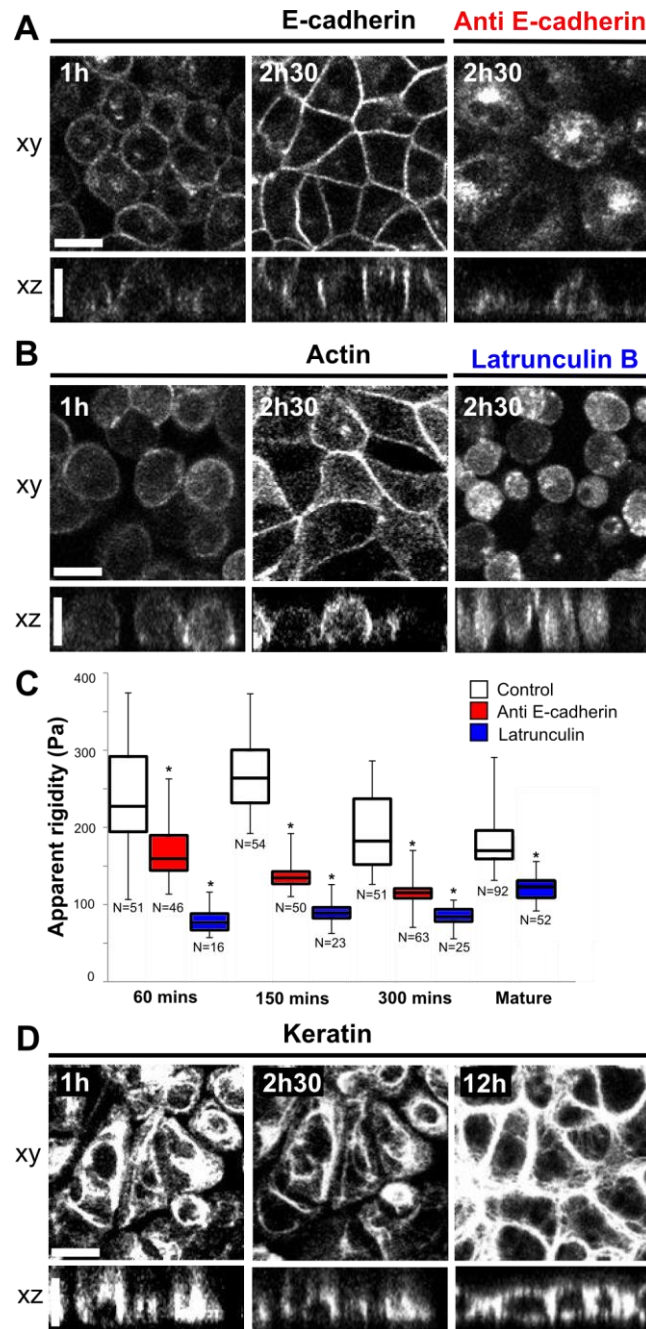
Figure 32 : Adherens junctions and desmosomes in monolayer mechanical properties

(A,B,D) All images are single confocal planes. The zx profile for each xy image is shown directly below it (s.b.=10 μm). Localisation of E-cadherin-GFP (A) and Life-act-Ruby (B, an F-actin reporter) localisation in cells 1h and 2h30 after replating onto collagen gels. E-cadherin and F-actin localisation to intercellular junctions can be inhibited by addition of anti E-cadherin blocking antibodies (A) or latrunculin B (B, a drug leading to F-actin depolymerisation) to the medium. (C) Apparent monolayer rigidity at 4 different time-points for control monolayers (white), monolayers treated with anti-E-Cadherin antibody (red), or latrunculin B (blue) (p*<0.01). The emergence of monolayer tissue-scale mechanical properties depended strongly on the assembly of a junctional F-actin network and the formation of E-cadherin mediated intercellular adhesions. (D) Localisation of keratin intermediate filaments visualised using keratin-18 GFP at different time-points after replating. An interconnected intercellular keratin network is not reformed between cells within 2h30.

When I blocked lamellipodial crawling with the arp2/3 inhibitor CK666 (125), poorly interconnected monolayers formed as cells were unable to establish initial contacts (*Figure 33* A), and the establishment of tissue-scale mechanical properties was severely impeded (*Figure 33* D). Surprisingly, in mature monolayers, arp2/3 inhibition did not affect apparent rigidity

Linear F-actin arrays generated by formins are also present at intercellular junctions (60, 61) and I investigated their contribution to monolayer apparent rigidity. Upon inhibition of formin activity with the broad spectrum inhibitor SMIFH2 (126), intercellular junctions appeared to form normally and some actin remodelling occurred (*Figure 33* B) but apparent rigidity was significantly lower than in control conditions at all time points (*Figure 33* B,D). These results confirm that formin mediated polymerisation of actin is required in the later steps of adherens junction maturation and indicate that linear actin arrays generated by formins play a significant role in monolayer supracellular rigidity.

INTERCELLULAR TENSION GENERATED BY MYOSIN CONTRACTILITY IS A MAJOR CONTRIBUTOR TO APPARENT RIGIDITY

Concomitant with the generation of linear arrays of F-actin by formins, junctional F-actin is also remodelled by myosin activity downstream of rho-kinase (53). Myosin contractility plays a fundamental role in cell and tissue mechanics generating cortical tension in single cells (34, 156), intercellular tension (59, 76, 102) as well as tissue-level tension (41) and deformations (18). Hence, I examined the role of myosin contractility on the establishment of monolayer tissue-scale mechanical properties. Inhibition of myosin II with blebbistatin abolished the increases in monolayer apparent rigidity that accompanied intercellular junction formation (*Figure 33* E) and reduced the apparent rigidity of mature monolayers to that of the collagen gel (Fig. 3E). Upon inhibition of Rho kinase by Y-27632, I observed a reduction in active F-actin remodelling at adherens junctions (*Figure 33* C), junctions appeared less taut between cells (*Figure 33* C), and the increase in monolayer apparent rigidity upon junction formation was severely impeded (*Figure 33* E). Previous work has shown that myosin II isoforms play complementary roles in cell monolayers and are regulated by different signalling pathways (157) with myosin

IIA controlled by ROCK and MLCK, while myosin IIB depends on Rap1. The identical effect of myosin II inhibition and ROCK inhibition therefore suggests that myosin IIA plays a dominant role in setting monolayer supracellular rigidity. Together, these results suggest that myosin-mediated tension rather than cellular elasticity is the prime determinant of monolayer tissue-scale mechanical properties.

In my measurements, increased apparent rigidity could either be due to an increase in Young's modulus of the cell monolayer concomitant with intercellular junction formation or to the establishment of a tissue-scale tension. The former hypothesis is supported by the role of actin nucleators in governing monolayer apparent rigidity and the notion that the actin cytoskeleton is the main determinant of cellular elasticity (28) (*Figure 33* D), while the latter is supported by the effect of inhibitors of myosin contractility (*Figure 33* E). One way of determining which of the two hypotheses is correct is to examine the width of the indentation profile generated by indentation to a chosen depth. If the change in apparent rigidity is due to an increase in elasticity, then the indentation profile should not change, instead the force necessary to create the indentation does. Conversely, if changes in apparent rigidity are due to the generation of a surface tension by the monolayer, the width of the indentation profile should increase significantly (148, 149). To test this experimentally, I acquired images of the indentation profile of monolayers expressing fluorescently-tagged membrane markers in response to a 15 μm deep indentation before and after disruption of intercellular junctions by calcium chelation with EDTA. In control monolayers, the indentation profile had a width larger than 150 μm (black curve, *Figure 34* A, top *Figure 34* B), whereas EDTA treatment reduced this width to ~90 μm (grey curve, *Figure 34* A, bottom *Figure 34* B). Hence, I concluded that formation of intercellular junctions leads to the establishment of a tissue-scale tension rather than an increase in monolayer elasticity, consistent with recent traction force-microscopy experiments (102).
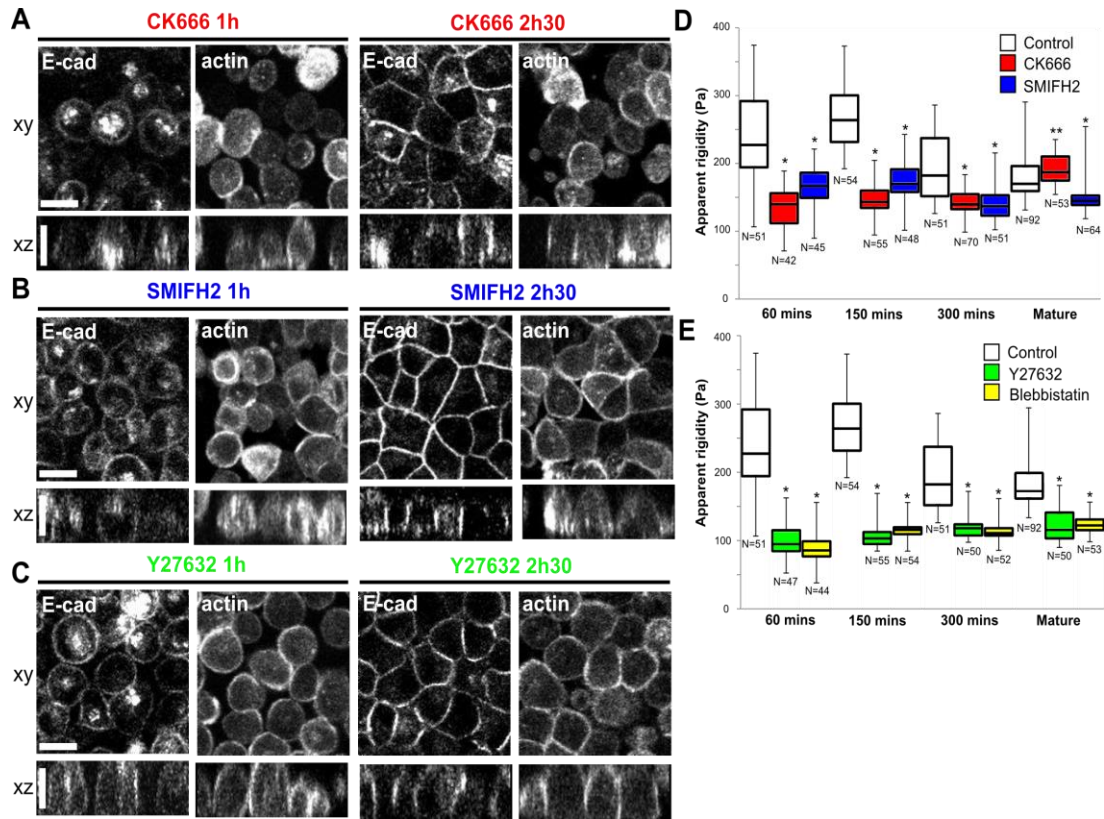
Figure 33 : Inhibition of the molecular mechanisms leading to adherens junction formation impedes the emergence of monolayer tissue-scale mechanical properties

(A-C) All images are single confocal planes. The zx profile for each xy image is shown directly below it (s.b.=10 μm). (A) Localisation of E-Cadherin and Life-Act-Ruby in cells treated with the arp2/3 inhibitor CK666 at 1h and 2h30 after replating. Treatment with CK666 prevents cell crawling and the formation of monolayers with extensive adherens junctions (red). (B) Localisation of E-Cadherin and Life-Act-Ruby in cells treated with the broad spectrum formin inhibitor SMIFH2 at 1h and 2h30 after replating. Treatment with SMIFH2 significantly delays actin polymerisation and decreases monolayer apparent rigidity reached at each time-point (blue). (C) Localisation of E-Cadherin and Life-Act-Ruby in cells treated with the rho-kinase inhibitor Y27632 at 1h and 2h30 after replating. Treatment with Y27632 inhibits rho kinase prevents the formation of contractile actin bundles at adherens junctions and leading to reduced monolayer stiffening (green). (D, E) Monolayer apparent rigidity at different time-points in control monolayers and monolayers treated with inhibitors of F-actin polymerisation (D) and (E) myosin contractility (blebbistatin in yellow), (p*<0.01, p**=0.03).

APPARENT RIGIDITY DECREASES ON LONG TIMESCALES WITH THE OPTIMISATION OF CELL PACKING

In my time-resolved measurements, I observed that monolayer apparent rigidity increased over the first ~150 minutes after replating before decreasing in the following 150 minutes ($E_{150mins}=269\pm50Pa$, $E_{300mins}=196\pm49Pa$, $p<0.01$). Furthermore, monolayers that were left to grow overnight showed a trend towards further reductions in apparent rigidity ($E_{300mins}=196\pm49Pa$, $E_{mature}=181\pm33Pa$,

p=0.06). I have established that the initial increase in monolayer apparent rigidity results from the formation of adherens junctions. In this process, cells spread to establish initial contacts and recruit actin and myosin to intercellular junctions increasing monolayer tension and hence apparent rigidity (*Figure 34*). Following this initial step, the height of intercellular junctions increases as they mature, cell morphology changes from spread to cuboidal, and cells condense (*Figure 31*). When I measured the average cell projected area over time, I found that its evolution mirrored the evolution of apparent rigidity (grey line, *Figure 34* D): projected area first increased significantly between 60 and 150 mins before decreasing significantly at 300 mins and overnight (black line, *Figure 34* D). I envisaged two different possible causes for the decrease in cellular projected area after 150min. First, following formation of intercellular junctions, cells may seek to minimise the intercellular stresses they are exposed to by moving with respect to one another within the monolayer (103). Second, cell division may decrease tissue tension by increasing cell density (79). Examination of time-lapse movies of monolayer formation revealed that cell divisions were rare during the first 300 mins following replating. However, over the same time period, cell density increased significantly (*Figure 34* B) and cell movements relative to one another could be observed, suggesting that cell rearrangement within the monolayer played a significant role in increasing cell density and decreasing cell projected area. After overnight maturation, cell density increased significantly (p<0.01 compared to 300 mins) though elasticity only showed a trend towards decreasing, suggesting that cell division may play a role in tension homeostasis but that cell rearrangements dominate over the time-frame of my experiments. Together, these data reinforce the notion that tension is at homeostasis in tissues and that this can be reached through changing cell packing density by rearrangement, apoptosis, or mitosis (87, 91, 92, 96).
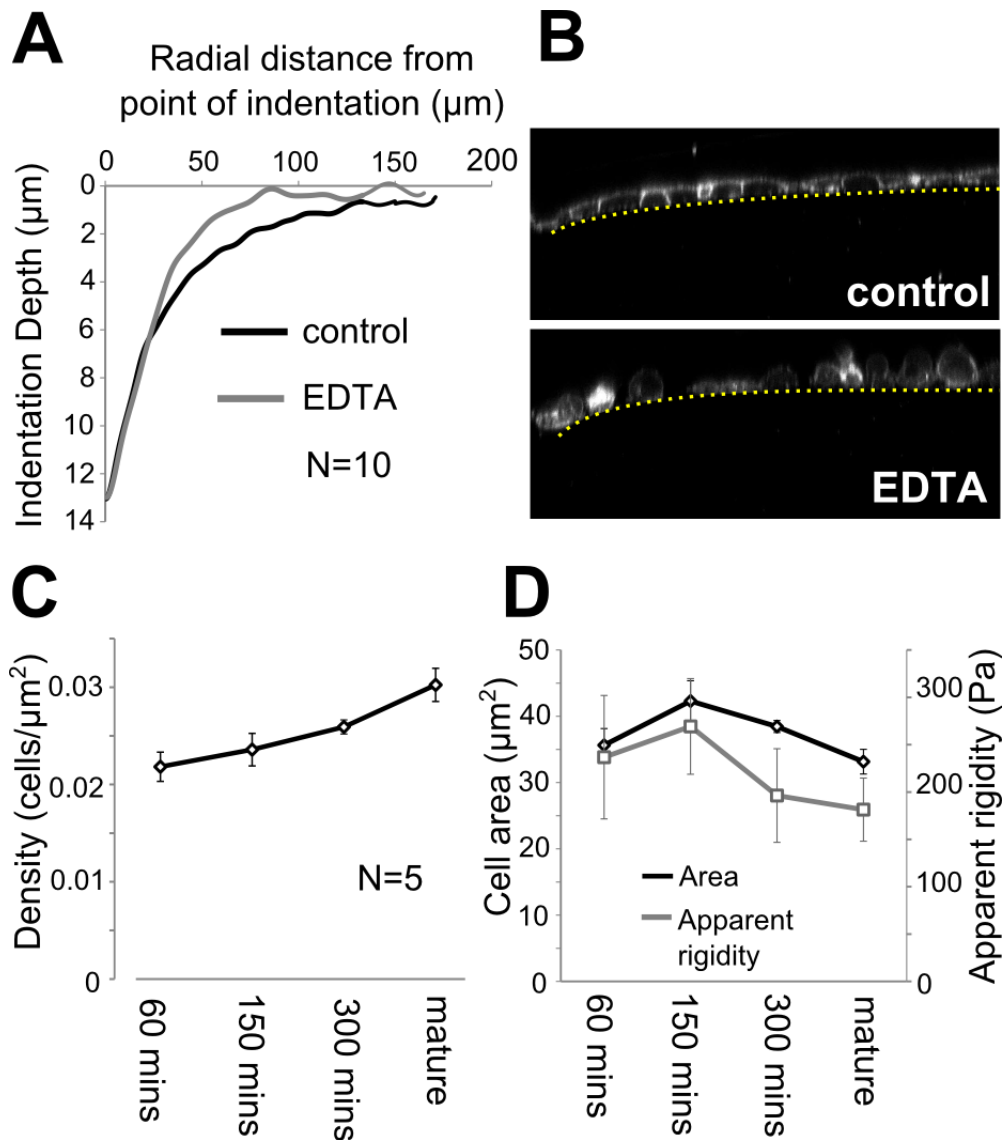
Figure 34 : Monolayer apparent rigidity results from a tissue-scale monolayer tension and cell rearrangements within the monolayer alter monolayer tension

(A) Monolayer indentation profile as a function of distance to the centre of indentation. Disrupting intercellular adhesion with EDTA (grey line) reduced the spatial extent of the indentation profile compared to control monolayers (black line). Curves are averaged over 10 experiments. (B) Images of a control monolayer (top) and EDTA treated monolayer (bottom) with the indentation profiles highlighted in yellow. (C) Temporal evolution of cell density averaged over 5 monolayers. Data points are represented as mean±SD. (D) Temporal evolution of projected cell area (black line) and apparent rigidity (grey line) over the course of intercellular junction formation and maturation. Data points are represented as mean±SD and are averaged over N=5 experiments.

v. DISCUSSION

Using time-lapse imaging and time-resolved mechanical measurements together with chemical perturbations, I have shown that the formation of intercellular junctions is accompanied by an increase in monolayer apparent rigidity that reflects the

emergence of tissue-scale mechanical properties. This phenomenon was critically dependent on the sequence of molecular steps leading to the formation of mature adherens junctions and coincided with it temporally (*Figure 35*). In contrast, during the 150 minute time-course over which increases in apparent rigidity were observed, an intercellular network of intermediate filaments linked by desmosomes did not reform and its presence in mature monolayers did not correlate with increased apparent rigidity. Perturbation of each of the steps leading to the assembly of mature contractile adherens junctions significantly affected monolayer mechanical properties. Disruption of lamellipodial extension through arp2/3 inhibition prevented stiffening, consistent with its role in the initial formation of intercellular contacts and their subsequent broadening. However, in mature monolayers, inhibition of arp2/3 did not affect apparent rigidity, in contrast to recent laser ablation experiments suggesting a role for arp2/3 in junctional tension (155), something perhaps due to incomplete maturation of adherens junctions in gene depletion experiments. Perturbation of formin mediated actin polymerisation decreased monolayer apparent rigidity in forming and mature monolayers, consistent with the notion that formins generate contractile F-actin arrays (158).

My data show that the main contribution to monolayer apparent rigidity was tension due to actomyosin contractility. Indeed, examination of the monolayer indentation profile before and after disruption of intercellular adhesions revealed that apparent rigidity was primarily dominated by tension within the monolayer. Recent traction force microscopy experiments have shown that total traction force increases linearly with the number of cells in colonies (92), suggesting that the linear increase in apparent rigidity I observed over the first 150 min after replating reflects a progressive increase in the number of cells interfaced to one another around the location of the indentation. Chemical perturbation experiments further confirmed the role of tension in the increase in monolayer apparent rigidity concomitant with intercellular junction formation. Indeed, depolymerisation of the actin cytoskeleton by latrunculin treatment or inhibition of myosin contractility both resulted in a near total loss of stiffening associated with monolayer formation. My results are consistent with recent work showing that intrinsic actomyosin activity constitutively exerts tension on E-cadherin at intercellular junctions (76, 102).
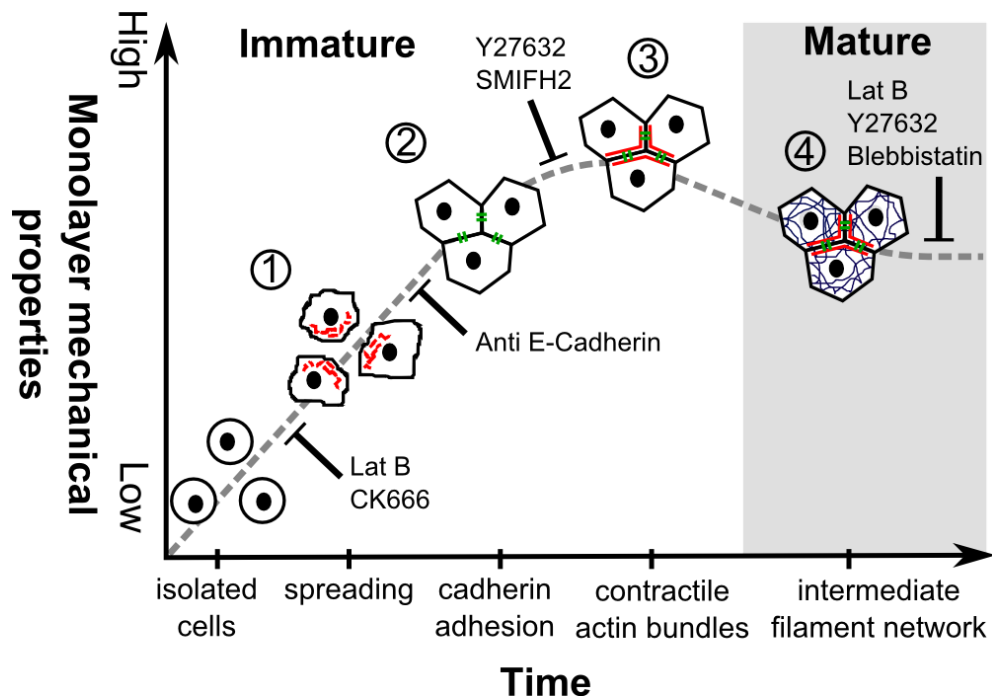
Figure 35 : Perspective view: The emergence of monolayer tissue-scale mechanical properties coincides with intercellular junction formation

After plating, spreading cells form lamellipodia resulting from the formation of a dendritic network of F-actin downstream of arp2/3 (red, 1). Upon contact of lamellipodia from neighbouring cells, E-cadherin clusters interface the membranes of contacting cells (green, 2). The dendritic F-actin network is then remodelled at the cell junctions through de novo filament polymerisation by formins and myosin-mediated remodelling (3). Later, an intercellular keratin filament network linked by desmosomes is established (blue, 4). Monolayer apparent rigidity increases concurrently with this sequence of events and inhibition of each of these molecular mechanisms perturbs the emergence of monolayer tissue-scale mechanical properties. Actomyosin contractility creates a tissue tension that is the major determinant of monolayer apparent rigidity.

In time-resolved AFM measurements, monolayer apparent rigidity initially increased over the course of two hours, reaching a peak before decreasing significantly between 2.5-5 hours after replating. Examination of temporal evolution of projected cell area and cell density suggested that decreases in apparent rigidity may be due to cell rearrangement within the monolayer to reach an energetically optimal configuration. Indeed, recent studies show that regulatory mechanisms involved in maintaining tissue tensional homeostasis can cause cells to apoptose (87) or migrate within the monolayer to minimise intercellular shear stresses (103). My data suggest that two temporally distinct steps may be necessary to reach optimal monolayer configuration from dissociated cells: first, cells adopt a high tension state to rapidly reform intercellular junctions, then, following confluence, cells optimise their arrangement within the monolayer to return to tissue tensional homeostasis. In

summary, I have shown that the establishment of mature contractile adherens junctions is accompanied by the emergence of tissue-scale mechanical properties and my technique paves the way to understand the molecular mechanisms underlying the integration of stresses generated by individual cells into a tissue-level tension.

vi. SUMMARY

Here I have shown the importance of the establishment and maturation of intercellular junctions in setting monolayer mechanical properties. The main drawback of this method is the interpretation of the mechanical measurements. The ability to dissect the contribution of pre-stress, elasticity and the effect of having a composite material would be greatly beneficial. However, I did not pursue this in my doctoral work as I had developed another tool to probe the mechanical properties of monolayers in the monolayer plane, free from their substrate. The advantage of this approach is the simple interpretation of the stress-strain response to evaluate monolayer elasticity.

7. CHARACTERISING THE PLANAR MECHANICS OF CULTURED CELL MONOLAYERS

i. ACKNOWLEDGEMENTS

ii. INTRODUCTION

To date, research in cell mechanics has primarily focused on isolated cells and much is now known about their mechanical properties in both normal physiology and disease (15). Comparatively little is known about the mechanics of simple tissues such as monolayers but recently experiments combining traction force microscopy with deformation analysis have begun to shed light on this topic. Within monolayers, stresses are propagated over several cell diameters by intercellular adhesion, cells migrate to minimise intercellular shear stress (103) and the collective motion of cells within monolayers displays behaviours reminiscent of a glass transition (71, 96). Despite these advances, our knowledge of monolayer mechanical properties such as stiffness or ultimate strength remains poor due to lack of an appropriate experimental technique. Extrapolation of these parameters from single cell measurements is not possible due to radical differences in cytoskeletal organisation associated with the formation of intercellular junctions. Present measurements of intercellular adhesion energy are restricted to durations over which intercellular junctions cannot fully mature (on the order of minutes) (58, 94). Direct experimental measurements on monolayers with mature intercellular junctions would greatly enhance our understanding of the mechanics of epithelial morphogenesis (80, 159) and the effect of pathologies on tissue strength (51).

To fill this gap I developed a versatile new system that allows investigation of the tensile planar mechanical properties of epithelial cell monolayers in isolation from their substrate. I interfaced the technique with high resolution confocal imaging of

subcellular structures and proteins that constitute cell junctions and the cytoskeleton. In addition, I designed this system such that forces can be measured as the monolayer is stretched, to extract the elasticity and intercellular adhesion strength of monolayers. Through the spatial organisation of their cytoskeleton and interfacing via specialised intercellular adhesions, cells create a tissue that has a much higher elastic modulus than measured in single cells (28, 29, 41).

iii. DEVELOPMENT OF A DEVICE TO MEASURE PLANAR MONOLAYER MECHANICS

The general principle of the system to characterise monolayer mechanics is simple: monolayers suspended between the extremities of two test rods are slowly extended by prising the rods apart with a micromanipulator. The applied force can be measured by monitoring the bending of the soft test rod during monolayer extension. My mechanical characterisation setup addresses four key requirements: (i) monolayers must be free from their substrate such that only the monolayer is load-bearing to allow for simple interpretation of the stress-strain response, (ii) attachment of the samples to the test rods must require minimal manipulation, (iii) live microscopy imaging at the cellular and subcellular level must be possible during mechanical stimulus, (iv) measurements must be quantitative to enable comparison between treatments.

Below I describe the necessity of, and solution to, each of these design requirements in further detail. The details of the device design and measurement protocols are contained within the materials and methods section (*Chapter 7 section V*).

(I) MONOLAYERS MUST BE FREE FROM THEIR SUBSTRATE

Tensile testing of materials is a traditional method for establishing their mechanical properties such as elasticity and ultimate strength due to the simplicity of measurement and interpretation. Although this works well for materials such as metals and polymers, biological samples have additional requirements that need to be addressed by the experimental technique. For example, these experiments need to be carried out in a fluid environment to keep the cells alive. Indeed, combining the practicalities of both cell culture and mechanical testing presents a particular challenge.

A common method to stretch cells is to culture them onto elastic substrates and mechanically activate the cells through substrate stretching. The difficulty with this approach is that decoupling the mechanical response of the cells from the substrate is non-trivial. Measuring mechanical properties such as ultimate strength are not possible with this approach as the durability of the cell-substrate composite is dominated by the elastic substrate.

To generate cell monolayers free from a substrate with minimal manipulation, cells were cultured on a temporary sacrificial substrate created by polymerising a drop of collagen between the two rods. Cells were seeded onto this scaffold and cultured until the monolayer extended from one test rod to the other covering the whole collagen substrate and part of each test rod (*Figure 36*). Prior to mechanical testing, the collagen was removed by enzymatic digestion leaving the monolayer attached to the test rods by cell-substrate adhesion but devoid of substrate and freely suspended in between (*Figure 36*).

(II) ATTACHMENT OF THE SAMPLES TO THE TEST RODS MUST REQUIRE MINIMAL MANIPULATION

Culturing the cells onto the test rods and then removing the substrate by enzymatic digestion is a physically non-invasive way of removing the substrate. Previous approaches require the use of tissue adhesives to attach samples to testing apparatus (89). The disadvantage of physically manipulating samples and using adhesives is that biological samples are fragile and can become damaged during attachment. The digestion approach requires no user manipulation of the sample or glue to affix it. By preparing the sample between two test rods, the monolayer is readily available to stimulate mechanically simply by prising the test rods apart.
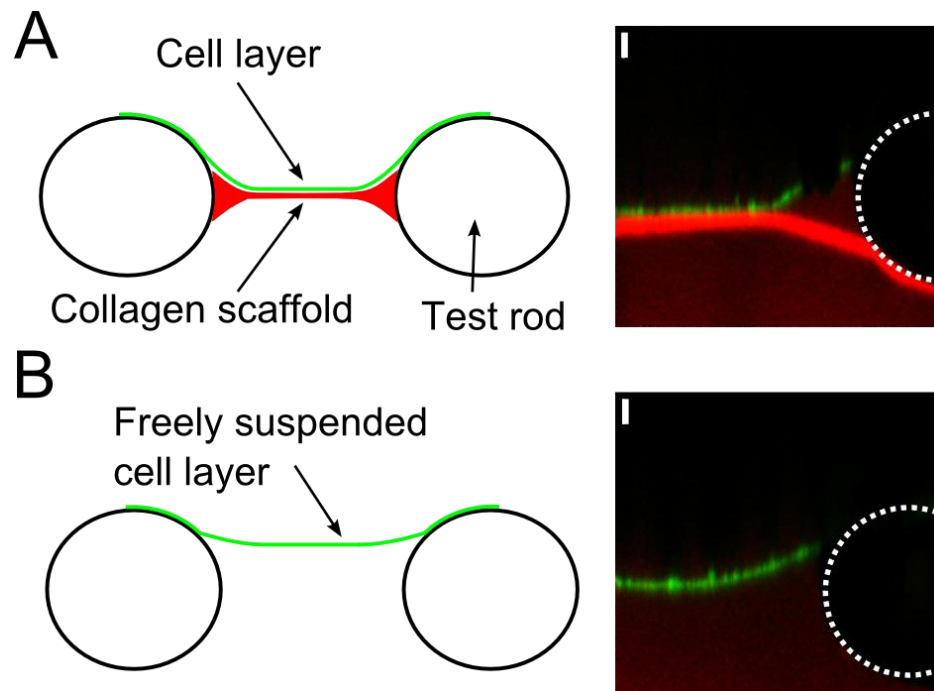
Figure 36 : Experimental setup for measuring the mechanical properties of cell monolayers.

(A) Left: line drawing, right: microscopy image. Cell layers (green) were cultured on a sacrificial collagen scaffold gelled between the test rods (red in line drawing and immunostain, s.b = 100 μm). (B) After enzymatic digestion, the collagen layer was completely removed leaving the monolayer freely suspended between the two test rods as evidenced by the loss of collagen immunostaining (red).

(III) LIVE MICROSCOPY IMAGING AT THE CELLULAR AND SUB-CELLULAR LEVEL MUST BE POSSIBLE DURING MECHANICAL STIMULUS

In order to address this design requirement I developed a mechanical testing setup that could be interfaced onto the standard stage of an inverted optical microscope. The mechanical testing equipment (*Figure 37*) consisted of two micromanipulators and a top-down macroscope to image test rod positions. A manual micromanipulator kept one rod stationary, while a motorised micromanipulator controls the displacement of the other.

The simplest form of the test rod design is where both rods are rigid. The devices consisted of a U shaped capillary, the arms of the U shape being the test rods and the bend acting as a point for attachment to the culture dish. A hinge was introduced into one of the arms by making a small break at the capillary base and threading it with a flexible wire making it easy to manipulate. Prising the rods apart at the top strains the monolayer directly, making these devices convenient for high magnification

imaging. Monolayers can be imaged at high resolution using conventional top down microscopes with dipping objectives that have a long working distance and high numerical aperture. Imaging devices at high magnification with inverted microscopes poses more of a challenge due to the comparatively shorter working distance of the objectives and the additional complication of the presence of the coverslip. To solve this problem, devices could be prepared in the first instance without attaching them permanently to the bottom of the culture dish. Then devices could be flipped over before imaging bringing monolayers closer to the bottom of the coverslip and within the working distance of the high magnification objectives.
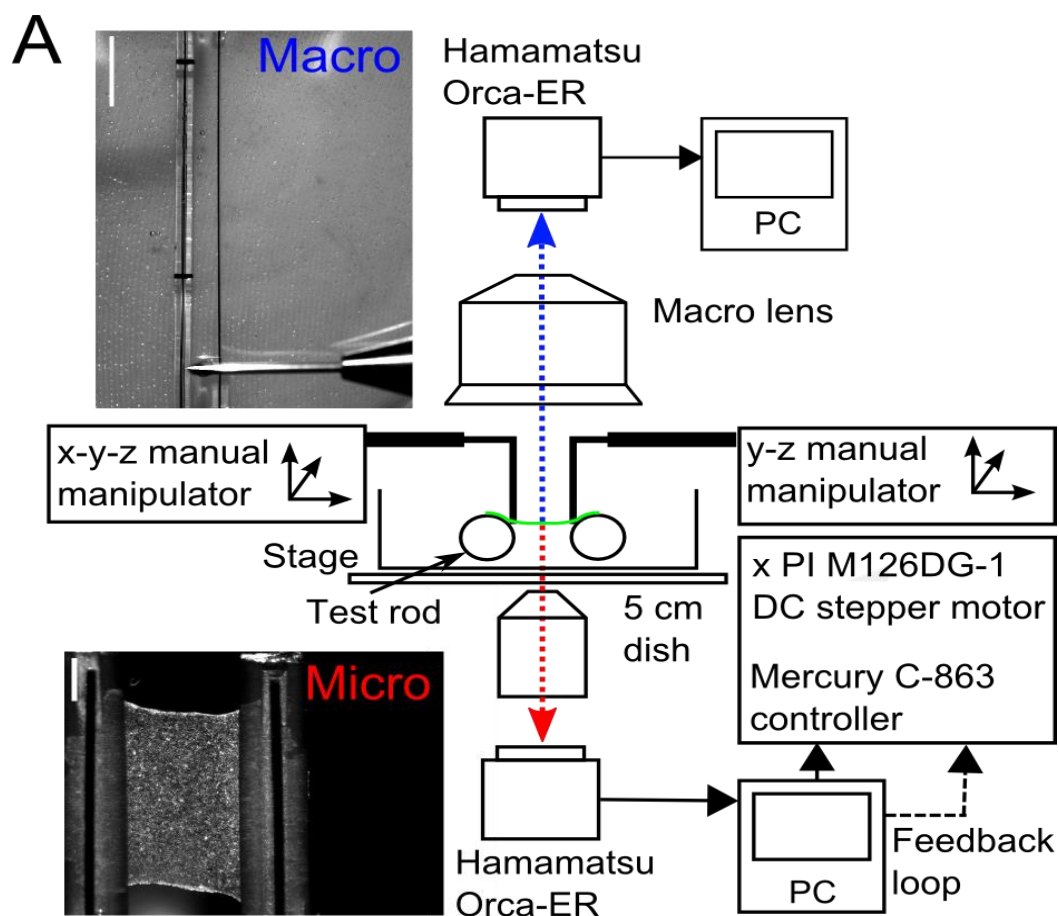
Figure 37 : Schematic diagram of the mechanical testing setup

(A) Petri dishes containing monolayer culture devices were mounted onto the microscope stage. The motorised micromanipulator (Physik Instrumente M126.DG1) arm was brought into contact with the soft test rod and the manual micromanipulator (Physik Instrumente M105.30) arm with the reference rod. The device test rods could be prised apart, thereby extending the cell monolayer, using the motorised manipulator for accurate control over extension and strain rate. Monolayer extension was imaged with an inverted microscope (red light path giving the bottom left image) and the positions of the test rods were monitored with a top-down macroscope (Canon FD macrolens) (blue light path giving the top left image) allowing measurement of strain and stress. In some experiments, a feedback loop was implemented to achieve constant stress or constant strain at 10Hz.

(IV) MEASUREMENTS MUST BE QUANTITATIVE TO ENABLE COMPARISON BETWEEN TREATMENTS.

This initial device design did not enable measurement of the force required to extend the monolayer. To generate quantitative measurements of monolayer mechanical properties, I developed the test rods system to allow for force measurements. Devices consisted of three main components (*Figure 38*): (i) a U-shaped glass capillary with one long arm that acts as a rigid reference rod, and a short arm that connects to the flexible test rod, (ii) a flexible test rod made of NiTi metal wire with a small enough bending rigidity for sub milli-Newton forces to induce a deflection precisely measurable by the macroscope, (iii) a small rigid reference sleeve on the flexible test rod that can be used to determine its unstressed position. Forces applied onto the monolayer during extension were determined by measuring the deflection *d* of the wire relative to its predicted unstressed position (*Figure 39* A, B) and fitting *d(y)* with a simple cantilevered beam model (*Figure 39* C, D).
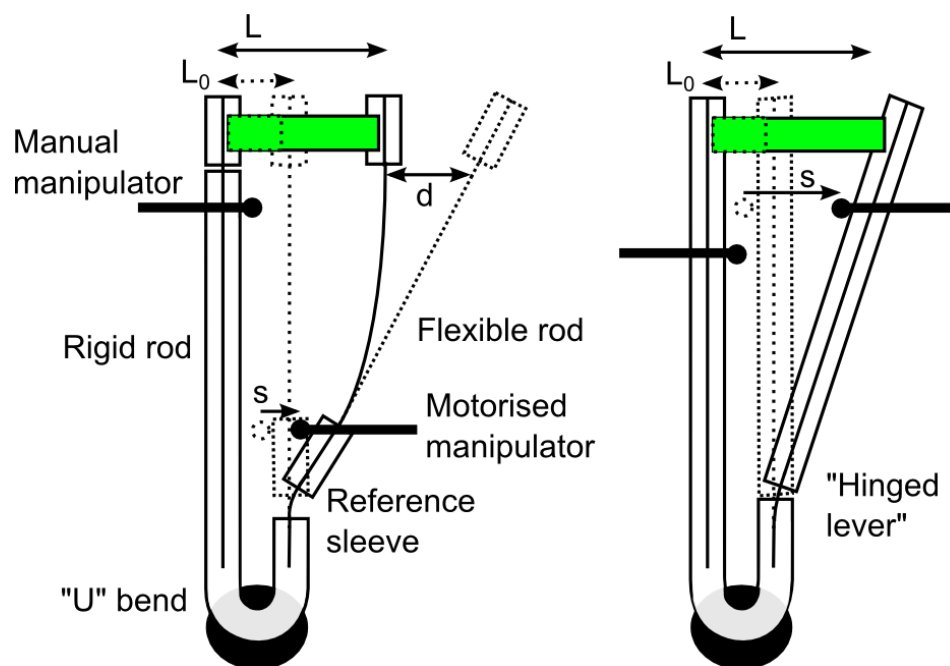
Figure 38 : Test rod device design

The device was enclosed inside a 5cm Petri dish. In the image, d is the flexible rod deflection, s the motor displacement and L the length of the monolayer, and the monolayer is shown in green (~2mm wide). These devices are ~4cm in length with the capillaries used being 1mm in diameter. The flexible wire is 100μm in diameter (see section V, Device fabrication). By making both of the test rods rigid, the strain on the monolayer could be directly controlled. These devices could be flipped over to bring the monolayer into the working range of higher magnification objectives on an inverted microscope. In devices for high magnification imaging thinner capillaries were used 0.8mm in diameter and thicker wire 200μm diameter (see section V, Device fabrication).
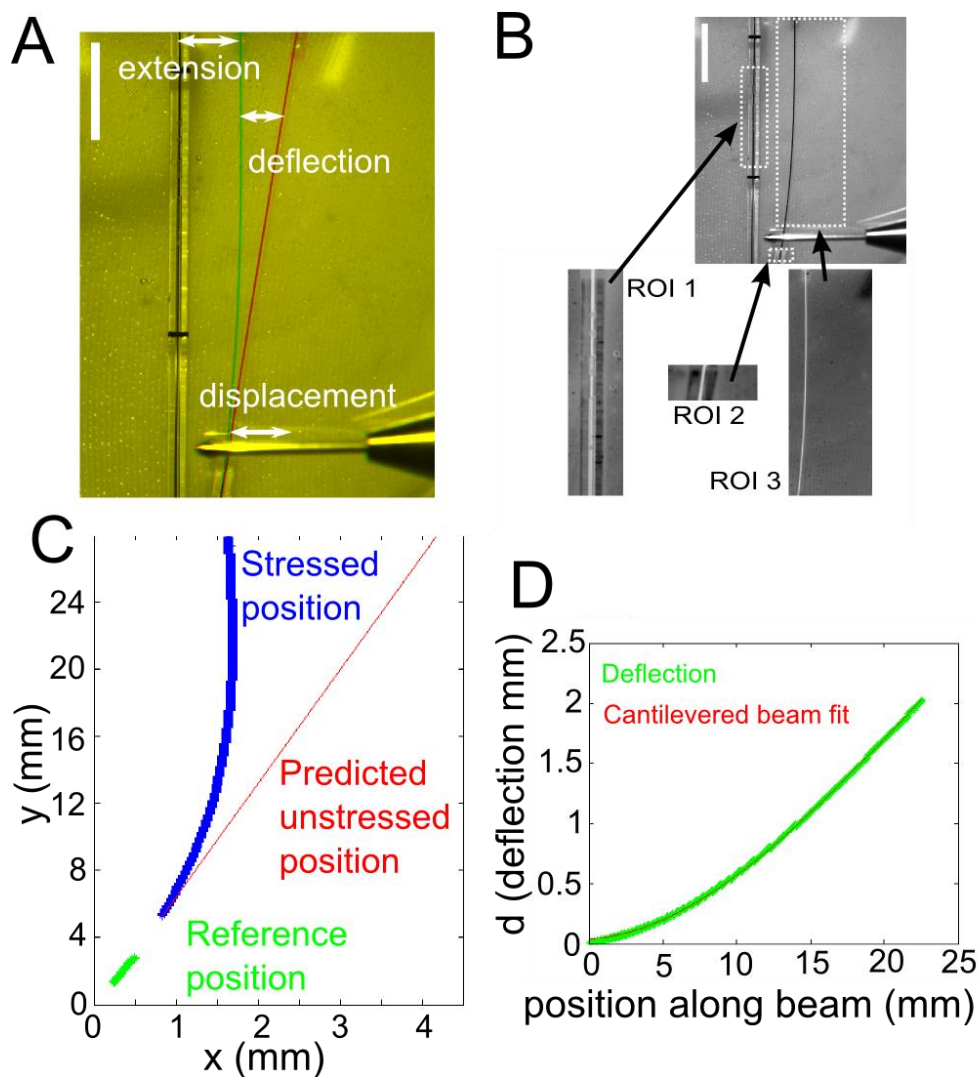
Figure 39 : Measurement of forces

(A) Colour combined image showing the macroscope view of a force measurement device with the flexible wire in the stressed (green, monolayer attached) and relaxed (red, ruptured monolayer) states (scale bar = 5mm). (B) Images from time lapse acquisitions were separated into three regions of interest (scale bar = 5mm) (ROI). By inverting the images, the position of the static (ROI 1), reference (ROI 2) and flexible (ROI 3) rods could be found by fitting a Gaussian intensity profile for each row of pixels successively. (C) The extracted position of the reference rod can be extrapolated to obtain the predicted unstressed position of the flexible rod (red). By subtracting the stressed position (blue) of the flexible rod from its predicted unstressed position (red), I obtained the deflection which can be fitted with a cantilevered beam model (D).

FORCE MEASUREMENTS ON MONOLAYERS

Force measurements were possible with this system by the correct calibration of the wire mechanical properties and accurate measurement of the rod deflection with image analysis. In order to measure the force exerted on the monolayer during

extension, macroscope images were acquired during extension at regular time intervals. The images were then analysed post hoc to obtain values for the stress and strain at each timepoint. Macroscope images were subjected to a Gaussian filter to smooth the image and reduce the influence of background noise and separated into three regions of interest to identify the static rod, the reference sleeve, and the flexible rod. The extremity of the reference glass sleeve was identified manually to measure the length of the flexible arm. The images were inverted and a Gaussian intensity profile fitted along the x direction for each row of pixels to identify the peak corresponding to the rod position. The static rod maxima were fitted with a line to identify the reference position, which was then used in calculating the strain on the monolayer.

To measure the deflection of the flexible test rod, the position of the peaks of the Gaussian fits were extracted and compared to the rod's predicted "unstressed" position. The unstressed position was computed from the projection of the portion of the flexible arm within the sleeve (i.e. that is unable to bend). This portion was fitted with a straight line which represents the predicted position of the flexible test rod with no restoring force from the cell sheet. The rod deflection *d(y)* was computed as the difference between the position of the unstressed bar and the actual measured position. The force was then calculated by fitting the whole rod deflection with the equation for a simple cantilevered beam(160):

$$F = \frac{-d(y)\,6\,E\,I}{(3L - y)y^2}$$

$$I = \frac{\pi r^4}{4}$$

Here, *I* is the area moment of inertia of the wire, *r* the wire radius, and *E* its elastic modulus. The engineering strain ε was measured by normalising the monolayer extension (measured length minus initial length) to the initial length.

$$\varepsilon = \frac{L - L_0}{L_0}$$

The stress σ was computed by dividing the measured force F by the cross sectional area of the monolayer, which was estimated from the measured monolayer width (measured from microscope images, t ~2mm) and the average monolayer thickness (d ~10μm).

$$\sigma = \frac{F}{t\,d}$$

WIRE CALIBRATION

For the calculation of the force the quantity E, the elastic modulus of the NiTi wire was calibrated. I devised a simple loading experiment where different loads of plasticine were attached to the end of a 4 cm long piece of wire and the deflection due to gravity measured. The mass of the NiTi wire was neglected and the system treated as a cantilevered beam loaded at its end. The deflection of several different wire samples were measured with 5 different weights, and the experiment repeated 5 times on different days. The deflection was measured using the macroscope camera setup. By measuring the length of the wire with Vernier callipers I calculated the elastic modulus of the wire to be 86.5±5.3 GPa, close to the manufacturer's estimate of 75 GPa.

SOURCES OF ERROR

Assuming that the wire is manufactured well with good quality control by the manufacturer there is not a high source of error with the associated wire elasticity and diameter. The elasticity of the wire was recalibrated with the loading measurements described above and was re-calibrated for new batches of wire. The wire diameter verified with digital vernier callipers. The main general source of error with this measurement is the detection of the wire positions with the macrosope and hence the calculation of the deflection and applied force. The deflection only scales linearly with the applied force but is limited in the fact that it is optically measured. To minimise error from this source, the wire intensity profile was fitted with a Gaussian to provide sub-pixel resolution on the position. The deflection was evaluated along the full length of the wire cantilever and then fitted with a cantilever beam model to minimise noise in the measurement. This method can accurately

measure sub milli-newton forces with a precision of ~5-10μN. This can be improved upon by implementing a digital force transducer (see **Chapter 9 Future work**).

iv. VALIDATION AND CALIBRATION OF THE METHOD

I verified the method with a series of control measurements. Firstly, I needed to confirm that the cells remained viable during the experiments, that they were alive, and retained their epithelial characteristics. Secondly, I needed to verify that the mechanical measurements were correct by calibrating with a classic material of known mechanical properties.

CELL VIABILITY

To verify that cell monolayers were healthy after removal of the substrate I conducted a live/dead assay (*Figure 40*). Propidium Iodide, a non-permeable nucleic acid marker only enters the cell and stains the nucleus on loss of membrane integrity, which is an early sign of cell death. To determine the location of nuclei within live monolayers, I treated them with Hoechst 34332, a membrane permeable nucleic acid marker to observe the position of the cell nuclei without membrane permeation. Over a duration of 3 hours, no fluorescent signal from the propidium iodide could be observed indicating that cell membranes were not compromised. As a control for the correct function of propidium iodide measurement the cell membrane was permeablised with a detergent Triton X at the end of the experiment. Upon permeablisiation of the cell membrane fluorescent signal could be seen from the propidium iodide which co-localised with the original Hoechst staining.
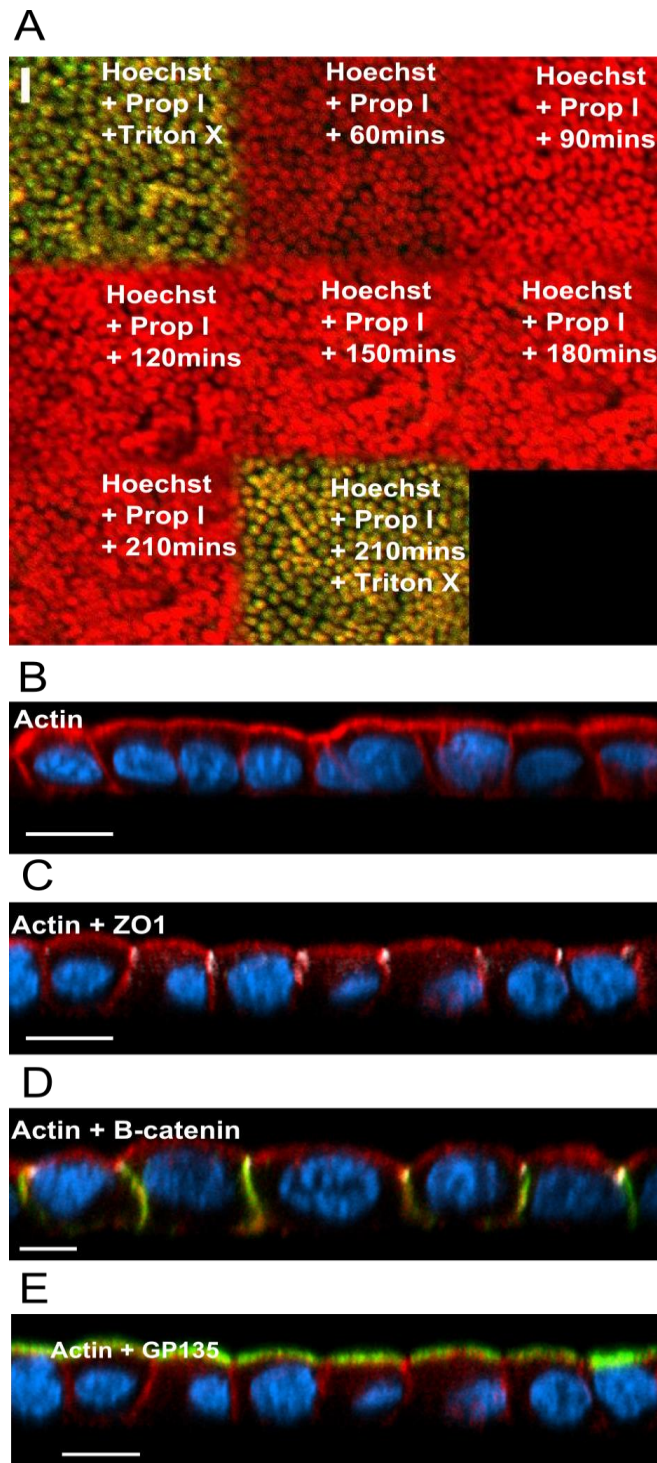
Figure 40 : Validation of cell viability through live-dead assay and immunostaining

(A) Cell viability within monolayers devoid of a substrate was checked using a live/dead assay. The nuclei of live cells were stained with the cell permeant nuclear stain Hoechst 33342 (1µg/ml for 5 min). To detect cells with compromised membranes, propidium iodide, a cell impermeant nuclear marker, was included in the medium at all times (1 µg/ml). Hoechst staining was imaged with a 405 nm laser (shown in red in the image) and propidium iodide (PI) was excited at 568nm (shown in green in the image). As a control for PI staining, I permeabilised the membrane of cells on a substrate (top left image). Upon permeabilisation with Triton-X100, cellular nuclei were intensely stained with propidium iodide and colocalised with Hoechst staining appearing yellow. Next, I imaged monolayers devoid of a substrate for at least 210 minutes in the presence of propidium iodide. During that time no propidium iodide staining was observed and Hoechst staining did not show any signs of nuclear condensation or fragmentation, indicating that the monolayers remained healthy. After 210 mins, to verify that propidium iodide was present in the medium and able to stain the nuclei, I permeablised the cells with the addition of tritonX to the medium. This resulted in rapid and intense propidium iodide staining of the monolayer (bottom centre image). Together, these images indicate that the cells within the monolayer are viable for much longer than the time course of my experiments (~10min). (B-E) To verify that monolayers retained their epithelial polarity after collagen digestion, freely suspended monolayers were fixed 3h after removal of the substrate and immunostained with antibodies against classical epithelial polarity markers. In each image, red shows the localisation of the actin cytoskeleton visualised with phalloidin-TRITC staining and blue shows the nucleus labelled with DAPi. (B) As in polarised monolayers cultured on substrates, F-actin was enriched at cell junctions and apically. (C) The tight junction protein ZO-1 (white) localised to distinct puncta at the apical side of cell-cell junctions. (D) β-catenin (green), a component of adherens junctions remained localised to cell junctions. (E) GP135 a marker of apical transport channels labelled the apical membrane of the cells. Together, these images demonstrate that the cells within the monolayer retain their characteristic epithelial polarisation for at least 3h after substrate removal.

115

Having confirmed cell viability, I checked that the apical-basal polarity of the cells was maintained for the duration of the experiments. Immunostaining of apical and junctional markers was performed to test the maintenance of cell polarity in collaboration with Julien Bellis. The cell nuclei were stained with DAPi in all experiments. F-actin was stained with phalloidin and localised to cell junctions and apically as expected for adherens junctions and micro-villus structures. Secondly, to verify the maintenance of mature and stable cell junctions monolayers were stained for ZO-1 and Beta-Catenin. ZO-1 is a protein involved in the formation of tight junctions that localises at cell junctions, near to the apical cell membrane. Beta-Catenin is a protein involved in the formation of adherens junctions and therefore localises at intercellular junctions. Finally, cells were stained for GP135, a marker of apical ion channels in the cell membrane, was strongly apical in the stained cells. These data show that, in the absence of substrate, monolayers stayed healthy and maintained their characteristic epithelial apico-basal polarisation for at least 3h (*Figure 40* B-E).

ELASTICITY CALIBRATION

To validate my experimental setup, I measured the elasticity of calibrated thin PDMS strips (*Figure 41* A). PDMS strips of different stiffnesses were created by mixing PDMS with different proportions of crosslinker or by varying baking time and temperature. Baking for shorter periods and lowering the concentration of crosslinker both result in softer strips. Briefly, PDMS was mixed thoroughly at the following ratio of primer to crosslinker 10:1 and 20:1, degassed and then spin-coated onto a silicon wafer. Wafers were then baked at 50 or 75 degrees for 4h or 90 min depending on the desired properties. Strips were generated by scraping the layer of PDMS with a scalpel. Their thickness was measured with confocal microscopy to be approximately d~50μm. Strips could be placed onto the extremities of devices ready for extension by reversible bonding of the PDMS to the test rods. Devices were custom made with a 0.3mm NiTi diameter wire due to the thicker and stiffer nature of the test material. To verify the measured elasticities with an independent method, the length of PDMS strips were measured under vertical load by adding defined masses to one extremity. One end of the PDMS strip was secured to the edge of a workbench and a small clip added to the other end. To increase the applied load,

additional clips were added. The length of each strip of PDMS at each load was measured using a pair of vernier callipers. The lengths were measured for five different loads and the elastic modulus calculated from the slope of the stress-strain response. Elasticities measured with this method were similar to those measured with the devices and values reported in the literature (161, 162).
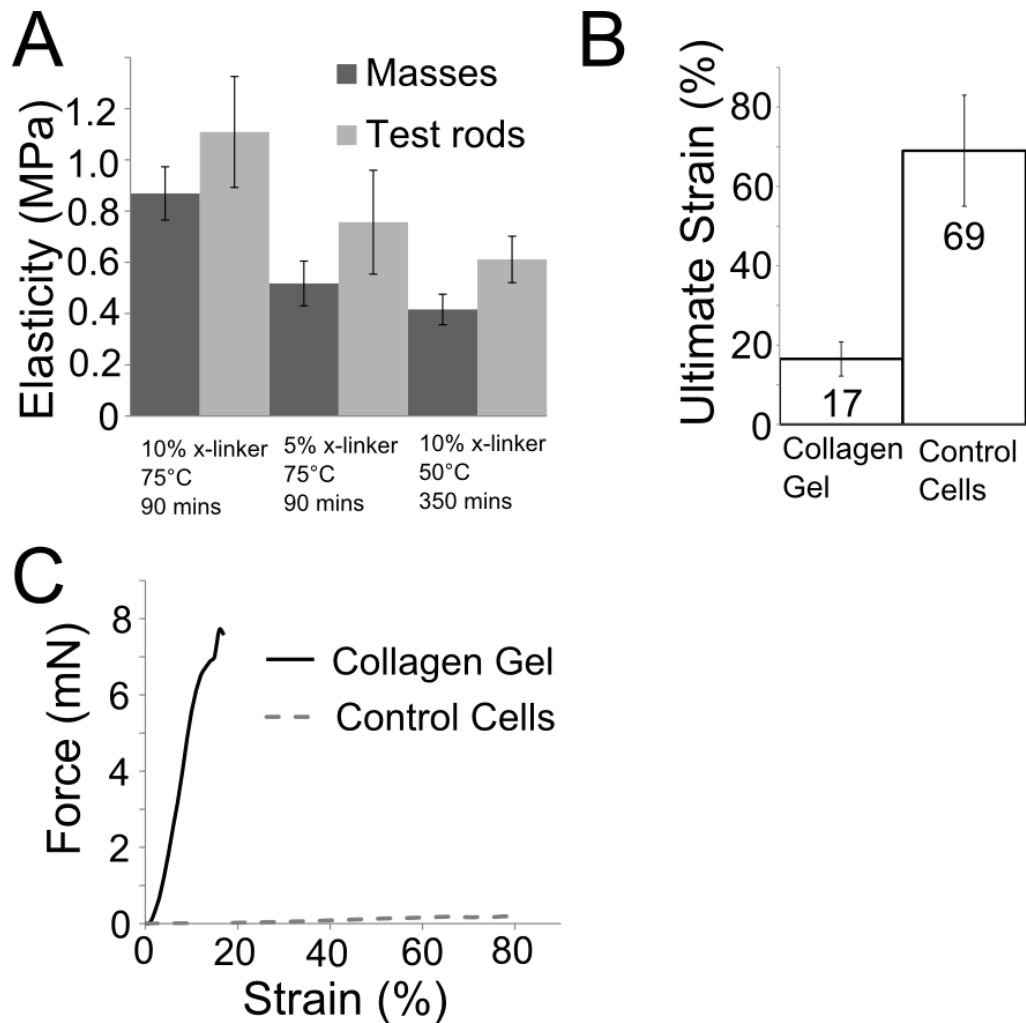
Figure 41 : Calibration of the testing device by comparison with other materials and methods

(A) The elastic moduli of PDMS strips measured using either the stretching device or gravity loading were in good agreement with one another as well as values reported in the literature (161, 162). (B) Measured ultimate strain and force response of freshly polymerised collagen gels and cell monolayers. Monolayers had a 3-fold higher average ultimate strain than freshly polymerised collagen gels. Because gels were much thicker (~1 mm) than the cell monolayers (~10μm), they displayed a much larger force response in experimental measurements (C). Therefore, ascertaining the mechanical properties of the cell monolayer in a composite measurement experiment is complex.

As an additional control I measured the stress strain response of the collagen scaffold and compared this to suspended monolayers. Suspended monolayers had very different mechanical properties to the collagen scaffold. Scaffolds were much stiffer and have a much lower ultimate strain than measured for monolayers (***Figure 41*** B, C). Freely suspending monolayers allows for direct measurement of their mechanical properties without the influence of the substrate.

CORRECTION IN THE MEASURED STRAIN DUE TO CHANGES IN THE MONOLAYER REST LENGTH

Upon examining the layer morphology after substrate digestion it is possible to see that the layers are not flat. This signifies that the layers have no pre-stress, but also implies that the zero extension does not correspond to zero planar strain. In the initial stages of extension the monolayers are "unravelled" until they become taut. In order to correct for this offset L_0 I employed a small correction to the monolayer rest length and hence the strain (***Figure 42***). The fact that the monolayers are not flat arises due to the geometry of the collagen scaffold that is formed between the test rods. By using simple geometrical considerations, the difference in the rest length and the distance between the test rods can be conservatively estimated to be about 5% and is incorporated as a correction to the strain in measurements of elasticity and ultimate strain.
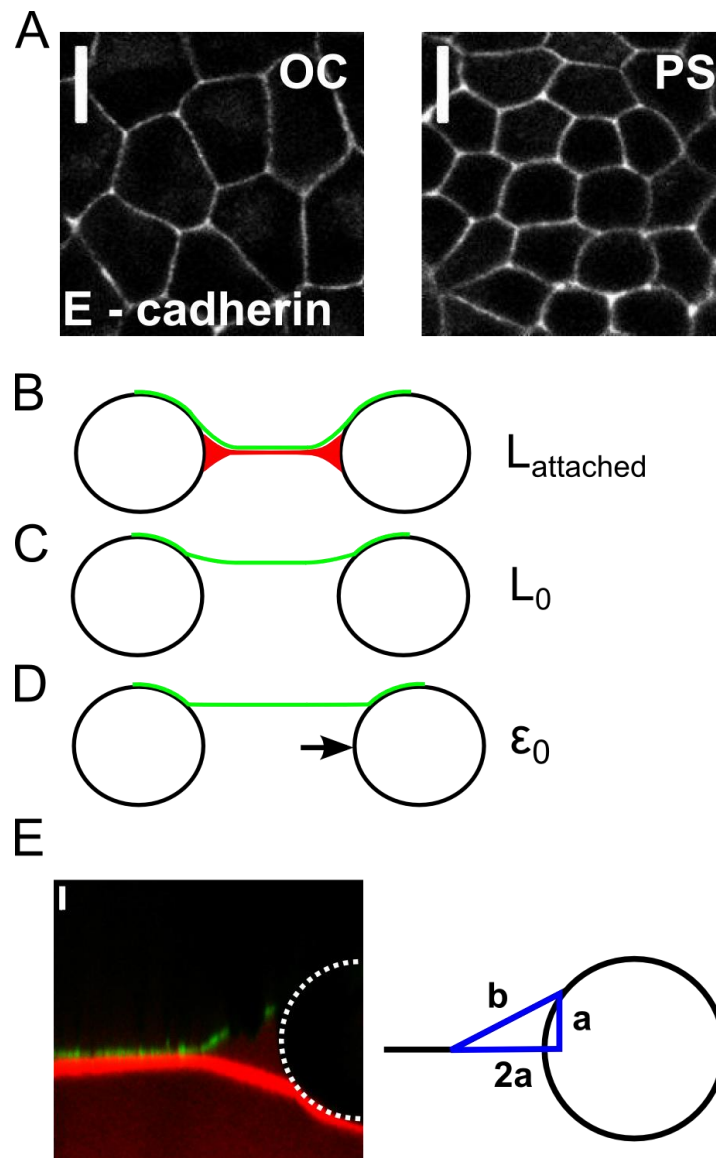
Figure 42 : Calculation of monolayer rest length

(A) When I compared images of monolayers attached to substrate to images after substrate removal, cells attached to substrate (left, OC: On Collagen) appeared more spread and had a larger projected surface area than cells without substrate. Indeed, culture of monolayers on my devices introduces a small offset between monolayer rest length ($L_{attached}$) and initial test rod separation (L_0). Hence, a small extension must be applied to the monolayers before they become taut (D). The first step of my culture process involves polymerising a small drop of collagen between the two test rods. Because the drop remains suspended between the two rods by capillarity, it acquires a characteristic dumbbell shape before it gels (red, B and E). Next, cells are seeded onto the collagen and grow to cover the upper surface of the collagen matrix (green, B). Due to the geometry of the collagen scaffold, the rest length of the cell layer is larger than the distance between the test rods. Hence, after digestion of the collagen, the cell monolayer is not taut between the rods (C), though cell contraction (A, PS) may compensate for some of the extra length. Therefore, a small extension must be applied to the monolayer before it becomes flat at zero strain (D). After substrate removal, the monolayer sags under its own weight between the two test-rods and this may be the source of the slight anisotropy in long axis orientation observed prior to strain application. (E) Simple geometrical considerations approximating the shape of the collagen scaffold to a triangular wedge suggest that monolayer rest length L attached is larger than the original separation between test rods L_0 by ~5%.

v.   MATERIALS AND METHODS

GENERAL

Measurements were performed using Leibovitz-L15 CO_2 independent medium supplemented with 10% FBS. All measurements in this chapter were conducted at room temperature.

DEVICE FABRICATION

Separate devices were used for force measurement and high magnification imaging due the short working distance of high magnification immersion objectives (280 μm for a 60x UPLSAPO water immersion objective, N.A=1.2).

Device fabrication: Force measurement devices

Thick walled borosilicate capillaries (l=100 mm, 5 μl graduated micropipette, Camag, Muttenz, Switzerland) were heated in their centre for a few seconds with a micro-pen blowtorch (Gosystem, Cheshire, UK) and bent into a "U" shape. The extremities of the capillary were brought to within 1.5 mm of one another. Capillaries were cut to size by gently breaking them with pliers. One arm was left long (~34mm) to act as a rigid reference rod and the other cut short (~4mm) to serve as a connection for the flexible test rod (*Figure 38*). A small length of capillary was cut to make a reference sleeve (~4mm). This covers a portion of the flexible test rod close to its connection to the rigid rod allowing for manipulation by the motorised micromanipulator, and projection of the un-deflected position of the flexible wire (*Figure 37*). A 0.1 mm diameter NiTi alloy wire (Euroflex, Pforzheim, Germany) was cut to length, dipped into UV curing glue (Loctite Glassbond, Henkel, Cheshire, UK) and threaded into the static rod. Another wire of similar length was dipped in glue, threaded firstly into the reference sleeve, and then into the connection for the flexible rod. The glue was cured by exposing to UV light for 5 minutes on a UV transilluminator (VWR, Leicestershire, UK). Two pieces of Tygon tubing (~4mm length, 0.25 mm i.d., 0.76mm o.d., Norton Performance Plastics, Ohio, USA) were dipped into glue, threaded onto the end of each the wire and exposed to UV light for 5 minutes. Excess Tygon tubing and wire was cut from the end of the devices. Finished test rod devices were washed in 70% ethanol followed by water. The test rods were glued to the bottom of 50 mm plastic bottomed petri dishes (BD flacon,

Oxford, UK) making sure that the ends of the rods were more than 1mm above the bottom of the dish. Prior to adding the collagen support layer, a small block of PDMS (1mm by 4mm wide) was placed in between the flexible and static rods to keep them at a constant separation until the cells had been seeded.

Device fabrication: High magnification imaging devices

A similar manufacturing process was used with the exception that thinner capillaries (od. 0.9 mm, 1 µl capillary, Camag) and thicker 0.2 mm NiTi wire were used. By making the reference sleeve capillary cover the full length of the flexible rod, both of the testing rods are rigid, with one rod acting as a "hinged lever" (*Figure 38*). This adaptation of the device allows for the strain on the monolayer to be directly controlled. To image with high magnification objectives (working distance ~280µm), the device had to be positioned as close to the bottom of the dish as possible. To accomplish this, the device was temporarily secured into a glass bottomed petri dish (Intracell, Herts, UK) with a small amount of plasticine (Blu Tak, Bostik, Leicester, UK) and the cells cultured as normal. Once cells were confluent, the culture medium was removed from the dish, and the device flipped over before being attached to the bottom of the dish with hot glue. Using this method, the monolayer could reproducibly be suspended approximately 100-200µm above the bottom of the dish, within reach of high magnification objectives.

CELL CULTURE ON DEVICES

Collagen type 1A (Cellmatrix, Nitta Gelatin inc., Japan) was reconstituted on ice in the following proportions: 5 parts collagen, 2 parts water, 2 parts 5xDMEM (PAA, Colbe, Germany) and one part sterile reconstitution buffer (2.2 g $NaHCO_3$ in 100ml of 0.02 N NaOH and 200 mM HEPES). A 10µl droplet of reconstituted collagen solution was deposited between the device test rods and stayed suspended by capillarity. Devices were placed at 37ºC for 90-120 minutes and allowed to dry giving a thin layer of collagen between the test rods. The collagen support was rehydrated by depositing a 10µl droplet of culture medium on the collagen and scant medium on the base of the dish to maintain a humidified atmosphere. Confluent flasks of MDCK cells were re-suspended to a concentration of 5 million cells per ml. The culture medium was aspirated from the collagen support, and a 5µl droplet of the re-suspended cell solution (corresponding to ~25000 cells) was placed onto the

collagen support and incubated at 37ºC for 30 minutes. Care was taken whilst seeding the cells onto the devices to ensure that the cell suspension remained on the top of the scaffold and that coverage included the rods themselves. The Petri dish containing the device was then filled with 6ml of culture medium such that the test rods were completely submerged. The PDMS block was removed from between the rods. After 48-72 hours, the collagen scaffold was removed by enzymatic digestion with 2 mg.ml^{-1} type 2 collagenase solution (Worthington, NJ, USA) in Leibovitz L-15 solution (Invitrogen, Paisley, UK) with 10% FBS for one hour. The collagenase solution was then gradually exchanged from the dish with Leibovitz L-15 solution and 10% FBS.

IMMUNOSTAINING OF CULTURE SETUP

To establish the effectiveness of the collagenase digestion, devices were fixed before and after treatment and stained with antibodies against collagen. To minimise use of reagents, miniature devices were made and enclosed in a glass bottomed chamber with a diameter of 10 mm. Devices had two rigid rods made by bending a capillary and cutting the ends to a final length of 5 mm. MDCK cells stably expressing PH-PLCδ-GFP were cultured on the devices as previously described and then fixed with 1.5 % paraformaldehyde in DMEM at room temperature for 15 minutes. When washing samples, partial fluid exchanges were necessary to prevent damage to the monolayer. Devices were stained with a monoclonal mouse anti-collagen antibody (Sigma Aldrich, Gillingham, UK, dilution: 1:25, 1 hour) followed by a goat anti-mouse Alexa 647 secondary antibody (Invitrogen, dilution: 1:100, 1 hour). Blocking steps and washes were performed with a solution of PBS with 10 mgml^{-1} BSA. To obtain profile view images of the culture devices stained samples were imaged the same day with a 10x (UPLSAPO) objective with confocal ZX slices were taken with a pixel size of 4.5 μm.

IMMUNOSTAINING OF MONOLAYERS TO ASSESS CELL POLARITY

After removal of their substrate and being put under tension for 3 hours, monolayers were fixed in 4% formaldehyde in PHEM buffer for 20 min (120mM PIPES, 50mM HEPES, 20mM EGTA and 4mM magnesium acetate), permeabilised for 30 min in 0.5% Triton X-100, blocked 30 min in 0.05% BSA-PBS and incubated overnight

with following primary antibodies: ZO-1 (rabbit, 1:50 dilution, Invitrogen), β-catenin (mouse, 1:100 dilution, Invitrogen) or gp135 (mouse, 1:20, a kind gift from Prof Karl Matter, UCL), incubated 6 hours with secondary antibodies (Rat anti-mouse Alexa488 for β-catenin or gp135, Invitrogen) or Alexa 647 (for ZO-1, goat anti-rabbit, Invitrogen), and counterstained with DAPi and Phalloidin-TRITC (1:200 dilution, Invitrogen). Acquisitions were done on a SPE Leica confocal microscope equipped with a 63x dipping objective. z-stacks were acquired with a 0.5 μm step and zx-sections were then generated using Imaris (Bitplane) software.

MICROSCOPY TECHNIQUES

Microscopy

Wide-field imaging was performed on an Olympus IX-71 inverted microscope. Confocal imaging was performed on an Olympus IX-81 equipped with an FV-1000 confocal head. For imaging the entire epithelial sheet, a 2x objective (2x PLN, Olympus) was used. For high resolution imaging samples were imaged using a 60x water immersion objective (UPLSAPO, Olympus, N.A = 1.2, W.D = 280 μm). Fluorescent proteins were imaged using the following excitation and emission: GFP was excited at 488 nm and emission was collected at 525 nm, m-Cherry was excited at 543 nm and emission was collected at 617 nm.

Macroscopy

The test rods were imaged using a Canon FD macro-lens (Canon, Surrey, UK) interfaced to a Hamamatsu EMCCD camera (Hamamatsu Orca ER, Hamamatsu UK, Hertfordshire, UK) piloted with micromanager (Vale Lab, UCSF(163)) and held in a custom support giving a top down view of the dish (***Figure 37***). The dish was mounted onto a custom made white Perspex stage which gives high contrast with the black oxide finish of the NiTi wire, enabling accurate tracking of the rod positions.

VOLUME CHANGE AND PROTEIN LOCALISATION MEASUREMENTS

To image protein localisation and cell volume during extension at high magnification, confocal images and stacks with 0.47 μm steps in z were acquired after digestion with collagenase and then at five successive 0.3 mm increments in extension. The strain in the monolayer was measured using macroscope images of the whole device.

All image analysis for quantitative measurements was implemented in MatLab (Mathworks, Natick, MA, USA).

Calculation of the tissue-level strain field by texture correlation

To estimate the real strain field in the sheet under tension, I used sum of squared difference template matching(164). The sheet was subdivided into a grid (with a node spacing of 15 pixels) (***Figure 47***, 0%, *blue*). The displacement of the grid nodes from one image to the next was found by computing the intensity cross-correlation of small image areas (30 by 30 pixels) around each node at subpixel resolution within a region of 90 by 90 pixels in the subsequent frame (***Figure 47***, 50%, *blue*). The correct position from one frame to the next was taken as the one with the highest correlation. The template was updated from one frame to the next. The deformation of each grid element relative its original dimensions allows computation of the strains ε_{xx}, ε_{yy}, and ε_{xy} at different extensions (***Figure 47***). Strain distributions were almost uniform across the sheet up until delamination.

Segmentation of monolayers into individual cells

Cells stably expressing E-cadherin-GFP were imaged with a 60x magnification objective to observe changes of cell shape and cellular arrangement within the monolayer under tension. In collaboration with Loic Peter, I developed routines for the segmentation of monolayers. To segment the images we followed a Hessian-based method for the detection of curvilinear structures (165), which in this case are ridges of intensity. We first pre-processed the image I by applying a Gaussian filter, and then we computed each pixel in the Hessian matrix:

$$H(x,y) = \begin{pmatrix} \dfrac{\partial^2 I}{\partial x^2}(x,y) & \dfrac{\partial^2 I}{\partial x \partial y}(x,y) \\ \dfrac{\partial^2 I}{\partial y \partial x}(x,y) & \dfrac{\partial^2 I}{\partial y^2}(x,y) \end{pmatrix}$$

This matrix is always real-valued and symmetric and thus has two real eigenvalues $\lambda(x,y)$ and $\mu(x,y)$ (with $\lambda \leq \mu$). At the top of a ridge of intensity we expect the

smallest eigenvalue to be negative with a high absolute value, while the associated eigenvector $\vec{u}$ gives the direction perpendicular to the ridge. We thus define a local measurement of ridgeness $R(x, y)$ at each pixel(x, y), as:

$$R(x, y) = \begin{cases} 0 & if \ \lambda(x, y) \geq 0 \\ -\lambda(x, y) & if \ \lambda(x, y) < 0 \end{cases}$$

R is therefore high on ridges, while remaining close to 0 on other parts of the image. Thresholding R returns a first approximation of the location of the ridge. To increase accuracy and ensure that each edge will be segmented as a single line, the position of the ridge is then computed by fitting the Taylor second-order polynomial $T(x, y)(t)$ in the direction $\vec{u}$ independently for each pixel. As described in (165), we keep (x, y) only if the derivative $T'(x, y)$ vanishes on the interval $[-\frac{1}{2}, \frac{1}{2}]$.

Since we are observing a cellularised tissue, we can assume that the map of the edges will be a closed mesh. Although most of the pixels are correctly classified by treating them independently, holes in the middle of a line or isolated detection artefacts can remain. This prompts the development of a restoration method. We first delete all of the objects which have less than a user-specified number of pixels, in order to suppress the isolated false positives. We then locate dead ends in my segmentation result (points which are located at the extremity of a line and attempt to close the mesh (***Figure 43***)). Each dead-end d at the extremity of a line l is evolved according to the following rule: either we can prolong l until another part of the mesh is successfully encountered, or l is deleted.

Let us denote $\vec{v}$ the tangent vector of the line l at d. For each point a classified as belonging to an edge, we define a score $f_d(a)$ measuring the relevance to link d to a:

$$f_d(a) = (\max\left(1 - \frac{r}{r_{max}}, 0\right))^{\alpha} \times \max(1 - \frac{2}{\pi}|\theta|, 0)$$

Where (r, θ) are the polar coordinates of the point a in the polar coordinate system of pole d and polar axis $\vec{v}$. This represents a compromise between distance to d and deviation with respect to $\vec{v}$. r_{max} and denotes the distance between d and a beyond

which $f_d(a) = 0$. The constant α balances the importance of the distance criterion relative to the direction criterion and is user specified. For $\alpha = 3$, accurate segmentation was achieved. If one or more points a have a positive score, d is linked to the one showing the best score. If not, the dead-end is treated as a segmentation artefact and removed (***Figure 43***).
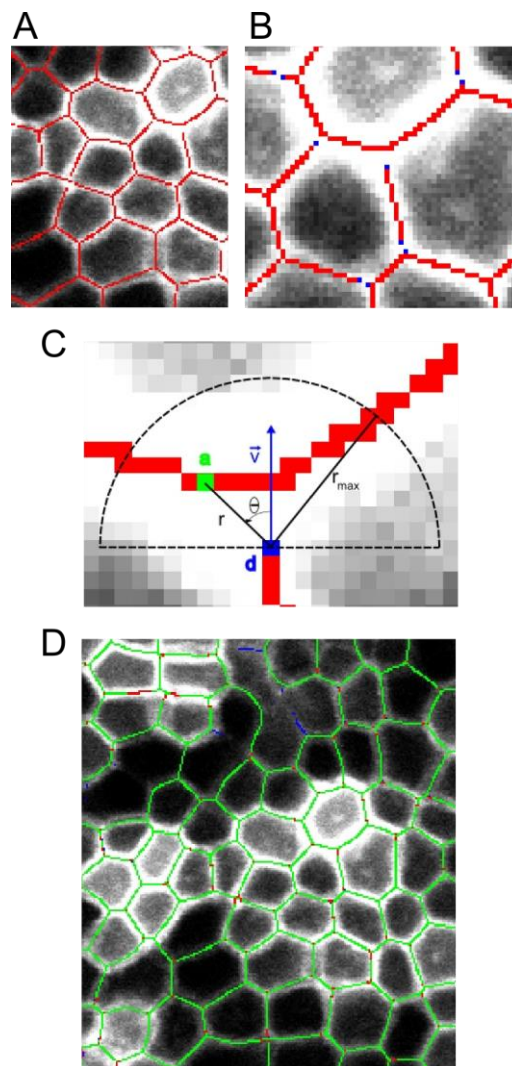
Figure 43 : Segmentation of monolayers

(A) Using a Hessian based approach, we identify ridges of intensity in images of E - cadherin GFP labelled cells. By treating pixels independently we can identify the cell edges but do not always obtain an entirely closed mesh (red). (B) Dead ends (blue dots) are identified at the extremity of unclosed lines and are evolved according to a selection rule. (C) For each dead end, we look for edge pixels (shown in red) in the semicircle of radius r_{max} oriented according to $\vec{v}$. If none are found, d and the line it belongs to are deleted. A score $f_d(a)$ is computed for each of the pixels within the semicircle (for example, the green pixel) and d linked to the pixel a having the highest score. For the case shown in (C), d will be linked vertically to the closest pixel because it maximises both the distance and direction criteria. (D) The final segmentation result shows the original pixels identified using the Hessian approach in green, pixels that are added by the restoration are shown in red, and pixels that are removed by the restoration are shown in blue.

Calculation of cellular-level strain

The cellular strain tensor was calculated as outlined (81). After segmenting monolayers into individual cells (***Figure 48***), the principal axes of inertia were found from the cell area. The average resting orientation and length of the principal axis was compared at different extensions to determine the average strain of the cells within the layer.

MECHANICAL MEASUREMENT PROTOCOLS

Initial loading measurements

Petri dishes containing devices were mounted onto the microscope stage and secured with plasticine. The motorised micromanipulator arm was positioned at the top extremity of the reference sleeve and the manual micromanipulator arm at the top of the reference rod. Monolayers were extended at a rate of 0.01 mm.s^{-1} (~1%.s^{-1}) until failure. Monolayers were imaged at a frame rate of 0.5 s/frame at low magnification with the inverted microscope and the test rod positions were imaged with a top down macroscope.

Creep measurements

A feedback loop was used to keep the level of stress constant following a step increase in stress. This custom feedback routine was written and implemented in LabView (National Instruments, Austin, Texas, USA). To evaluate the creep response at two different stress amplitudes the motor was driven 0.3 mm at a speed of 0.75 mm.s^{-1} (~75%.s^{-1}), giving a stress of ~3.0kPa (High stress) or driven 0.1 mm giving a stress of ~0.7kPa (Low stress). Under these conditions, target stress was reached in less than ~0.5s and maintained for 200s.

Stress relaxation measurements

For stress relaxation measurements, a custom feedback routine was written and implemented in LabView (National Instruments, Austin, Texas, USA). Monolayers were initially subjected to a pre-conditioning cyclic loading (8 cycles, at a speed of 0.01 mm.s^{-1} or 1%.s^{-1}, 0.3 mm initially then a 0.1mm amplitude cycle). For stress relaxation measurements the motor was driven 0.3 mm at a speed of 0.75 mm.s^{-1} (~75%.s^{-1}), giving a strain of ~20-30 %. The strain was measured with the microscope images and maintained constant by the feedback routine.

Fitting monolayer stress relaxations

To measure the monolayer apparent viscosity, I fitted the stress relaxation data after 5 seconds with the standard linear solid model. The standard linear solid consists of a spring - dashpot (with apparent elasticity E_2 and viscosity η) in parallel with another spring (elasticity E_1) (166). In this model, stress decays exponentially with a time constant $\tau_1 = {}^{\eta}/_{E_2}$ when the material is subjected to a step strain ε at t= 0, $\sigma(t) =$

$$\varepsilon_0 \left[E_1 + E_2 e^{-t/\tau_1} \right].$$

Dependence of elasticity on load cycle number and strain rate

For cyclic loading measurements, monolayers were initially subjected to a 0.3mm extension at 0.01mms^{-1} (~1%.s^{-1}) and then left at constant strain for ~500 seconds. Monolayers were then subjected to three different amplitudes of loading cycles (~3%, ~10% and 20% in amplitude) and the stress strain response of each cycle calculated. The elasticity was measured from the slope of the extension phase of each cycle. To examine the effect of strain rate on measured elasticity, monolayers were initially subjected to a 0.3mm extension at 0.01mms^{-1} (~1%.s^{-1}) and then left at constant strain for ~500 seconds. Cyclic loading was then performed at the following drive rates; 0.005 mms^{-1}, 0.01 mms^{-1}, 0.02 mms^{-1}, and 0.05 mms^{-1} (respectively 0.5, 1, 2, and 5%.s^{-1}) for 0.05mm (~5%) cycles.

vi. RESULTS

TISSUE-LEVEL MECHANICS

Using the experimental setup, I characterised the mechanical properties of monolayers of Madine-Darby Canine Kidney (MDCK-II) cells, a classic epithelial cell model. In the following, unless otherwise noted, I report the engineering strain: $\varepsilon = \Delta L/L_0$, with ΔL the monolayer length change and L_0 its original length (***Figure 42***).

TIME DEPENDENT MECHANICAL PROPERTIES

Living tissues are intrinsically viscoelastic with both physical and biological phenomena contributing to their time-dependent mechanical properties. Measured physiological strain rates in monolayer covered tissues range from ~0.04%.s^{-1} in developing drosophila embryos (81) and tens to hundreds of %.s^{-1} in alveolar

epithelium and mitral valve tissue (167, 168). To investigate the time-dependent mechanical properties of monolayers, I characterised their creep response to two distinct step increases in stress, respectively with high (3 kPa) and low stress (0.7 kPa). When the monolayers were subjected to low stress loading, strain increased rapidly in response to stress application before reaching a plateau that subsisted over 200s (*Figure 44*, grey line). In contrast, when high stress loading was applied, no plateau was reached and strain increased continually with time (*Figure 44*, black line). Plotting these response curves in log-log scale revealed that monolayer creep followed a power law in response to high stress step loading but not following low stress step loading (*Figure 44*, *inset*), suggesting that monolayers behave as viscoelastic solids below a certain critical stress and as complex fluids above. Power law creep responses had an exponent $\beta=0.15\pm0.03$, slightly less than generally reported for single cells ($\beta\sim0.3$-0.5,(70)). Consistent with the observations upon low stress loading, stress relaxation of monolayers also reached a plateau after ~50s (*Figure 45*), suggesting a limit elastic behaviour. Estimates of relaxation rates for computational models and comparative studies could be obtained by fitting stress relaxations with appropriate rheological models (*Figure 45*). The time-scales needed to reach a plateau in low stress creep and stress relaxation experiments (~50s) suggest that the short time scale response likely arises from biochemical properties of the cell, such as the turnover of the actin cytoskeleton ($t_{1/2}\sim 10s$ in MDCK cells (56)). However, further work will be necessary to fully explore the rheological behaviours of monolayers and determine what biological mechanisms underlie their time-dependent mechanical behaviour.
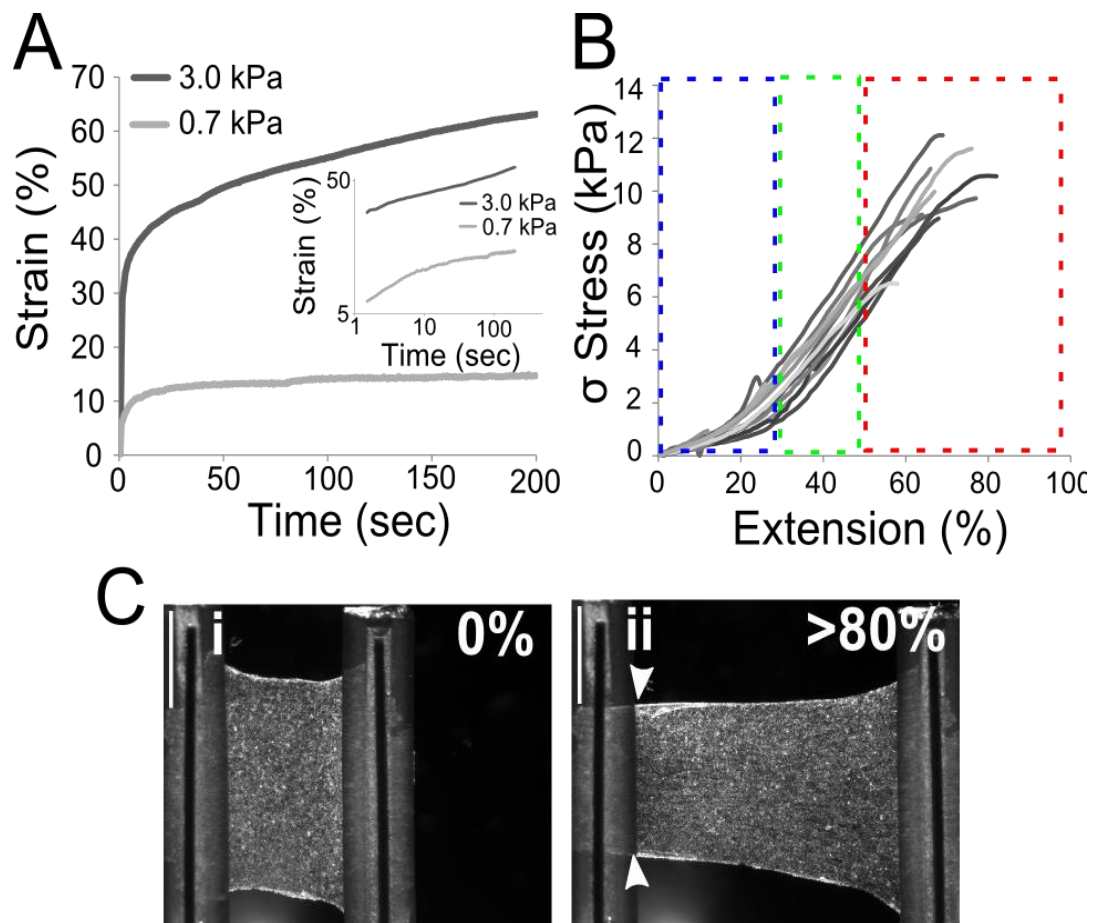
Figure 44 : Mechanical properties of monolayers

(A) Creep response following step application of low (0.7 kPa, light grey) and high (3 kPa, dark grey) stress. The plotted responses are averaged over at least 6 experiments each. At low stress, following a rapid increase in strain, monolayers reached a plateau that lasted for the remainder of the experiment. At high stress, no plateau was reached and strain increased continually with time. Inset: Creep response curves plotted in log-log scales. The creep response at high stress (dark grey) was well fitted by a linear function with slope β=0.15±0.03; whereas at low stress the creep response was not linear. (B) Stress-extension curves shown for 12 different monolayers. All curves displayed three distinct regimes of loading: i) an initial "toe" region (blue box) as the monolayer becomes loaded under tension, ii) a linear extension regime (green box) from which an elastic modulus can be calculated, iii) a plateau (red box) which corresponds to plastic deformation and eventual failure. (C) Deformation of a monolayer under stretch. Images acquired by bright-field microscopy for a monolayer at 0 and >80% extension. At >80% extension, the monolayer delaminated from the test rods (arrows) suggesting that cell-cell adhesion is stronger than cell-substrate adhesion for this geometry. s.b =1mm.
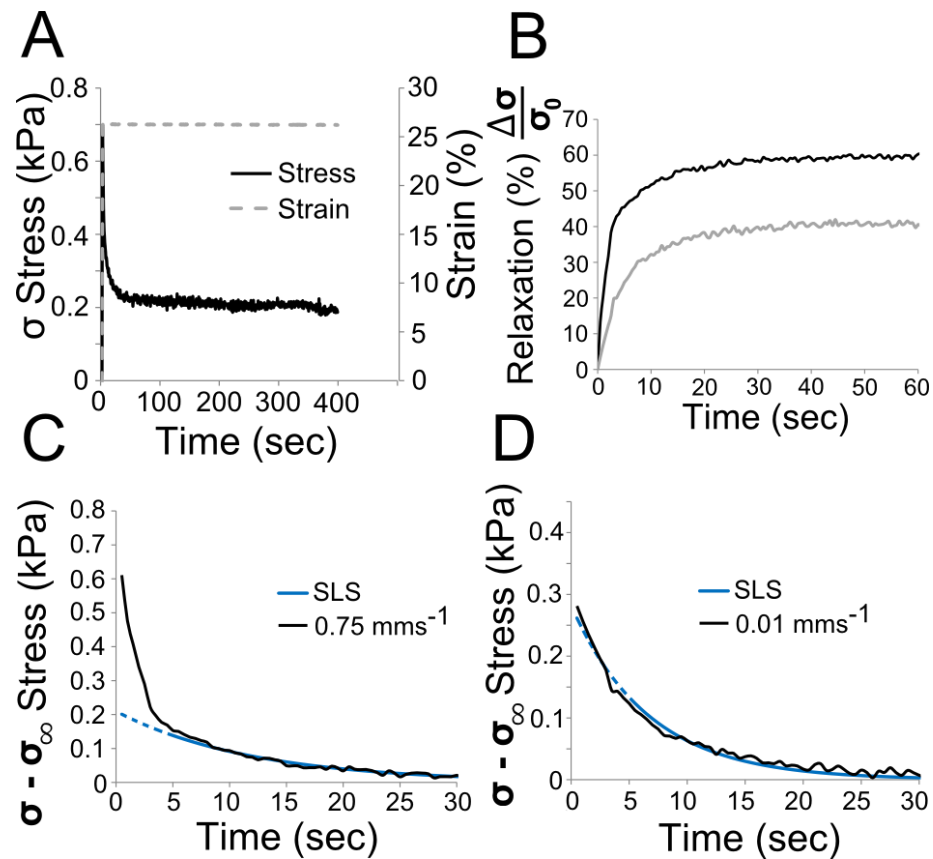
Figure 45 : Stress relaxation in monolayers

(E) Stress relaxation in monolayers. After initial extension with a strain rate of 75%.s-1, stress relaxed to ~40% of its initial value over ~50s. At longer timescales, a plateau was reached and stress remained constant for up to 400s. (F) Percentage relaxation as a function of time for monolayers stretched fast and slowly. Curves averaged over n = 4 measurements show that for slow strain rates (dark grey) stress relaxation is reduced from 68 % to 34 % in the initial 30 seconds of relaxation compared to fast strain rates (light grey). (G-H) Stress relaxation in monolayers loaded at high (75%.s⁻¹, G) and low (1%.s⁻¹, H) strain rates. (G) Representative monolayer stress relaxation after high strain rate loading. Monolayers loaded at high strain rates (75%.s⁻¹) had biphasic stress relaxations with a high amplitude fast initial phase followed by a lower amplitude slower phase. After the first 5 seconds following loading, the relaxation of monolayers loaded at high strain rates could be well fitted with the standard linear solid model and yielded an apparent viscosity η~0.3±0.1MPa.s (N=6, blue). (H) Representative stress relaxation after low strain rate loading. Monolayers loaded at low strain rates (1%.s⁻¹) had largely monophasic stress relaxations and the fast response observed in response to high strain rate loading was absent. After the first 5 seconds following loading, the relaxation of monolayers loaded at low rates could be well fitted with the standard linear solid model and yielded an apparent viscosity similar to that of the fast loading rates (p=0.78 when compared to one another).

TIME INDEPENDENT MECHANICAL PROPERTIES

I decided to focus on monolayer mechanical properties at strain rates between 0.5-5%.s⁻¹ that are relevant for embryonic morphogenesis where only very slow deformations take place (~0.04%.s⁻¹,(81)). To determine the elasticity and ultimate strength of monolayers, I acquired stress-extension curves until failure (***Figure 44***

B). For strain rates between 0.5-5%.s^{-1}, I did not observe any significant differences in measured elastic moduli, indicating that loading was quasi-static (***Figure 44***). I settled on a strain rate of 1%.s^{-1} for my measurements. All stress-extension curves shared the following characteristic features: i) a "toe" region where stress increased slowly and non-linearly between 0 and ~25% extension, ii) a linear region between ~25% and ~50% extension, iii) mechanical failure (for extensions >70%), following a plateau of the curve. Monolayer stiffnesses were computed from the slope of the stress-strain curves in the linear region where monolayer differential stiffness was constant (***Figure 46*** B). Measured stiffnesses averaged E=20 ± 2 kPa, two orders of magnitude larger than the elasticity of MDCK cell monolayers probed in the transversal direction by AFM (28). The average strain at failure was a remarkable 69 ± 14 % with failure occurring by delamination, suggesting that adhesion of monolayers to the test rods was weaker than cell-cell adhesion (***Figure 44*** C). In cyclic loading experiments, monolayer stiffness did not vary significantly with loading cycle for small amplitudes (~3%) but did for larger amplitudes (~10-20%) (***Figure 46*** C, D). This suggested that MDCK monolayers underwent partial fluidization for large strain amplitudes, consistent with the existence of a threshold stress in my creep experiments and reports examining fluidization in single MDCK cells (71).

CELLULAR-LEVEL MECHANICS

To understand how monolayers could withstand such large deformations, I analysed deformations at the cell and tissue level. Monolayer deformations can occur through two mechanisms: shape change of the constituent cells, or re-organisation of cellular arrangement within the monolayer, a process known as intercalation (169). One mechanical hallmark of intercalation is that the tissue-level strain tensor does not match the cellular-level strain tensor (81) and therefore I compared tissue-strain to cell-strain during extension.
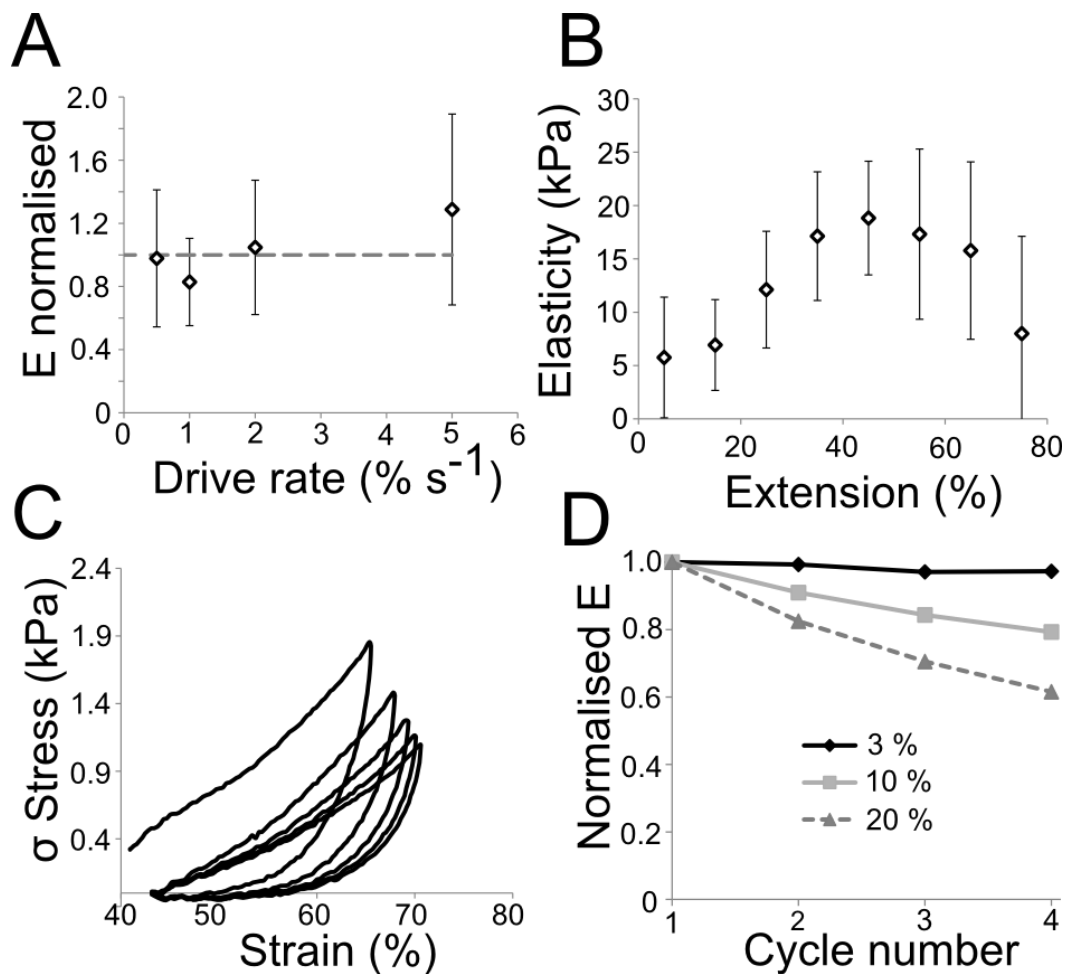
Figure 46 : Elastic properties of monolayers

(A) Dependence of monolayer elasticity on strain rate. The measured monolayer elasticity did not significantly differ over a broad range of drive rates (0.005 - 0.05 mms^{-1}, 0.5-5%.s^{-1}). N= 5 experiments for each rate. (B) Differential stiffness of monolayers sampled in 10% increments in extension did not vary significantly between ~25% and 55% extension. (C) After initial application of stress and subsequent relaxation, monolayers were subjected to cyclic oscillations with an amplitude of 10% strain while driving length change at a rate of ~1%.s^{-1}. As the cycle number increased, the slope of the loading phase decreased. (D) Elastic modulus as a function of cycle number for different strain amplitudes. For the lowest strain amplitude (~3%), the elastic modulus remained constant with increasing cycle number. At higher amplitudes (10 and 20%), the elastic modulus showed a significant decrease with increasing cycle number.
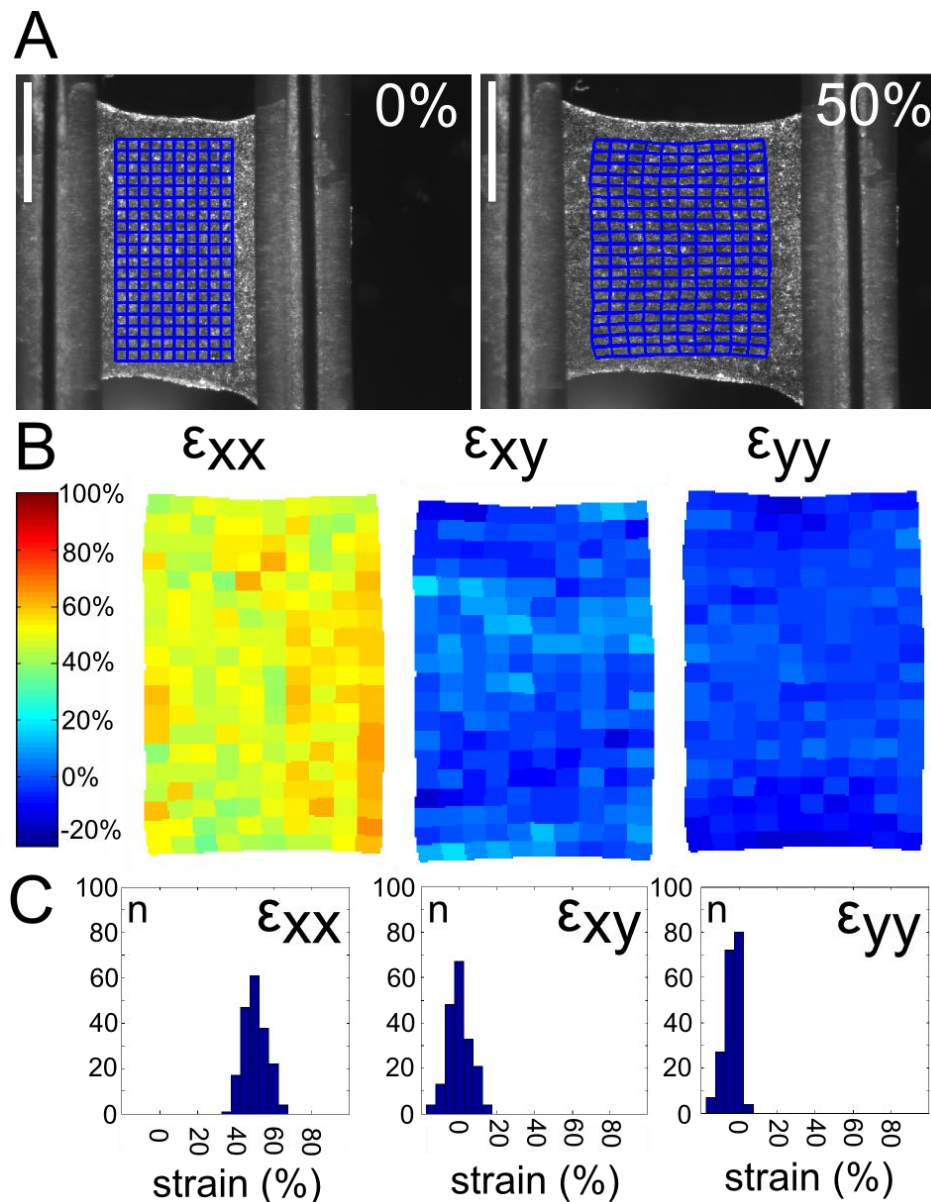
Figure 47 : Monolayer mechanics at the tissue level

(A) Using texture correlation, the position of nodes in the blue grid in the monolayer at rest could be tracked in the stretched monolayer. s.b=1mm. (B) This allowed computation of the strain fields εxx, εxy and εyy. (C) εxx was quasi uniform throughout the monolayer with values close to the engineering strain computed from the applied extension (50±6%). εyy was also quasi uniform throughout the sheet with average values close to zero (-3±4%). Some contraction was apparent at the edges, typical for a material of this geometry. εxy was also quasi uniform throughout the monolayer during extension (0±6%). In the graphs, n denotes the number of grid cells that have a given strain.

I measured the tissue-level strain by computing the displacement of a grid of points within the monolayer using low magnification images (texture correlation, ***Figure 47*** A). The tissue-strain ε_{xx} throughout the monolayer was tightly distributed around the value of the imposed engineering strain (***Figure 47*** B). In the transverse direction, tissue-strain ε_{yy} was tightly distributed around zero (***Figure 47*** C) but displayed a

small inward contraction at the outer boundaries. This level of homogeneity in the strain distribution within monolayers, suggest that monolayer cellular constituents have similar mechanical properties such as elasticity. Indeed, in AFM measurements on MDCK cells there is a much smaller variation in the measured Young's modulus than in other cell types such as HeLa cells (29, 144).
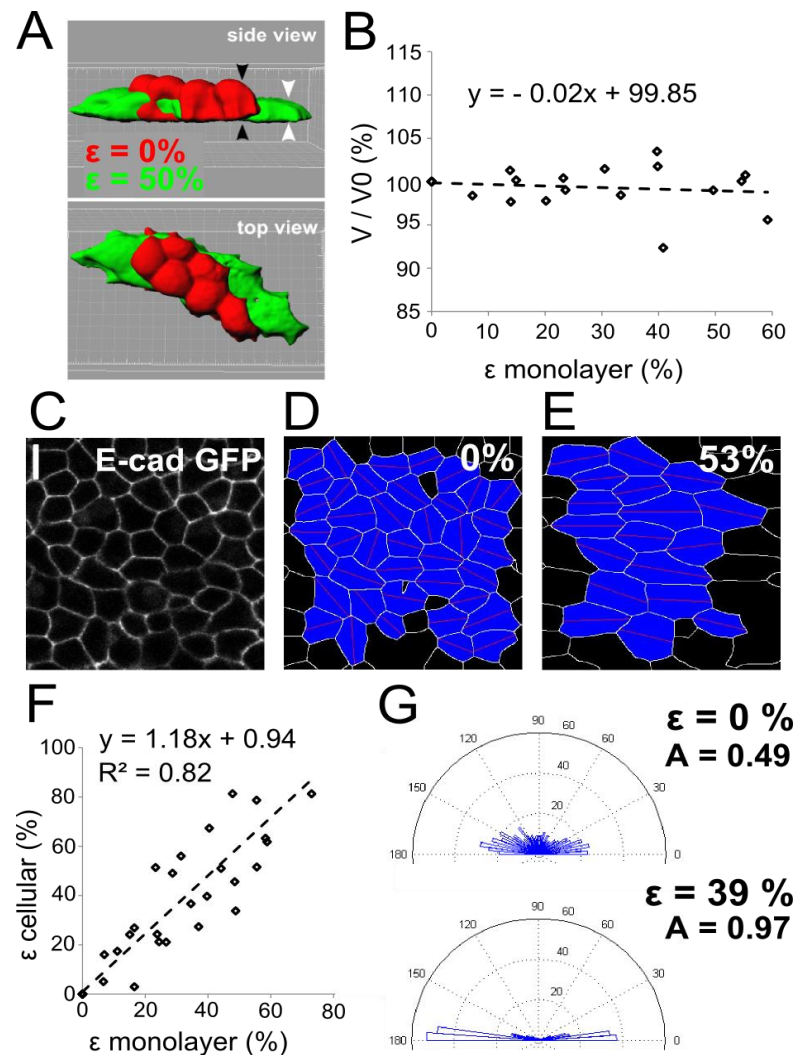
Figure 48 : Monolayer mechanics at the cellular level

(A) 3D isosurface reconstruction of cells within a monolayer before (red) and after (green) extension. Cell height decreased with extension (side view: black arrowheads: 0% strain, white arrowheads: 50% strain) but cellular projected area increased (top view). (B) Cell volume was conserved during extension, suggesting that the constituent cells are close to being incompressible. (C-E) Segmented images of cells expressing E-cadherin-GFP were used to calculate the cellular deformations before and during stretch. (F) The calculated cellular strain matched the monolayer strain near perfectly indicating that no intercalation takes place during extension. (G) The orientation of cell long axes prior to stretch was widely distributed with a small bias along the x-axis but, during stretch, cells orientations were nearly exclusively aligned with the direction of extension. The anisotropy of alignment calculated as A = 1 - (% aligned perpendicular)/(% aligned parallel) almost doubled when the cells were subjected to 39% strain.

Since there was no large contraction of the monolayer in the "y" direction I examined the deformation of the cells perpendicular to the monolayer plane. Three-dimensional isosurface reconstructions of cells within the monolayer during extension revealed that the increase in projected surface area of the monolayer (*Figure 48* A, B, *top view*, *red* before extension, *green* at 50% strain) was accompanied by thinning of the cells (*Figure 48* A, *side view*) perpendicular to the monolayer plane, thereby maintaining cell volume close to being constant to within about 10% of the measured volume (*Figure 48*). This indicated that the large increase in projected surface area was not accommodated by the small magnitude of the inward contraction noted at outer boundaries, but rather by preferential thinning of the monolayer in the transverse direction. This also suggested that, as expected from their cytoskeletal organisation, monolayers have anisotropic mechanical properties. During wound healing experiments, monolayers are put under tension by the migration of leader cells at the wound edge leading to the highly heterogeneous distribution for ε_{xy} that guides collective migration of cells within the monolayer (103). In contrast, in my experiments ε_{xy} was tightly distributed around zero presumably due to the uniform displacement applied to the monolayer and the far more rapid application of stress. The homogeneity of the strain field demonstrates that the cell properties, in particular their stiffnesses, are uniform across the monolayer. The absence in suspended epithelia of the typical patterns of cell displacements visible on dense epithelia migrating on a substrate (103) confirmed the requirement for strong cell-substrate interactions in the emergence of collective migration patterns.

Cellular-level strain was characterised by measuring changes in cellular long axis length and orientation from segmented images of monolayers expressing E-cadherin GFP (*Figure 48*) (81). During extension, the cellular-level strain matched tissue-level strain, suggesting that no intercalation took place. Average long axis orientation changed from having a small level of orientation anisotropy at rest, possibly due to small magnitude stresses arising after substrate removal, to displaying a much stronger anisotropy when the sheet was stretched. Together these data show that cultured monolayers extend solely due to shape change of their cellular components with no intercalation. Consistent with these mechanical

measurements, on the time-scales of the experiments (~5min), microscopy examination of the cells did not reveal cell re-arrangement or division.

SUB-CELLULAR MECHANICS: CYTOSKELETAL DEFORMATION DURING EXTENSION

The cytoskeleton plays a major role in single cell mechanical properties and, in tissues, loss of function mutations affecting cytoskeletal and adhesive proteins lead to increased fragility. I examined cytoskeletal organisation during monolayer extension paying particular attention to protein constituents of adherens junctions and desmosomes, key structures in intercellular junctions.

In adherens junctions, adjacent cell membranes are tethered to one another by classical cadherins (E-cadherin in epithelial cells) that are linked intracellularly to the actomyosin cytoskeleton thus integrating neighbouring cells into a mechanical syncytium (54). Removal of the collagen substrate led to a general rounding of the cells and a reduction in projected surface area due to loss of basal adhesion (**Figure 49**, **Figure 42**) but no change in the localisation of E-cadherin was observed. E-cadherin distribution was not affected by extension (**Figure 49** A-C). F-actin remained localised to intercellular junctions (**Figure 49** D-F) but had a somewhat less uniform distribution under strain displaying some enrichment at tricellular junctions. Myosin regulatory light chain (MRLC), a component of myosin II whose phosphorylation controls contractility, displayed a dramatic change in localisation upon removal of the substrate and under strain. Localisation changed from being cytoplasmic to punctate and junctional (**Figure 49** G-I), reminiscent of myosin localisation in embryonic epithelial tissues (18) and suggesting a role for myosin contractility in monolayer mechanics.
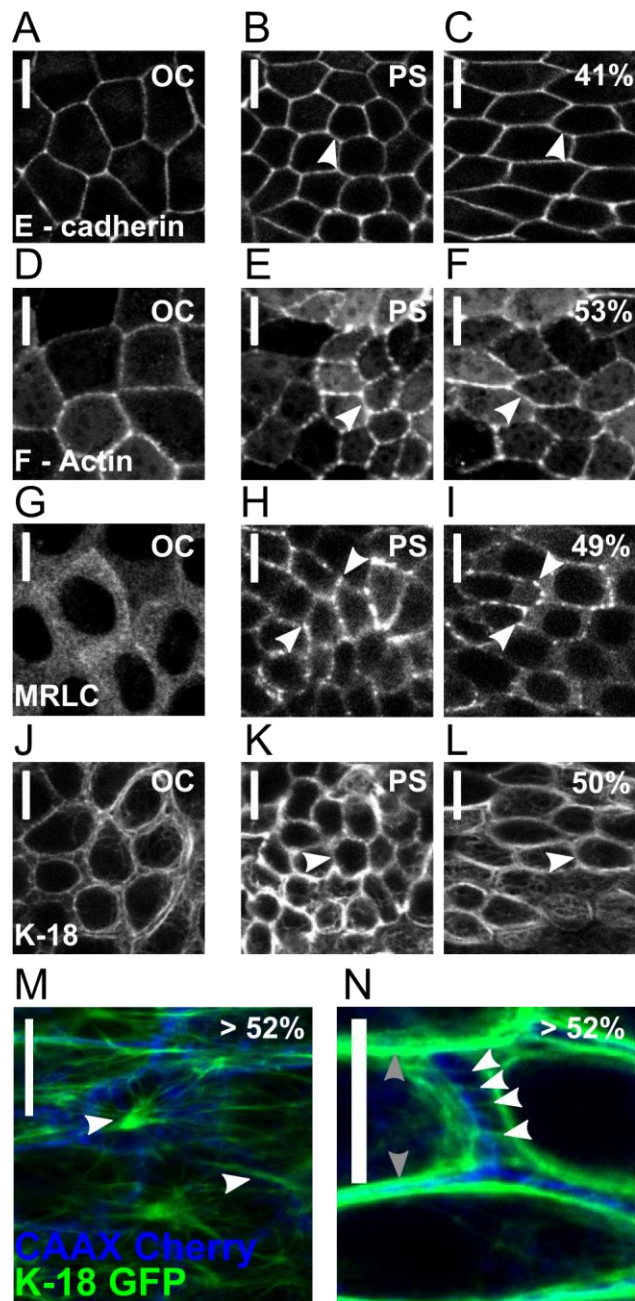
Figure 49 : Subcellular organisation in stretched monolayers

OC: On collagen, PS: pre-stretch, % indicates the percentage strain (s.b=10 μm). (A-C) E-cadherin GFP remained localised to cell junctions in all conditions. (D-F) Life-act GFP, an F-actin marker, remained localised at cell junctions throughout extension but appeared less uniform at low stretch. (G-I) The regulatory light chain of myosin was primarily cytoplasmic in cells on collagen (G), but underwent a dramatic relocalisation to cell junctions pre-stretch (H) and at high extension (I). (J-L) The keratin 18 filament network spanned the entire monolayer on collagen (J) and looked largely bundled prior to extension (K). Application of stretch induced rearrangement of the filaments, suggesting that they served to transmit stress across cell boundaries (arrowhead). (M) Keratin filaments (green) formed an intercellular network with nodes at the cell centres (white arrows) that linked cells to one another across cell boundaries (blue) in stretched monolayers. (N), keratin filaments (green) appeared tensed across cell junctions (blue) perpendicular to the direction of extension (white arrows) and bundled (grey arrows) at cell junctions parallel to the direction of extension.

Desmosomes link the keratin intermediate filaments of neighbouring cells to one another forming a second supracellular cytoskeletal network. Genetic mutations of keratins or desmosomal proteins result in fragile epithelia (51). On collagen, keratin localised perinuclearly with short wavy segments linking cells to one another (*Figure 49* J-N). After removal of collagen, keratin filaments remained perinuclear and, at high strain, filaments became aligned in the direction of stretch. When imaged at higher magnification, a keratin supracellular network was clearly visible and filaments straddling intercellular junctions appeared taut and aligned parallel to the direction of extension (*Figure 49* M, N, *arrows*). This change in conformation from wavy at low strain to taut at high strain suggested that keratins are involved in a non-linear mechanical response of the monolayer to stretch, as proposed by others (37, 43) and consistent with the mechanical properties of isolated keratins and keratin networks in cells (43, 45).

SUBCELLULAR PERTURBATIONS LEAD TO CHANGES IN TISSUE-LEVEL MECHANICS

I examined how perturbations at the molecular scale affected mechanics at the tissue-scale. The filamentous actin network is a key contributor to cellular elasticity in isolated cells and, in monolayers, it is the main component of adherens junctions. When I depolymerised the actin cytoskeleton of monolayers with latrunculin B, their stiffness decreased by ~50% compared to controls ($E_{latrunculin}$=10±6 kPa, p<0.01, *Figure 50*), demonstrating the importance of F-actin for monolayer stiffness. Next, I asked if myosin contractility contributed to monolayer mechanics based on its localisation to intercellular junctions (*Figure 49*). Treatment of monolayers with Y27632, an inhibitor of rho-kinase mediated contractility, led to a significant ~36% decrease in stiffness (E_{Y27632}=13±6 kPa, p<0.01). Hence, myosin contractility contributes to monolayer elasticity. Ultimate strain did not change with treatments affecting F-actin or contractility (*Figure 50* C).
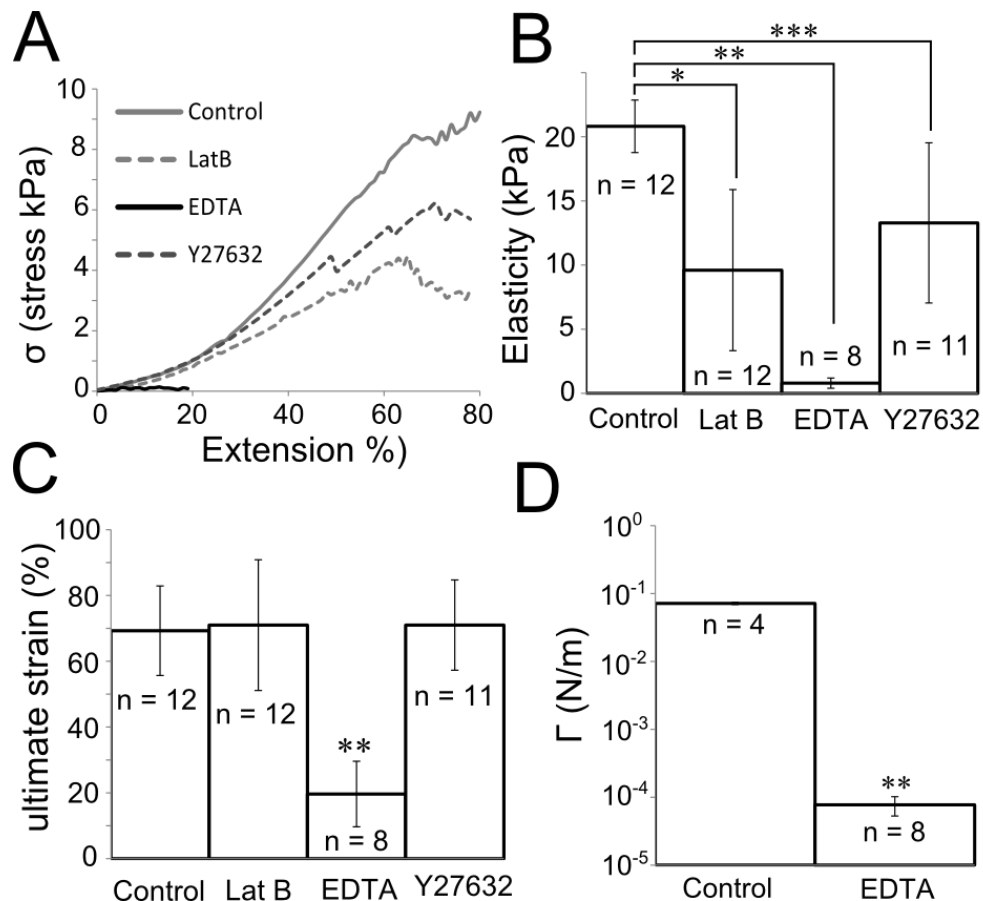
Figure 50 : The actin cytoskeleton and intercellular adhesion contribute strongly to monolayer mechanics.

*(A) Average loading curves for monolayers treated with Latrunculin B (dashed light grey line), Y27632 (dashed dark grey line), and EDTA (black line) compared to control monolayers (light grey line). (B) Monolayer stiffness was significantly reduced by treatment with latrunculin B, Y27632, or EDTA ($N_{control}=12$, $N_{latrunculin}=12*$, $N_{EDTA}=8**$, $N_{Y27632}=11***$, $p < 0.01$ for all measurements). (C) Ultimate strength was not significantly reduced by treatment with latrunculin B or Y27632 but was significantly reduced by treatment with EDTA (**). (D) EDTA treated monolayers showed a considerable reduction in their adhesion energy density ($p<0.01$ **).*

INTERCELLULAR ADHESION IN MONOLAYERS

During ultimate strength measurements, control monolayers normally failed by delamination from the test rods, suggesting that failure occurred through rupture of cell-substrate adhesions. To induce failure through rupture of intercellular adhesions, I concentrated stresses by narrowing tissue width by nicking the unstressed sheet prior to extension (***Figure 51***). Under these conditions, failure occurred at local strains of 110±18 %, more than doubling monolayer length. Cracks initiated in the monolayer close to the nicked region and propagated perpendicularly to the direction of stretch across the sheet width. Knowing the monolayer elasticity (E=20 kPa) and

choosing the cell diameter $a \sim 10$ µm as a natural length-scale within the monolayer, I could estimate the intercellular adhesion energy density per unit area Γ within the monolayer: $\Gamma = a\sigma^2/2E = 0.07$ N.m^{-1} with $\sigma = 17 \pm 3$ kPa the ultimate stress (**Figure 52**). The average force required to separate two cells within the monolayer is $F_{doublet} \sim F_{total}/N \sim 1.7$ µN with $F_{total} \sim 202$ µN the applied force onto the monolayer at rupture and $N \sim 120$ the average number of cells in the narrowed monolayer width. Experiments on cell doublets brought into contact for ~ 30min yield a separation force $F \sim 200$ nN (94), almost 9 times lower than in monolayers, perhaps reflecting the less mature intercellular junctions formed during the shorter intercellular contact time.
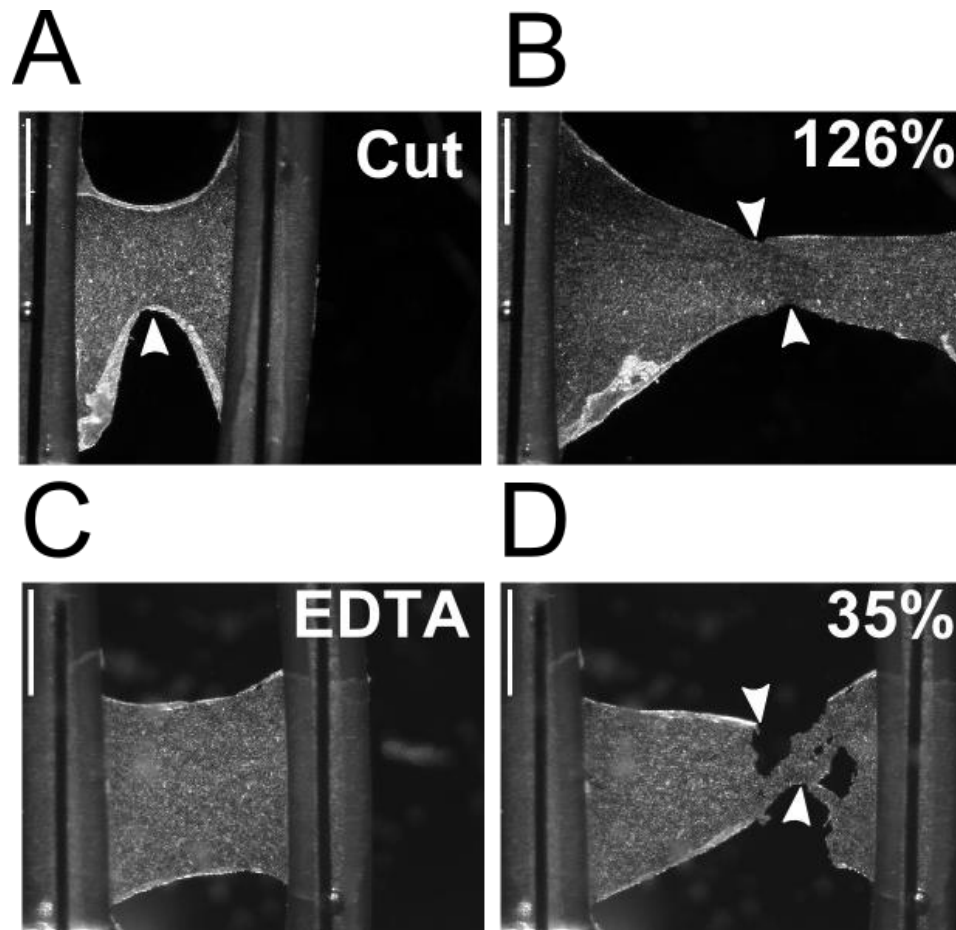
Figure 51 : Images of monolayer fracture

(A, B) To induce failure through intercellular adhesion rupture in control monolayers, a nick was made in the sheet to concentrate stresses (white arrow). Monolayers failed at high strain by crack formation (B, 126% strain, arrows). Cracks within the monolayer formed in the region of highest local tissue strain (arrows). With EDTA treatment (C-D), cracks formed within the monolayer and propagated perpendicularly to the direction of extension (white arrows). s.b=1mm.

To verify the well-known importance of intercellular adhesion for monolayer mechanics, I disrupted cell-cell adhesion by treatment with EDTA, a divalent cation chelator that blocks cadherin-mediated adhesion. Monolayers treated with EDTA still retained sufficient integrity to withstand a small strain (<20%) but at moderate strain (~25%), cracks formed within the monolayer propagating perpendicularly to the direction of stretch (***Figure 51***). Monolayers had significantly reduced stiffnesses and intercellular adhesion energy densities compared to controls (E=0.8±0.4 kPa and Γ=8.10^{-5} N.m^{-1}, p<0.01 in both cases) (***Figure 50*** D), quantitatively confirming the well-studied role of cadherin-mediated intercellular adhesion in monolayer integrity.

$$\delta E_{elastic} = a\,\delta x\,\frac{1}{2}E\varepsilon^2$$

$$\delta E_{adhesion} = \Gamma\,\delta x$$

cracks propagate when

$$\sigma > \left(\frac{\Gamma 2E}{a}\right)^{1/2}$$

with $\sigma = E\,\varepsilon$
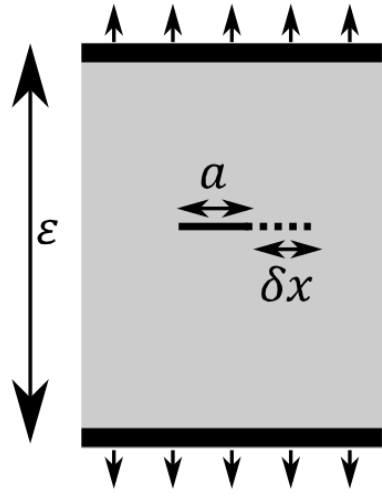
Figure 52 : Estimating the adhesion energy density from experiments

I derive an estimate of the adhesion energy density in MDCK monolayers by using a standard fracture mechanics approach. It consists of comparing the variations of elastic and surface energies when the length a of a crack increases by δx. The elastic energy released by the crack growth can be calculated from the tissue strain and the tissue stiffness (for simplicity, linearity here is assumed). The increase in adhesion energy is Γδx. At failure, the released elastic energy becomes greater than the cost in adhesion energy, causing catastrophic crack growth and failure. In an epithelium, the average cell length is chosen as the characteristic length scale "a" for the initial mechanical defects (or internal crack size).

vii.   DISCUSSION

Using a novel culture system, I give the first detailed characterisation of monolayer mechanical properties at the tissue, cellular, and subcellular scales. Live imaging during mechanical testing allowed me to relate cellular and subcellular level phenomena to tissue level mechanics. I have shown that on short timescales,

extension of monolayers results solely from deformation of their constituent cells rather than intercalation and monolayers can withstand more than a doubling in length before failure through rupture of intercellular junctions. Monolayer stiffness were two orders of magnitude larger than the elasticity of their constituent cells measured in the transversal direction by AFM (28) in monolayers grown on glass substrates, pointing to a large anisotropy in monolayer mechanical properties. The actin cytoskeleton accounted for half of the stiffness of monolayers, presumably due to its importance in forming intercellular junctions. A closer inspection of the time-dependent behaviour also revealed that monolayers display complex time-dependent rheological properties. As in single cells (71), application of high amplitude cyclical strain loading led to partial fluidisation of the monolayers but the exact biological mechanisms underlying this behaviour remains unknown. Consistent with experiments in embryos and isolated cells (15, 18), myosin contractility contributed significantly to monolayer mechanics, as suggested by localisation of MRLC to intercellular junctions. Within monolayers, the average force required to separate two cells was ~1.7μN, ~9 fold larger than measured in pairs of isolated cells (94), perhaps due to the more natural configuration of the cells or the fuller maturation of intercellular junctions. Based on these measurements and the contribution of actin to the monolayer stiffness, at fracture the actin network in each individual cell bears ~840nN, comparable to the maximal line tensions of ~400nN borne by stress fibres (33). As expected, disruption of cell-cell adhesion led to a dramatic fragilisation of cell sheets. Taken together, these data paint a picture of monolayer mechanics where cells adhere strongly to one another and therefore can pull strongly on one another through myosin contractility, leading to the development of a tissue-level tension and as a result higher stiffness. Furthermore, such a process may be self-reinforcing with higher tensions leading to myosin recruitment (170) and increased myosin duty ratio (171). Imaging of intermediate filaments revealed that their aspect changed from wavy to taut with increasing monolayer extension, suggesting that at high strains they become load-bearing and therefore may be involved in a non-linear mechanical response of the monolayer as previously proposed (37, 43). Such an interpretation would be consistent with the fragile epithelium symptoms observed in patients with mutations in keratins or desmosomal proteins (51) but will necessitate further study. Together my experimental methods pave the way for quantitative

investigations of monolayer mechanics at the subcellular, cellular, and tissue level and they should be widely applicable to any cell type forming strong intercellular junctions.

During development, embryonic morphogenesis is in large part due to changes in the organisation and mechanics of epithelial monolayers. Over the past decade, researchers have devised many experimental and computational techniques to study the mechanics of morphogenetic events but a detailed understanding has been hindered by a lack of tools to directly characterise monolayer mechanics. For example, measurements of embryonic epithelial tension by laser cutting rely on monitoring tissue recoil, something that depends both on monolayer tension and stiffness. Though laser cutting successfully allows for comparative measurements of tension to be performed, combining it with my techniques would allow for deconvolution of tension and stiffness and hence absolute measurements. In computational models of epithelia, the contribution of cytoskeletal components (in particular actomyosin contractility) to monolayer mechanics is often accounted for by spring networks and line tensions acting in bulk or at intercellular junctions (80, 159). However, estimating the value of the corresponding parameters has proven challenging. Based on my measurements of monolayer stiffness for a range of biological and chemical perturbations, suitable estimates of these parameters can be obtained. Direct experimental measurements of monolayer mechanics combined with computational models will therefore allow for a better understanding of multicellular aggregate mechanics.

viii.   SUMMARY

The main goal of this thesis was to develop a device that could measure the mechanical properties of monolayers in the tissue plane. I determined the elasticity, time dependent properties and strength of cell monolayers. I achieved these primary goals and have made links to the cell cytoskeleton and the architecture of adherens junctions that give monolayers their supracellular mechanical properties. Further investigation would be required with mutant cell lines targeting intercellular adhesion and the cytoskeleton to further determine which structures are load bearing and are important in setting monolayer planar mechanical properties.

8. CONCLUDING REMARKS

I have measured the mechanical properties of both single MDCK epithelial cells and those of the simple epithelial tissues. In my initial measurements of single cell mechanical properties using atomic force microscopy (AFM), I identified that pyramidal tips yield elasticity values that are 2-3 fold higher than those obtained with spherical tips. This was due to an underestimation of the area of contact predicted by the hertz model for low aspect ratio pyramidal tips. In the literature there is a broad range of values reported for the elastic modulus of biological materials. In particular, there is a large variation between measurements made with different experimental tools on the same cell type. Modifications to current methods such as using spherical AFM tips are important to standardise mechanical measurement protocols, in order to obtain comparable data between experimental techniques.

Using AFM I found that the Young's modulus of MDCK cells to be ~400Pa when probed at small strain. This value was heavily dependent on the integrity of the actin cytoskeleton. However, this value is not necessarily the most informative measurement, as in most physiological cases monolayers and simple tissues are deformed in the plane. Currently experimental tools to probe the planar mechanical properties of cell monolayers are lacking and hence I developed methods to fill this gap.

MDCK monolayers were grown onto thick collagen gels and used large AFM indentation measurements to measure the monolayer-gel composite mechanical properties. I have shown this measurement protocol to be sensitive to the establishment of intercellular junctions and the net monolayer tension. However, I did not quantitatively evaluate the level of tension independently from the monolayer elasticity. This investigation would benefit from further analysis of the indentation response of composite materials to large indentation and perhaps a finite element model to better interpret the data. Despite this limitation, I have shown that this method can yield valuable information about the mechanical properties that coincide with the formation of adherens junctions. Due to the ease of operation of AFM, time resolved measurements of the mechanical properties are easy to perform. Since cells

can be replated onto the substrate, this method offers a reference measurement just after replating, where no intercellular junctions have been established as a baseline value.

In parallel with this method I developed a novel tool to stretch monolayers directly in the monolayer plane. Using this technique I have shown that monolayers display non-linear elastic and complex rheological properties. Tensile testing of monolayers yielded an elastic modulus that is ~20 times larger than the value obtained via AFM measurements. Furthermore monolayers exhibited increased "fluid like" behaviour when exposed to large stresses. This type of response has previously been reported in single cells in response to stretching of their substrate (71).

The reason for the increased elastic modulus when measuring in the monolayer plane is due to the subcellular structures that are stimulated with this type of loading. Epithelial cells form actin rich intercellular junctions that are highly contractile. Actin is known to be one of the main determinants of the mechanical properties of single cells, and hence actin rich structures are important mechanically. AFM indentation cannot probe the mechanical properties of intercellular junctions and hence their mechanical contribution is often overlooked. Furthermore, I have shown that the intermediate filament network becomes taut between cells and may contribute to monolayer mechanical properties at high strain. Again this could be overlooked in indentation measurements where strains are purposefully kept small. One of the most interesting results of these measurements was the ability of monolayers to accommodate large levels of strain without mechanical failure. Specialised adhesion structures interface the cytoskeletons of monolayer constituent cells endowing monolayers with a high resistance to fracture.

Although much is now known about the mechanical behaviour of single cells and whole organs, comparatively less is known about the mechanical behaviour of simple multicellular aggregates. There have been some seminal advances in understanding aggregate mechanical behaviour, particularly in their collective migration (96, 103, 172) and the coordination of forces during development (81, 173). The work presented in this thesis provides one of the first mechanistic characterisations of simple epithelial tissues, and provides links with the biological

determinants of monolayer mechanical properties. This data will be highly valuable for computational studies of epithelia that require calibration with experimental values. The methods presented in this thesis pave the way for a new level of tissue characterization. By bridging across the relevant length-scales and time-scales these tools provide a unique foundation on which to build a more general and accurate understanding of tissue physiology and pathologies.

9. FUTURE WORK

ADDITIONAL DESIGN MODIFICATIONS TO THE MONOLAYER STRETCHER

Optimising the imaging setup

The device design and described in ***chapter 7*** addresses several of the key requirements to measure monolayer mechanical properties. The one major disadvantage is that different devices had to be created to image the cell monolayer at high magnification and to perform mechanical measurements. This was largely due to the working distance limitations of inverted microscope high magnification objectives. Force measurement devices had to be created with enough clearance from the bottom of the petri dish so that there was no physical contact with the cantilevered beam. This would result in friction and an overestimation of forces. There are two possible solutions to this problem. Firstly, with further development the whole design with the macroscope could be made smaller allowing for enough room for a top down dipping objective to be used to image the monolayer. This would remove the need to use inverted microscopes and associated problems with working distance. Secondly, force measurement devices can be flipped over in the same way as for the high magnification devices but a spacer used to maintain a specific level of clearance from the bottom of the petri dish.

Long timescale measurements

One of the main problems with long timescale measurements with these devices is delamination of cells from the testing rods. On long timescales monolayers are contractile, and this contractile force increases the degree of delamination. In order to solve this problem, one of two strategies can be adopted. Firstly, the area of contact between the monolayer and the test rod can be increased in comparison to the suspended monolayer. This reduces the stress at the point of contact with the test rod and hence the degree of delamination. This can be accomplished by cutting away part of the monolayer that is suspended as described in ***chapter 7***, or by increasing the area of the extremities of the test rods that cells are cultured onto.

Short timescale measurements

In the described method forces are measured optically through the deflection of a cantilevered beam. The rate of sampling is hence limited to the speed at which the camera can acquire images and process them. For short timescale measurements on the order of 10ms, this is a limiting factor. By modifying the system to incorporate a high speed force transducer measurements can be obtained at a much higher sampling rate, which is necessary to observe fast relaxation dynamics such as the redistribution of pressure throughout cells.

CORTICAL POLARISATION GUIDES ORIENTED CELL DIVISION

In collaboration with Julien Bellis, we have shown that cells within monolayers that are under stretch have oriented cell divisions. This is an interesting observation in the context of embryo mechanics and development, where cell division could serve to relax tissue level stresses. By stretching monolayers with the system that I have described in *chapter 7* and immunostaining layers, my preliminary results suggest that cell shape elongation causes cortical accumulation of proteins such as Numa and Gaplhpai that orient the mitotic spindle along the cell long axis.

FRACTURE MECHANICS OF EPITHELIAL LAYERS

In *chapter 7* I have made initial characterisations of the fracture mechanics of epithelial cell monolayers. By cutting away part of the layer I created a critical crack that propagates through the monolayer, and estimated the adhesion energy density. Cutting the cell layer in this fashion is not particularly accurate and characterising fully the fracture mechanics of these layers requires a different approach. By interfacing the setup with a laser cutting system, the whole monolayer could be placed under a constant stress and single cell junctions cut to relieve stress. This could enable for the first time, measurement of the stress along intercellular junctions quantitatively through the stress released at the monolayer level.

10.   ENGD PUBLICATIONS

*equally contributed

Julien Bellis*, <u>Andrew R Harris</u>*, Andrea Dimitracopoulos, Maxine Lam, Tom Wyatt, Guillaume Charras and Buzz Baum, *Axial cortical polarization guides oriented division to relax an epithelium following an imposed stretch.* In preparation 2013

<u>Harris, A.R.</u>,*. A. Daeden*, and G.T. Charras. *The emergence of a supracellular stiffness in epithelial monolayers coincides with the assembly of mature contractile adherens junctions.* Submitted to Current Biology, 2013

Moeendarbary, E., L. Valon, M. Fritzsche, **<u>A.R. Harris</u>**, D.A. Moulding, A.J. Thrasher, E. Stride, L. Mahadevan and G.T. Charras, *The cytoplasm of living cells behaves as a poroelastic material*. Nature Materials, 2013

Terry, S.J., A. Elbediwy, C. Zihni, **<u>A.R. Harris</u>**, M. Bailly, G.T. Charras, M.S. Balda, and K. Matter, *Stimulation of Cortical Myosin Phosphorylation by p114RhoGEF Drives Cell Migration and Tumor Cell Invasion.* PLoS ONE, 2012. **7**(11): p. e50188.

<u>Harris, A.R.</u>, L. Peter, J. Bellis, B. Baum, A.J. Kabla, and G.T. Charras, *Characterizing the mechanics of cultured cell monolayers.* Proceedings of the National Academy of Sciences, 2012.

Recommended in F1000:

http://f1000.com/prime/717967200

Previewed in Nature Methods:
http://www.nature.com/nmeth/journal/v9/n12/full/nmeth.2265.html

<u>Harris, A.R.</u> and G.T. Charras, *Experimental validation of atomic force microscopy-based cell elasticity measurements.* Nanotechnology, 2011. **22**(34): p. 345102-345102.

Kajita, M., C. Hogan, **A.R. Harris**, S. Dupre-Crochet, N. Itasaki, K. Kawakami, G. Charras, M. Tada, and Y. Fujita, *Interaction with surrounding normal epithelial cells influences signalling pathways and behaviour of Src-transformed cells.* J Cell Sci. 123(2): p. 171-180.

11.   REFERENCES

1.   Lee GY & Lim CT (2007) Biomechanics approaches to studying human diseases. *Trends in biotechnology* 25(3):111-118.

2.   Fung Y-c (1996) *Biomechanics: circulation* (Springer).

3.   Fung Y-c (1993) *Biomechanics: mechanical properties of living tissues* (Springer).

4.   Engler AJ, Sen S, Sweeney HL, & Discher DE (2006) Matrix Elasticity Directs Stem Cell Lineage Specification. *Cell* 126(4):677-689.

5.   Discher DE, Janmey P, & Wang Y-l (2005) Tissue Cells Feel and Respond to the Stiffness of Their Substrate. *Science* 310(5751):1139-1143.

6.   del Rio A, Perez-Jimenez R, Liu R, Roca-Cusachs P, Fernandez JM, & Sheetz MP (2009) Stretching Single Talin Rod Molecules Activates Vinculin Binding. *Science* 323(5914):638-641.

7.   Geiger B, Bershadsky A, Pankov R, & Yamada KM (2001) Transmembrane crosstalk between the extracellular matrix and the cytoskeleton. *Nature Reviews Molecular Cell Biology* 2(11):793-805.

8.   Prager-Khoutorsky M, Lichtenstein A, Krishnan R, Rajendran K, Mayo A, Kam Z, Geiger B, & Bershadsky AD (2011) Fibroblast polarization is a matrix-rigidity-dependent process controlled by focal adhesion mechanosensing. *Nature cell biology* 13(12):1457-1465.

9.   Butcher DT, Alliston T, & Weaver VM (2009) A tense situation: forcing tumour progression. *Nature Reviews Cancer* 9(2):108-122.

10.   Yu H, Mouw JK, & Weaver VM (2011) Forcing form and function: biomechanical regulation of tumor evolution. *Trends in cell biology* 21(1):47-56.

11.   Hogan C, Dupre-Crochet S, Norman M, Kajita M, Zimmermann C, Pelling AE, Piddini E, Baena-Lopez LA, Vincent J-P, Itoh Y, Hosoya H, Pichaud F, & Fujita Y (2009) Characterization of the interface between normal and transformed epithelial cells. *Nature Cell Biology* 11(4):460-467.

12.   Kajita M, Hogan C, Harris AR, Dupre-Crochet S, Itasaki N, Kawakami K, Charras G, Tada M, & Fujita Y (Interaction with surrounding normal epithelial cells influences signalling pathways and behaviour of Src-transformed cells. *J Cell Sci* 123(2):171-180.

13.   Lodish HF, Baltimore D, Berk A, & Darnell JE (1995) *Molecular cell biology* (WH Freeman New York, NY:).

14.   Fletcher DA & Theriot JA (2004) An introduction to cell motility for the physical scientist. *Physical Biology* 1(1):T1.

15.   Fletcher DA & Mullins RD (2010) Cell mechanics and the cytoskeleton. *Nature* 463(7280):485-492.

16.   Friedl P & Gilmour D (2009) Collective cell migration in morphogenesis, regeneration and cancer. *Nature Reviews Molecular Cell Biology* 10(7):445-457.

17.   Schultz GS & Wysocki A (2009) Interactions between extracellular matrix and growth factors in wound healing. *Wound Repair and Regeneration* 17(2):153-162.

18. Rauzi M, Verant P, Lecuit T, & Lenne P-F (2008) Nature and anisotropy of cortical forces orienting Drosophila tissue morphogenesis. *Nature Cell Biology* 10(12):1401-1410.

19. Levine E, Lee CH, Kintner C, & Gumbiner BM (1994) Selective disruption of E-cadherin function in early Xenopus embryos by a dominant negative mutant. *Development* 120(4):901-909.

20. Davidson LA, Keller R, & DeSimone DW (2004) Assembly and remodeling of the fibrillar fibronectin extracellular matrix during gastrulation and neurulation in Xenopus laevis. *Developmental dynamics : an official publication of the American Association of Anatomists* 231(4):888-895.

21. Davidson LA, Marsden M, Keller R, & Desimone DW (2006) Integrin alpha5beta1 and fibronectin regulate polarized cell protrusions required for Xenopus convergence and extension. *Current biology : CB* 16(9):833-844.

22. Georges-Labouesse EN, George EL, Rayburn H, & Hynes RO (1996) Mesodermal development in mouse embryos mutant for fibronectin. *Developmental dynamics : an official publication of the American Association of Anatomists* 207(2):145-156.

23. Mogilner A & Oster G (1996) Cell motility driven by actin polymerization. *Biophysical Journal* 71(6):3030-3045.

24. Galbraith C, Skalak R, & Chien S (1998) Shear stress induces spatial reorganization of the endothelial cell cytoskeleton. *Cell motility and the cytoskeleton* 40(4):317-330.

25. Ross JL, Ali MY, & Warshaw DM (2008) Cargo transport: molecular motors navigate a complex cytoskeleton. *Current opinion in cell biology* 20(1):41-47.

26. Sedzinski J, Biro M, Oswald A, Tinevez J-Y, Salbreux G, & Paluch E (2011) Polar actomyosin contractility destabilizes the position of the cytokinetic furrow. *Nature* 476(7361):462-466.

27. Rayment I, Holden HM, Whittaker M, Yohn CB, Lorenz M, Holmes KC, & Milligan RA (1993) Structure of the actin-myosin complex and its implications for muscle contraction. *Science-New York then Washington* 261:58-58.

28. Harris AR & Charras GT (2011) Experimental validation of atomic force microscopy-based cell elasticity measurements. *Nanotechnology* 22(34):345102-345102.

29. Moeendarbary E, Valon L, Fritzsche M, Harris AR, Moulding DA, Thrasher AJ, Stride E, Mahadevan L, & Charras GT (2013) The cytoplasm of living cells behaves as a poroelastic material. *Nature materials*.

30. Gittes F, Mickey B, Nettleton J, & Howard J (1993) Flexural rigidity of microtubules and actin filaments measured from thermal fluctuations in shape. *The Journal of cell biology* 120(4):923-934.

31. Gardel M, Shin J, MacKintosh F, Mahadevan L, Matsudaira P, & Weitz D (2004) Elastic behavior of cross-linked and bundled actin networks. *Science* 304(5675):1301-1305.

32. Ratheesh A (2012) A bigger picture: classical cadherins and the dynamic actin cytoskeleton. *Nature Reviews Molecular Cell Biology* 13(10):673-679.

33. Deguchi S, Ohashi T, & Sato M (2006) Tensile properties of single stress fibers isolated from cultured vascular smooth muscle cells. *Journal of biomechanics* 39(14):2603-2610.

34. Salbreux G, Charras G, & Paluch E (2012) Actin cortex mechanics and cellular morphogenesis. *Trends in cell biology*.

35. Stricker J, Falzone T, & Gardel ML (2010) Mechanics of the F-actin cytoskeleton. *Journal of biomechanics* 43(1):9-14.

36. Müsch A (2003) Microtubule organization and function in epithelial cells. *Traffic* 5(1):1-9.

37. Ingber DE (2003) Tensegrity I. Cell structure and hierarchical systems biology. *Journal of cell science* 116(7):1157-1173.

38. Wang N, Naruse K, Stamenović D, Fredberg JJ, Mijailovich SM, Tolić-Nørrelykke IM, Polte T, Mannix R, & Ingber DE (2001) Mechanical behavior in living cells consistent with the tensegrity model. *Proceedings of the National Academy of Sciences* 98(14):7765-7770.

39. Picone R, Ren X, Ivanovitch KD, Clarke JD, McKendry RA, & Baum B (2010) A polarised population of dynamic microtubules mediates homeostatic length control in animal cells. *PLoS biology* 8(11):e1000542.

40. Fuchs E & Weber K (1994) Intermediate filaments: structure, dynamics, function and disease. *Annual review of biochemistry* 63(1):345-382.

41. Harris AR, Peter L, Bellis J, Baum B, Kabla AJ, & Charras GT (2012) Characterizing the mechanics of cultured cell monolayers. *Proceedings of the National Academy of Sciences*.

42. Fudge D, Russell D, Beriault D, Moore W, Lane EB, & Vogl AW (2008) The Intermediate Filament Network in Cultured Human Keratinocytes Is Remarkably Extensible and Resilient. *PLoS ONE* 3(6):e2327.

43. Herrmann H, Bar H, Kreplak L, Strelkov SV, & Aebi U (2007) Intermediate filaments: from cell architecture to nanomechanics. *Nature Reviews Molecular Cell Biology* 8(7):562-573.

44. Kreplak L & Fudge D (2007) Biomechanical properties of intermediate filaments: from tissues to single filaments and back. *BioEssays* 29(1):26-35.

45. Sivaramakrishnan S, DeGiulio JV, Lorand L, Goldman RD, & Ridge KM (2008) Micromechanical properties of keratin intermediate filament networks. *Proceedings of the National Academy of Sciences* 105(3):889-894.

46. Strnad P, Windoffer R, & Leube RE (2002) Induction of rapid and reversible cytokeratin filament network remodeling by inhibition of tyrosine phosphatases. *Journal of cell science* 115(21):4133-4148.

47. Blankson H, Holen I, & Seglen PO (1995) Disruption of the cytokeratin cytoskeleton and inhibition of hepatocytic autophagy by okadaic acid. *Experimental cell research* 218(2):522-530.

48. Hartsock A & Nelson WJ (2008) Adherens and tight junctions: Structure, function and connections to the actin cytoskeleton. *Biochimica et Biophysica Acta (BBA) - Biomembranes* 1778(3):660-669.

49.   Niessen C (2007) Tight junctions/adherens junctions: basic structure and function. *Journal of investigative dermatology* 127(11):2525.

50.   Me, scedil G, & Gabriele Richard TWW (2007) Gap junctions: basic structure and function. *Journal of Investigative Dermatology* 127(11):2516-2524.

51.   Getsios S, Huen AC, & Green KJ (2004) Working out the strength and flexibility of desmosomes. *Nature Reviews Molecular Cell Biology* 5(4):271-281.

52.   Green KJ & Simpson CL (2007) Desmosomes: new perspectives on a classic. *Journal of Investigative Dermatology* 127(11):2499-2515.

53.   Harris TJC & Tepass U (2010) Adherens junctions: from molecules to morphogenesis. *Nature Reviews Molecular Cell Biology* 11(7):502-514.

54.   Gumbiner BM (2005) Regulation of cadherin-mediated adhesion in morphogenesis. *Nature Reviews Molecular Cell Biology* 6(8):622-634.

55.   Brieher WM (2012) Cadherin junctions and their cytoskeleton (s). *Current opinion in cell biology*.

56.   Yamada S, Pokutta S, Drees F, Weis WI, & Nelson WJ (2005) Deconstructing the Cadherin-Catenin-Actin Complex. *Cell* 123(5):889-901.

57.   Martin AC, Gelbart M, Fernandez-Gonzalez R, Kaschube M, & Wieschaus EF (2010) Integration of contractile forces during tissue invagination. *The Journal of cell biology* 188(5):735-749.

58.   Hobbs RP & Green KJ (2011) Desmoplakin Regulates Desmosome Hyperadhesion. *Journal of Investigative Dermatology*.

59.   Liu Z, Tan JL, Cohen DM, Yang MT, Sniadecki NJ, Ruiz SA, Nelson CM, & Chen CS (2010) Mechanical tugging force regulates the size of cell–cell junctions. *Proceedings of the National Academy of Sciences*.

60.   Kobielak A, Pasolli HA, & Fuchs E (2003) Mammalian formin-1 participates in adherens junctions and polymerization of linear actin cables. *Nature cell biology* 6(1):21-30.

61.   Carramusa L, Ballestrem C, Zilberman Y, & Bershadsky AD (2007) Mammalian diaphanous-related formin Dia1 controls the organization of E-cadherin-mediated cell-cell junctions. *Journal of cell science* 120(21):3870-3882.

62.   Drees F, Pokutta S, Yamada S, Nelson WJ, & Weis WI (2005) α-catenin is a molecular switch that binds E-cadherin-β-catenin and regulates actin-filament assembly. *Cell* 123(5):903-915.

63.   Braga VMM, Del Maschio A, Machesky L, & Dejana E (1999) Regulation of Cadherin Function by Rho and Rac: Modulation by Junction Maturation and Cellular Context. *Molecular biology of the cell* 10(1):9-22.

64.   Braga VMM, Machesky LM, Hall A, & Hotchin NA (1997) The Small GTPases Rho and Rac Are Required for the Establishment of Cadherin-dependent Cell–Cell Contacts. *The Journal of cell biology* 137(6):1421-1431.

65.   Godsel LM, Hobbs RP, & Green KJ (2008) Intermediate filament assembly: dynamics to disease. *Trends in cell biology* 18(1):28-37.

66.   Yoon KH, Yoon M, Moir RD, Khuon S, Flitney FW, & Goldman RD (2001) Insights into the Dynamic Properties of Keratin Intermediate Filaments in Living Epithelial Cells. *The Journal of cell biology* 153(3):503-516.

67.   Green KJ & Gaudry CA (2000) Are desmosomes more than tethers for intermediate filaments? *Nature Reviews Molecular Cell Biology* 1(3):208-216.

68.   Landau LD, Lifshitz E, Sykes J, Reid W, & Dill EH (1960) Theory of Elasticity: Vol. 7 of Course of Theoretical Physics. *Physics Today* 13:44.

69.   Gere JM (2002) Mechanics of Materials *(Nelson Thornes).*

70.   Kollmannsberger P & Fabry B (2011) Linear and Nonlinear Rheology of Living Cells. *Annual Review of Materials Research* 41(1):75-97.

71.   Trepat X, Deng L, An SS, Navajas D, Tschumperlin DJ, Gerthoffer WT, Butler JP, & Fredberg JJ (2007) Universal physical responses to stretch in the living cell. *Nature* 447(7144):592-595.

72.   Deng L, Trepat X, Butler JP, Millet E, Morgan KG, Weitz DA, & Fredberg JJ (2006) Fast and slow dynamics of the cytoskeleton. *Nature materials* 5(8):636-640.

73.   Boal DH (2002) Mechanics of the cell. *Cambridge University Press*.

74.   Bausch AR & Kroy K (2006) A bottom-up approach to cell mechanics. *Nature Physics* 2(4):231-238.

75.   Gardel ML, Shin JH, MacKintosh FC, Mahadevan L, Matsudaira P, & Weitz DA (2004) Elastic Behavior of Cross-Linked and Bundled Actin Networks. *Science* 304(5675):1301-1305.

76.   Borghi N, Sorokina M, Shcherbakova OG, Weis WI, Pruitt BL, Nelson WJ, & Dunn AR (2012) E-cadherin is under constitutive actomyosin-generated tension that is increased at cell–cell contacts upon externally applied stretch. *Proceedings of the National Academy of Sciences* 109(31):12568-12573.

77.   Gonzalez-Rodriguez D, Guevorkian K, Douezan S, & Brochard-Wyart F (2012) Soft matter models of developing tissues and tumors. *Science* 338(6109):910-917.

78.   Maître J-L, Berthoumieux H, Krens SFG, Salbreux G, Jülicher F, Paluch E, & Heisenberg C-P (2012) Adhesion Functions in Cell Sorting by Mechanically Coupling the Cortices of Adhering Cells. *Science* 338(6104):253-256.

79.   Ranft J, Basan M, Elgeti J, Joanny J-F, Prost J, & Jülicher F (2010) Fluidization of tissues by cell division and apoptosis. *Proceedings of the National Academy of Sciences* 107(49):20863-20868.

80.   Farhadifar R, Röper J-C, Aigouy B, Eaton S, & Jülicher F (2007) The Influence of Cell Mechanics, Cell-Cell Interactions, and Proliferation on Epithelial Packing. *Current Biology* 17(24):2095-2104.

81.   Blanchard GB, Kabla AJ, Schultz NL, Butler LC, Sanson B, Gorfinkiel N, Mahadevan L, & Adams RJ (2009) Tissue tectonics: morphogenetic strain rates, cell shape change and intercalation. *Nature Methods* 6(6):458-464.

82.   Marinari E, Mehonic A, Curran S, Gale J, Duke T, & Baum B (2012) Live-cell delamination counterbalances epithelial growth to limit tissue overcrowding. *Nature* 484(7395):542-545.

83.   Brodland GW, Chen DIL, & Veldhuis JH (2006) A cell-based constitutive model for embryonic epithelia and other planar aggregates of biological cells. *International Journal of Plasticity* 22(6):965-995.

84.   Basan M, Risler T, Joanny JF, Sastre-Garau X, & Prost J (2009) Homeostatic competition drives tumor growth and metastasis nucleation. *HFSP Journal* 3(4):265-272.

85.   Montel F, Delarue M, Elgeti J, Malaquin L, Basan M, Risler T, Cabane B, Vignjevic D, Prost J, & Cappello G (2011) Stress clamp experiments on multicellular tumor spheroids. *Physical Review Letters* 107(18):188102.

86.   Cheng G, Tse J, Jain RK, & Munn LL (2009) Micro-Environmental Mechanical Stress Controls Tumor Spheroid Size and Morphology by Suppressing Proliferation and Inducing Apoptosis in Cancer Cells. *PLoS ONE* 4(2):e4632.

87.   Eisenhoffer GT, Loftus PD, Yoshigi M, Otsuna H, Chien CB, Morcos PA, & Rosenblatt J (2012) Crowding induces live cell extrusion to maintain homeostatic cell numbers in epithelia. *Nature*.

88.   Mao Y, Tournier AL, Bates PA, Gale JE, Tapon N, & Thompson BJ (2011) Planar polarization of the atypical myosin Dachs orients cell divisions in Drosophila. *Genes & development* 25(2):131-136.

89.   Wiebe C & Brodland GW (2005) Tensile properties of embryonic epithelia measured using a novel instrument. *Journal of biomechanics* 38(10):2087-2094.

90.   Davidson L & Keller R (2007) Measuring Mechanical Properties of Embryos and Embryonic Tissues. *Methods in Cell Biology*, eds Yu-Li W & Dennis ED (Academic Press), Vol Volume 83, pp 425-439.

91.   Mertz AF, Che Y, Banerjee S, Goldstein JM, Rosowski KA, Revilla SF, Niessen CM, Marchetti MC, Dufresne ER, & Horsley V (2013) Cadherin-based intercellular adhesions organize epithelial cell–matrix traction forces. *Proceedings of the National Academy of Sciences* 110(3):842-847.

92.   Mertz AF, Banerjee S, Che Y, German GK, Xu Y, Hyland C, Marchetti MC, Horsley V, & Dufresne ER (2012) Scaling of Traction Forces with the Size of Cohesive Cell Colonies. *Physical Review Letters* 108(19):198101.

93.   Vedula SRK, Leong MC, Lai TL, Hersen P, Kabla AJ, Lim CT, & Ladoux B (2012) Emerging modes of collective cell migration induced by geometrical constraints. *Proceedings of the National Academy of Sciences* 109(32):12974-12979.

94.   Chu Y-S, Thomas WA, Eder O, Pincet F, Perez E, Thiery JP, & Dufour S (2004) Force measurements in E-cadherin–mediated cell doublets reveal rapid adhesion strengthened by actin cytoskeleton remodeling through Rac and Cdc42. *The Journal of cell biology* 167(6):1183-1194.

95.   Bonnet I, Marcq P, Bosveld F, Fetler L, Bellaïche Y, & Graner F (2012) Mechanical state, material properties and continuous description of an epithelial tissue. *Journal of The Royal Society Interface* 9(75):2614-2623.

96.   Angelini TE, Hannezo E, Trepat X, Marquez M, Fredberg JJ, & Weitz DA (2011) Glass-like dynamics of collective cell migration. *Proceedings of the National Academy of Sciences*.

97.   Poujade M, Grasland-Mongrain E, Hertzog A, Jouanneau J, Chavrier P, Ladoux B, Buguin A, & Silberzan P (2007) Collective migration of an epithelial monolayer in

response to a model wound. *Proceedings of the National Academy of Sciences* 104(41):15988-15993.

98. Sakuma I, Nishimura Y, Chui C, Kobayashi E, Inada H, Chen X, & Hisada T (2003) In vitro measurement of mechanical properties of liver tissue under compression and elongation using a new test piece holding method with surgical glue. *Surgery Simulation and Soft Tissue Modeling*:1003-1003.

99. Suki B, Barabási A-L, Hantos Z, Peták F, & Stanley HE (1994) Avalanches and power-law behaviour in lung inflation. *Nature* 368(6472):615-618.

100. Delalleau A, Josse G, Lagarde J-M, Zahouani H, & Bergheau J-M (2006) Characterization of the mechanical properties of skin by inverse analysis combined with the indentation test. *Journal of biomechanics* 39(9):1603-1610.

101. Vader D, Kabla A, Weitz D, & Mahadevan L (2009) Strain-Induced Alignment in Collagen Gels. *PLoS ONE* 4(6):e5902.

102. Maruthamuthu V, Sabass B, Schwarz US, & Gardel ML (2011) Cell-ECM traction force modulates endogenous tension at cell-cell contacts. *Proceedings of the National Academy of Sciences* 108(12):4708-4713.

103. Tambe DT, Corey Hardin C, Angelini TE, Rajendran K, Park CY, Serra-Picamal X, Zhou EH, Zaman MH, Butler JP, Weitz DA, Fredberg JJ, & Trepat X (2011) Collective cell guidance by cooperative intercellular forces. *Nature Materials* 10(6):469-475.

104. Saez A, Anon E, Ghibaudo M, Du Roure O, Di Meglio J, Hersen P, Silberzan P, Buguin A, & Ladoux B (2010) Traction forces exerted by epithelial cell sheets. *Journal of Physics: Condensed Matter* 22(19):194119.

105. Wendy RT, Frank PTB, Tod AL, Leonidas GA, & Farshid G (2006) Determination of the Poisson's ratio of the cell: recovery properties of chondrocytes after release from complete micropipette aspiration. *Journal of biomechanics* 39(1):78-87.

106. Guck J, Ananthakrishnan R, Mahmood H, Moon TJ, Cunningham CC, & Käs J (2001) The optical stretcher: a novel laser tool to micromanipulate cells. *Biophysical Journal* 81(2):767-784.

107. Yoon Y-Z, Kotar J, Yoon G, & Cicuta P (2008) The nonlinear mechanical response of the red blood cell. *Physical Biology* 5(3):036007.

108. Legant WR, Pathak A, Yang MT, Deshpande VS, McMeeking RM, & Chen CS (2009) Microfabricated tissue gauges to measure and manipulate forces from 3D microtissues. *Proceedings of the National Academy of Sciences* 106(25):10097-10102.

109. Guevorkian K, Gonzalez-Rodriguez D, Carlier C, Dufour S, & Brochard-Wyart F (2011) Mechanosensitive shivering of model tissues under controlled aspiration. *Proceedings of the National Academy of Sciences* 108(33):13387-13392.

110. Stroetz RW, Vlahakis NE, Walters BJ, Schroeder MA, & Hubmayr RD (2001) Validation of a new live cell strain system: characterization of plasma membrane stress failure. *Journal of applied physiology* 90(6):2361-2370.

111. Trzewik J, Artmann-Temiz A, Linder P, Demirci T, Digel I, & Artmann G (2004) Evaluation of lateral mechanical tension in thin-film tissue constructs. *Annals of biomedical engineering* 32(9):1243-1251.

112.   Binnig G, Quate CF, & Gerber C (1986) Atomic force microscope. *Physical Review Letters* 56(9):930-933.

113.   Müller D, Schabert FA, Büldt G, & Engel A (1995) Imaging purple membranes in aqueous solutions at sub-nanometer resolution by atomic force microscopy. *Biophysical Journal* 68(5):1681-1686.

114.   Burnham NA & Colton RJ (1989) Measuring the nanomechanical properties and surface forces of materials using an atomic force microscope. *Journal of Vacuum Science & Technology A: Vacuum, Surfaces, and Films* 7(4):2906-2913.

115.   Johnson KL (1985) Contact Mechanics *(Cambridge University Press, Cambridge)* p 452.

116.   Fischer-Cripps AC (2000) Introduction to Contact Mechanics *(Springer Science and Business Media, LLC, New York) second edition Ed p 151.*

117.   Dimitriadis EK, Horkay F, Maresca J, Kachar B, & Chadwick RS (2002) Determination of Elastic Moduli of Thin Layers of Soft Material Using the Atomic Force Microscope. *Biophysical journal* 82(5):2798-2810.

118.   Jaasma MJ, Jackson WM, & Keaveny TM (2006) Measurement and characterization of whole-cell mechanical behavior. *Annals of biomedical engineering* 34(5):748-758.

119.   Lin DC & Horkay F (2008) Nanomechanics of polymer gels and biological tissues: A critical review of analytical approaches in the Hertzian regime and beyond. *Soft matter* 4(4):669-682.

120.   Lin DC, Shreiber DI, Dimitriadis EK, & Horkay F (2009) Spherical indentation of soft matter beyond the Hertzian regime: numerical and experimental validation of hyperelastic models. *Biomechanics and modeling in mechanobiology* 8(5):345-358.

121.   Lin DC, Dimitriadis EK, & Horkay F (2007) Robust Strategies for Automated AFM Force Curve Analysis I.Non-adhesive Indentation of Soft, Inhomogeneous. *ASME*.

122.   Lin DC, Dimitriadis EK, & Horkay F (2007) Robust strategies for automated AFM force curve Analysis-II: Adhesion-influenced indentation of soft, elastic materials. *ASME* 129(6):904.

123.   Ory DS, Neugeboren BA, & Mulligan RC (1996) A stable human-derived packaging cell line for production of high titer retrovirus/vesicular stomatitis virus G pseudotypes. *Proceedings of the National Academy of Sciences* 93(21):11400-11406.

124.   Rotsch C & Radmacher M (2000) Drug-Induced Changes of Cytoskeletal Structure and Mechanics in Fibroblasts: An Atomic Force Microscopy Study. *Biophysical journal* 78(1):520-535.

125.   Nolen B, Tomasevic N, Russell A, Pierce D, Jia Z, McCormick C, Hartman J, Sakowicz R, & Pollard T (2009) Characterization of two classes of small molecule inhibitors of Arp2/3 complex. *Nature* 460(7258):1031-1034.

126.   Rizvi SA, Neidt EM, Cui J, Feiger Z, Skau CT, Gardel ML, Kozmin SA, & Kovar DR (2009) Identification and characterization of a small molecule inhibitor of formin-mediated actin assembly. *Chemistry & biology* 16(11):1158-1168.

127. Ishizaki T, Uehata M, Tamechika I, Keel J, Nonomura K, Maekawa M, & Narumiya S (2000) Pharmacological properties of Y-27632, a specific inhibitor of rho-associated kinases. *Molecular Pharmacology* 57(5):976-983.

128. Kovács M, Tóth J, Hetényi C, Málnási-Csizmadia A, & Sellers JR (2004) Mechanism of blebbistatin inhibition of myosin II. *Journal of Biological Chemistry* 279(34):35557-35563.

129. Kuznetsova TG, Starodubtseva MN, Yegorenkov NI, Chizhik SA, & Zhdanov RI (2007) Atomic force microscopy probing of cell elasticity. *Micron* 38(8):824-833.

130. Laurent VM, Kasas S, Yersin A, Schäffer TE, Catsicas S, Dietler G, Verkhovsky AB, & Meister J-J (2005) Gradient of Rigidity in the Lamellipodia of Migrating Cells Revealed by Atomic Force Microscopy. *Biophysical journal* 89(1):667-675.

131. Li QS, Lee GYH, Ong CN, & Lim CT (2008) AFM indentation study of breast cancer cells. *Biochemical and Biophysical Research Communications* 374(4):609-613.

132. Docheva D, Padula D, Popov C, Mutschler W, Clausen-Schaumann H, & Schieker M (2008) Researching into the cellular shape, volume and elasticity of mesenchymal stem cells, osteoblasts and osteosarcoma cells by atomic force microscopy. *(Blackwell Publishing Ltd)*, pp 537-552.

133. Matzke R, Jacobson K, & Radmacher M (2001) Direct, high-resolution measurement of furrow stiffening during division of adherent cells. *Nature Cell Biology* 3(6):607-610.

134. Kunda P, Pelling AE, Liu T, & Baum B (2008) Moesin Controls Cortical Rigidity, Cell Rounding, and Spindle Morphogenesis during Mitosis. *Current biology : CB* 18(2):91-101.

135. Puech P-H, Taubenberger A, Ulrich F, Krieg M, Muller DJ, & Heisenberg C-P (2005) Measuring cell adhesion forces of primary gastrulating cells from zebrafish using atomic force microscopy. *Journal of Cell Science* 118(18):4199-4206.

136. Alonso JL & Goldmann WH (2003) Feeling the forces: atomic force microscopy in cell biology. *Life Sciences* 72(23):2553-2560.

137. Robert MH (2000) Micropipette aspiration of living cells. *Journal of biomechanics* 33(1):15-22.

138. Wirtz D (2009) Particle-Tracking Microrheology of Living Cells: Principles and Applications. *Annual Review of Biophysics* 38(1):301-326.

139. Rico F, eacute, lix, Roca-Cusachs P, Gavara N, uacute, ria, Farr, Ramon, Rotger M, & Navajas D (2005) Probing mechanical properties of living cells by atomic force microscopy with blunted pyramidal cantilever tips. *Physical Review E* 72(2):021914.

140. Berdyyeva TK & et al. (2005) Human epithelial cells increase their rigidity with ageing in vitro : direct measurements. *Physics in Medicine and Biology* 50(1):81.

141. Choi A & Zheng Y (2005) Estimation of Young's modulus and Poisson's ratio of soft tissue from indentation using two different-sized indentors: Finite element analysis of the finite deformation effect. *Medical and Biological Engineering and Computing* 43(2):258-264.

142. Maniotis AJ, Chen CS, & Ingber DE (1997) Demonstration of mechanical connections between integrins, cytoskeletal filaments, and nucleoplasm that

stabilize nuclear structure. *Proceedings of the National Academy of Sciences* 94(3):849-854.

143.   Hutter JL & Bechhoefer J (1993) Calibration of atomic force microscope tips. *Review of Scientific Instruments* 64(7):1868-1873.

144.   A-Hassan E, Heinz WF, Antonik MD, D'Costa NP, Nageswaran S, Schoenenberger C-A, & Hoh JH (1998) Relative Microelastic Mapping of Living Cells by Atomic Force Microscopy. *Biophysical journal* 74(3):1564-1578.

145.   Charras GT, Lehenkari PP, & Horton MA (2001) Atomic force microscopy can be used to mechanically stimulate osteoblasts and evaluate cellular strain distributions. *Ultramicroscopy* 86(1-2):85-95.

146.   Lin DC, Dimitriadis EK, & Horkay F (2007) Robust Strategies for Automated AFM Force Curve Analysis---I. Non-adhesive Indentation of Soft, Inhomogeneous Materials. *Journal of Biomechanical Engineering* 129(3):430-440.

147.   Colombelli J & Solon J (2012) Force communication in multicellular tissues addressed by laser nanosurgery. *Cell and Tissue Research*:1-15.

148.   Kim JH & Gouldstone A (2008) Spherical indentation of a membrane on an elastic half-space. *Journal of Materials Research* 23(8):2212-2220.

149.   Zamir EA & Taber LA (2004) On the effects of residual stress in microindentation tests of soft tissue structures. *Journal of Biomechanical Engineering* 126(2):276.

150.   Zhang C & Zhang Y (2009) Extracting elastic properties and prestress of a cell using atomic force microscopy. *Journal of Materials Research* 24(03):1167-1171.

151.   Kumar S, Maxwell IZ, Heisterkamp A, Polte TR, Lele TP, Salanga M, Mazur E, & Ingber DE (2006) Viscoelastic retraction of single living stress fibers and its impact on cell shape, cytoskeletal organization, and extracellular matrix mechanics. *Biophysical Journal* 90(10):3762.

152.   Mattey D, Burdge G, & Garrod D (1990) Development of desmosomal adhesion between MDCK cells following calcium switching. *Journal of cell science* 97(4):689-704.

153.   Pollard TD & Borisy GG (2003) Cellular motility driven by assembly and disassembly of actin filaments. *Cell* 112(4):453-465.

154.   Kovacs EM, Verma S, Ali RG, Ratheesh A, Hamilton NA, & Akhmanova A (2011) N-WASP regulates the epithelial junctional actin cytoskeleton through a non-canonical post-nucleation pathway. *Nature cell biology* 13(8):934-943.

155.   Verma S, Han SP, Michael M, Gomez GA, Yang Z, Teasdale RD, Ratheesh A, Kovacs EM, & Ali RG (2012) A WAVE2–Arp2/3 actin nucleator apparatus supports junctional tension at the epithelial zonula adherens. *Molecular biology of the cell* 23(23):4601-4610.

156.   Rauzi M, Lenne PF, & Lecuit T (2010) Planar polarized actomyosin contractile flows control epithelial junction remodelling. *Nature* 468(7327):1110-1114.

157.   Smutny M, Cox HL, Leerberg JM, Kovacs EM, Conti MA, Ferguson C, Hamilton NA, Parton RG, & Adelstein RS (2010) Myosin II isoforms identify distinct functional modules that support integrity of the epithelial zonula adherens. *Nature cell biology* 12(7):696-702.

158.   Michelot A & Drubin DG (2011) Building distinct actin filament networks in a common cytoplasm. *Current Biology* 21(14):R560-569.

159.   Chen HH & Brodland GW (2000) Cell-Level Finite Element Studies of Viscous Cells in Planar Aggregates. *Journal of Biomechanical Engineering* 122(4):394-401.

160.   Gere JM (2004) Mechanics of Materials.

161.   Brown XQ, Ookawa K, & Wong JY (2005) Evaluation of polydimethylsiloxane scaffolds with physiologically-relevant elastic moduli: interplay of substrate mechanics and surface chemistry effects on vascular smooth muscle cell response. *Biomaterials* 26(16):3123-3129.

162.   Fuard D, Tzvetkova-Chevolleau T, Decossas S, Tracqui P, & Schiavone P (2008) Optimization of poly-di-methyl-siloxane (PDMS) substrates for studying cellular adhesion and motility. *Microelectronic Engineering* 85(5–6):1289-1293.

163.   Edelstein A, Amodaj N, Hoover K, Vale R, & Stuurman N (2010) *Computer Control of Microscopes Using µManager* (John Wiley & Sons, Inc.).

164.   Pratt WK (1991) Digital Image Processing. *Wiley, New York* 2nd ed.

165.   Steger C (1998) An Unbiased Detector of Curvilinear Structures. *IEEE Trans. Pattern Anal. Mach. Intell.* 20(2):113-125.

166.   Christensen RM (1971) Theory of viscoelasticity: An Introduction.

167.   Perlman CE & Bhattacharya J (2007) Alveolar expansion imaged by optical sectioning microscopy. *Journal of applied physiology* 103(3):1037-1044.

168.   Sacks MS, He Z, Baijens L, Wanant S, Shah P, Sugimoto H, & Yoganathan AP (2002) Surface Strains in the Anterior Leaflet of the Functioning Mitral Valve. *Annals of biomedical engineering* 30(10):1281-1290.

169.   Wolpert L (2001) Principles of Development *(Oxford University Press, USA) 2 Ed.*

170.   Fernandez-Gonzalez R, Simoes SdM, Röper J-C, Eaton S, & Zallen JA (2009) Myosin II Dynamics Are Regulated by Tension in Intercalating Cells. *Developmental cell* 17(5):736-743.

171.   Ren Y, Effler JC, Norstrom M, Luo T, Firtel RA, Iglesias PA, Rock RS, & Robinson DN (2009) Mechanosensing through Cooperative Interactions between Myosin II and the Actin Crosslinker Cortexillin I. *Current Biology* 19(17):1421-1428.

172.   Angelini TE, Hannezo E, Trepat X, Fredberg JJ, & Weitz DA (2010) Cell Migration Driven by Cooperative Substrate Deformation Patterns. *Physical Review Letters* 104(16):168104.

173.   Butler LC, Blanchard GB, Kabla AJ, Lawrence NJ, Welchman DP, Mahadevan L, Adams RJ, & Sanson B (2009) Cell shape changes indicate a role for extrinsic tensile forces in Drosophila germ-band extension. *Nature cell biology* 11(7):859-864.